Site BA3[1]

Kelemen, P.B., Matter, J.M., Teagle, D.A.H., Coggon, J.A., and the Oman Drilling Project Science Team[2]

Keywords: Oman Drilling Project, OmanDP, Site BA3, Hole BA3A, Wadi Lawayni, Samail ophiolite, mantle peridotite, hydrogeology, multiborehole testing, chemosynthetic biosphere

Chapter contents

Introduction 1
Operations 2
Background description 2
Veins 5
Structural geology 9
Geochemistry 14
Microbiology 16
Paleomagnetism 16
Physical Properties 17
Imaging spectroscopy 20
Downhole logging and hydrogeological testing 21
References 21
Figures 23
Tables 90
Supplemental tables 90

Introduction

Site BA3

Site BA3 (22.86617°N, 58.71057°E) is situated in the southern end of Wadi Lawayni and hosted in partially serpentinized peridotite of the mantle section of the Samail Ophiolite (see Figure F1 in the **Introduction to Science Theme 1A** chapter). Site BA3 is adjacent to an existing borehole (Hole NSHQ-14 at 22.86611°N, 58.71056°E) drilled by the Ministry of Regional Municipalities and Water Resources (see Figure F2 in the **Introduction to Science Theme 3** chapter). Hole NSHQ-14 is not included in the Ministry's current groundwater monitoring network, but it has been subject to water, dissolved gas, and microbial sampling by members of the Oman Drilling Project Science Party from 2012 to 2020. Groundwater in Hole NSHQ-14 is hyperalkaline, with a pH of 11.5 and dissolved hydrogen and methane concentrations as high as 2.9 mM and 0.17 mM, respectively (Miller et al., 2016; Rempfert et al., 2017). The groundwater is more than 68 years old, as indicated by pre-hydrogen-bomb (1952) tritium concentrations, and exhibits significant non-atmospheric helium accumulation (Paukert et al., 2019). Based on the presence of hyperalkaline groundwater and the relatively high dissolved hydrogen concentration in Hole NSHQ-14, we decided to drill a 300 m diamond-cored hole next to it. The hole sited here is a far-field site of the Wadi Lawayni multiborehole test site. The resulting data will address active alteration of exposed mantle peridotite (hydration, oxidation, and carbonation) and will be used to explore the subsurface hydrology and chemosynthetic biosphere fostered by weathering of mantle peridotite.

Geological setting

Site BA3 is situated on a raised gravel terrace above an active wadi channel (Fig. F1). The surface layer of alluvium is ~20 m thick. The geology of this site is predominantly partially serpentinized harzburgite with minor dunite bodies and pyroxenite and gabbronorite dikes.

No drill pad preparation was necessary at this site because of its wide, level morphology. Existing access via a track from the paved road to the south was adequate and required minimal improvement to facilitate access for the diamond coring drill rig and associated vehicles.

[1] Kelemen, P.B., Matter, J.M., Teagle, D.A.H., Coggon, J.A., and the Oman Drilling Project Science Team, 2020. Site BA3. *In* Kelemen, P.B., Matter, J.M., Teagle, D.A.H., Coggon, J.A., and the Oman Drilling Project Science Team, *Proceedings of the Oman Drilling Project*: College Station, TX (International Ocean Discovery Program). https://doi.org/10.14379/OmanDP.proc.117.2020

[2] OmanDP Science Team affiliations.

MS OmanDP-117
Published 16 December 2020

Operations

An overview of all holes drilled is given in Table T3 in the **Methods** chapter. Drilling operations and core curation information are reported in Table T1.

All times are reported as local time in Oman (UTC + 4 h).

Hole BA3A drilling summary

- Spud-in: 08 Jan 2018, 13:30 h
- First core on deck: 08 Jan 2018, 14:00 h
- Surface casing (HW) installed: 08 Jan 2018, 5.7 m below ground level (mbgl)
- HW extended: 09 Jan 2018, 8.7 mbgl
- HW extended: 11 Jan 2018, 13.20 mbgl
- HW extended: 13 Jan 2018, 20.70 mbgl
- NW casing installed: 15 Jan 2018, 23.80 mbgl
- Final core on deck: 22 Jan 2018, 10:30 h
- Total depth (TD) of borehole: 302.70 mbgl

Geology summary

Serpentinized harzburgite with thin gabbroic dikes and dunite layers.

Technical issues

At 45.0 mbgl (11 Feb 2018), there was indication of bit blocking and no drilling fluid circulation. Drillers pulled out of hole (POOH) HQ drill pipes and cleaned the drill bit, followed by a run in hole (RIH) and fixing of broken wireline. POOH HQ drill pipes on 13 Feb 2018 because of problems pulling out the inner tube to recover core. The problem was resolved after POOH.

Operations summary

- 6–7 Jan 2018: mobilize rig, drilling equipment, and accessories to Hole BA3A from the CM site.
- 8 Jan 2018: start drilling Hole BA3A after setup of HQ drill bit assembly from ground level to 8.70 mbgl. Extend HW surface casing to 5.7 mbgl.
- 9 Jan 2018: drill to 29.70 mbgl; extend HW surface casing to 8.7 mbgl; drill to 41.70 mbgl.
- 10–11 Jan 2018: drill to 45.0 mbgl; loss of circulation and bit blockage; check inner tube and RIH, but problems persist. POOH, replace bit, and extend HW surface casing to 13.20 mbgl.
- 13 Jan 2018: additional extension of HW surface casing to 20.70 mbgl due to falling shoe bit and casing; POOH and RIH after checking inner tube again. Resume drilling at 15:20 h.
- 14 Jan 2018: stop coring at 14:00 h to change drill rig oil filters.
- 15 Jan 2018: ream and extend HW surface casing 20.70–23.70 mbgl; core to 152.70 mbgl.
- 16–21 Jan 2018: core 152.70–290.70 mbgl.
- 22 Jan 2018: core to TD = 302.70 mbgl. Complete POOH and demobilization of rig and drilling equipment.

Background description

Hole BA3A provides access to more than 300 m of material from the shallow mantle lithosphere. The main lithology logged in Hole BA3A is harzburgite. Minor abundances of dunite and crosscutting gabbroic to clinopyroxenitic dikes complete the primary composition of the core. The abundance of the principal lithologies and their variations with depth including mineral modes are documented in Figures F2 and F3 and Table T2. Harzburgite dominates the core with subordinate dunite in the uppermost 180 m. Gabbro, olivine gabbro, and clinopyroxenite dikes make up <1% of the core, whereas dunite contributes 2% by thickness.

Alteration is pervasive and extensive, concentrated along dikes and veins in the form of halos. Serpentine is the main alteration mineral in the ultramafic rocks. A variety of calcium-bearing phases including prehnite, tremolite, hydrogrossular, xonotlite, and Ca carbonates formed in the vicinity of dikes. Fractured zones are frequent throughout the core and are associated with particularly intense alteration and high vein density. Complete description and frequency of veins and the structures associated with deformation zones are found **Veins** and **Structural geology**, respectively.

Lithologic units and subunits were defined in the context of changes in lithology, mineral assemblage, modal abundance, structural and textural variations, alteration, veining, and fracturing. A complete description of individual units and subunits is available in supplemental Tables ST1 and ST2. Supplemental Table ST1 contains all data recorded from the background description team during visual inspection of the cores, and supplemental Table ST2 summarizes all information related to the individual lithologic units extracted from the master table mentioned above. The results presented below are supported by X-ray diffraction (XRD) and chemistry (see **Geochemistry**) analyses.

Lithologic sequence

A single major sequence was described in Hole BA3A, consisting of mainly of harzburgite with modal transitions into dunite and minor intercalations of gabbroic and clinopyroxenitic dikes. A minor sequence, the alluvium sequence, forms the uppermost 6 m of the core. A brief description of interesting features in this minor sequence is given in the following para-

graph. The rest of this section focuses on the major harzburgitic sequence. The depths and properties of the sequences are summarized in Table T3.

Alluvium sequence

The alluvium sequence, 0–6.32 m, was retrieved in Sections BA3A-1Z-1 through 3Z-1. The sequence is composed of a mix of mafic to ultramafic blocks of various sizes (from centimeter to several meters) with, in some places, matrix-supported carbonated breccia (Fig. F4). Millimeter-size clasts likely have the same composition as the surrounding pebbles and boulders, but no precise mineralogy has been established for them. The sequence includes a harzburgite almost 3 m long. The occurrence of gravel and carbonated breccia below it indicates this is a large boulder within the alluvium sequence rather than part of the main harzburgite sequence.

Harzburgite sequence

The harzburgite sequence, 6.32–302.79 m (end of hole), was retrieved from Sections 3Z-1 through 114Z-4. The 300 m thick harzburgite sequence includes harzburgite (97.6%, 289.2 m) with dunite patches (2.0%, 6.0 m) that are orthopyroxene bearing in places. The lowermost dunite patch is at 186 m depth. Characteristic mantle foliation textures and pyroxene-enriched layers are typical of this sequence. The remaining 0.5% consists of gabbro, olivine gabbro, and clinopyroxenite, mostly occurring as thin (millimeter to a few centimeters thick) and strongly altered dikes.

Mineral variations with depth in the peridotite are given in Figure F5. The harzburgite is relatively homogeneous with modal abundances of orthopyroxene ranging 20%–40% (mean ~ 30%) and locally lower abundances where dunite patches are described. A few percent spinel and clinopyroxene are common in the harzburgite. A high mode of clinopyroxene was described at ~115–119 m, coinciding with lower orthopyroxene content. This could mark a lherzolitic portion of the core or be a mistake related to a locally higher degree of alteration. Unfortunately, no thin section or XRD data are available at this particular depth to confirm the visual description.

Description of principal rock types

Descriptions of the principal rock types are derived from macroscopic and microscopic observations and are presented in order of abundance below and in Table T2.

Harzburgite

Harzburgite is the most abundant rock type of the harzburgite sequence and of the total Hole BA3A core. The harzburgites are medium to coarse grained and equigranular (e.g., Fig. F6). The primary modal abundance of olivine ranges 65%–85% (average grain size = 1.5–3.5 mm; maximum = 4.5 mm). Orthopyroxene mode ranges 15%–20% (average grain size = 2.3–4 mm; maximum = 6.7 mm). Textures are typically porphyroclastic to granular. The harzburgites are frequently foliated with a foliation plane defined by shape-preferred orientation (SPO) of the orthopyroxenes observed both macroscopically (Fig. F6A) and microscopically (Fig. F7) starting from 140 m. Pyroxene-enriched layers are also common along the section (Fig. F6B, F6C). Banding is generally weak (Fig. F6B), but more marked banding also occurs (e.g. Fig. F6C). There is no discernible variation in the frequency or intensity of banding and foliation as a function of depth.

The abundance of clinopyroxene increases with depth; samples at 140–300 m contain clinopyroxene-enriched harzburgite zones with modal abundances ranging 3%–5% (Fig. F8). Further, orthopyroxene-clinopyroxene intergrowths (Fig. F9) and clinopyroxene lamellae in orthopyroxene (Fig. F8) are common from 100 m downhole. In some cases, clinopyroxene can contribute as much as 40% of orthopyroxene crystals by volume. Otherwise, clinopyroxene grains are mostly found in interstitial locations on orthopyroxene grain boundaries (Fig. F8), with the exception of rare prismatic crystals in the clinopyroxene-enriched zones (Fig. F8C), where grain sizes can reach 4 mm. Clinopyroxene grain size ranges 0.4–1.6 mm, and the mode ranges 0%–5%.

Spinel is anhedral to subhedral with modes of 0.5%–5%. Grains range in size from a few hundred micrometers to 2.8 mm and can locally exhibit interstitial or vermicular habit when spinel is proximal to prismatic clinopyroxene and orthopyroxene (Fig. F7). The most common spinel phases in the uppermost samples are magnetite and ferrichromite, presumed to be alteration after igneous chromite; Cr-poor magnetite is observed in serpentine veins (Fig. F10A–F10C). Chromite is the dominant spinel phase in the rest of Hole BA3A (Fig. F10D–F10F).

Sulfides are sparse in the uppermost samples but increase in abundance through the uppermost 100 m of core. Modes reach 2% in samples in the lowermost 100 m of the core. Chalcopyrite, cuprite, bornite, and native copper were observed at maximum grain sizes from 0.2 mm (Fig. F11). Cuprite and bornite occur as alteration phases after chalcopyrite, and native copper is intergrown with the chalcopyrite.

Extensive alteration and serpentinization in Hole BA3A are ubiquitous and increase further where the rock is fractured (Fig. F12A). Olivine and orthopyroxene are extensively replaced by serpentine (e.g., Figs. F9C, F11D, F13C; Table T4), and brucite is documented at 120 and 250 m (Samples 52Z-1, 33–38 cm, and 96Z-2, 0–5 cm; Table T4). Clinopyroxene is

the most resistant to alteration. Bulk rock XRD reveals preserved olivine and orthopyroxene relics from 20 m (e.g., Sample 12Z-4, 45–50 cm; Table T4); these relics are observed in thin section (e.g., Fig. F7) and become more common toward the bottom of the hole.

Oxidation, inferred from brown or orange coloration of the rock, was commonly noted as an alteration feature in harzburgite (Fig. F14). Pervasively oxidized rocks (e.g., Fig. F12B) occur preferentially in the upper parts of the core, whereas oxidation below 250 m is localized to fractures and faults or around dikes and cracks (e.g., Fig. F12C). Intense oxidation at the top of the hole, most likely linked to surface weathering, is almost completely gone within the uppermost 10 m. In zones of intense oxidation, the primary mineralogy is, in most cases, completely destroyed by alteration, and no fresh olivine or orthopyroxene cores remain (Fig. F13; 80 m).

Dunite

Dunite is the second most abundant lithology recovered from Hole BA3A. It appears only in the upper and middle part of the core and makes up a very minor part of this sequence (6 m, 2.02%) (Fig. F2; Table T2). Dunite occurs in patches (Fig. F15A) and between orthopyroxene-rich layers (Fig. F15B) in the harzburgite sequence.

Three dunite thin sections were produced: two from ~20 m (uppermost dunite bodies, e.g., interval 13Z-2, 22–25 cm) and one from ~190 m (lowermost dunite bodies, interval 75Z-1, 42–44 cm). In all thin sections, olivine, inferred to be initially subhedral and equigranular from the distribution of mesh-textured serpentine, is extensively replaced by serpentine, which forms a dense network that to a large extent appears to pseudomorph the original grains (Fig. F16A, F16B). The primary modal abundance of olivine is inferred to have ranged 91%–95% with slightly lower abundance in the lower sections. Orthopyroxene in the dunites is extensively altered. Its mode, grain shape, and grain size were inferred from relics and pseudomorphic serpentine. Orthopyroxene mode is up to 2%, grains are anhedral to subhedral, and size ranges 1.2–1.6 mm. Subhedral clinopyroxene, with modes <3% and average grain size of 0.6–0.8 mm, was only observed in the deeper dunitic lenses, consistent with the trend in the harzburgites.

Spinels in the dunite are most often subhedral and polygonal; modes range 3%–5% and average grain sizes range 0.2–1.2 mm. Magnetite replacing chromite is the dominant spinel phase in the two shallow dunitic samples (Fig. F16A, F16C, F16D), whereas chromite is modally dominant in the deeper sample. Accessory sulfides are observed but only in the shallower samples and are in general tiny (<0.4 mm).

All investigated dunites are highly altered and display a typical mesh texture with no olivine cores preserved. This observation is confirmed by XRD analysis (e.g. Fig. F17C, Sample 75Z-1, 39–44 cm; Table T4). In addition to the classical mesh cell type (Fig. F16B), two atypical types were observed. Samples 13Z-2, 29–32 cm (20 m), and 75Z-1, 42–44 cm (190 m), exhibit "fingerprint" texture consisting of concentric rings inside completely serpentinized olivine (Fig. F17). Both of these samples were taken proximal to serpentine veins. The second mesh cell type consists of apparently eroded mesh cell cores with secondary euhedral 0.03 mm lizardite crystals growing from the rim into the open space (Fig. F16A, F16C, F16E, Sample 13Z-2, 22–25 cm; 20 m).

Dikes

Dikes crosscut the harzburgitic sequence. The apparent thickness, uncorrected for dip, is typically ~1 cm; the largest dikes are as thick as 14 cm. The abundance of dikes increases slightly in the lower part of the sequence where dunites are absent (Fig. F18A). Dikes are either gabbroic (Fig. F19A) or clinopyroxenitic (Fig. F19B, F19C). Overall, dike composition does not vary along the sequence (Fig. F18B). However, it should be noted that the primary mineralogy and mode were not always easy to determine because of the high degree of alteration (Fig. F20A).

Gabbroic dikes

Gabbroic dikes are the most common dike type: total thickness = 89 cm, comprising 64 cm of gabbro and 25 cm of olivine gabbro through the recovered core. Gabbroic dikes are represented by 7 thin sections throughout Hole BA3A. Most of the gabbros are 100% altered, and alteration colors include white, gray, and green. Under these circumstances, evaluation of the primary igneous features was not possible. However, in some cases pseudomorphic replacement in the gabbros and olivine gabbros records a granular protolith with grain size ranging from fine to coarse and a consistently equigranular grain size distribution (Fig. F21A, F21B, F21D, F21E).

Based on the assumption of pseudomorphic replacement where igneous-like textures are preserved, preservation of rare clinopyroxene grains, grain sizes, abundances, and shapes were inferred. Clinopyroxene, the most commonly preserved, forms subhedral crystals with subequant or prismatic habit, average size ranging 0.2–2.5 mm, and modal abundance of 30%–90%. Maximum grain size is 6 mm. Subhedral olivine pseudomorphs, identified from a dark brown color in hand specimen, contribute 5%–55% of the mode of the gabbros and are inferred to have had subequant shape with an average grain size of 2 mm (maximum = 4.5 mm). Pseudomorphs inferred to be after plagioclase are anhedral to subhedral with in-

tergranular texture or tabular shape and modal abundance of 20%–90%. Spinel is anhedral, interstitial, and comprises 0.5%–2% of the gabbros. Grain size ranges from a few hundred micrometers to 1.6 mm. Pyrrhotite was noted in Section 30Z-1 in both XRD and thin section (Fig. F21A–F21C, F21F).

The primary mineralogy is extensively replaced by secondary phases that include tremolite, hydrogrossular, chlorite, serpentine, clay, talc, prehnite, and magnetite (Fig. F22; Table T4). These phases are characteristic of rodingitic assemblages and are commonly pink or pale brown (Fig. F20B). The composition of the replacing phases is commonly linked to that of their precursor. For example, in a microgabbro at 65 m, tremolite replaces clinopyroxene, serpentine replaces olivine, and hydrogrossular replaces plagioclase (Fig. F21A, F21B, F21D, F21E).

Metasomatic changes to bulk rock composition on at least the millimeter scale are indicated by mineral assemblages. Detailed observation of a contact between a gabbroic dike and serpentinized harzburgite at 150 m reveals that chlorite, serpentine, and hydrogrossular are concentrated at the contact zone between dike and host rock (thin section Sample 64Z-5, 22–26 cm; Fig. F22). In this case the dike itself is almost completely replaced by chlorite, hydrogrossular, and magnetite; prismatic clinopyroxene is the only survivor from the protolith (Fig. F22A–F22E). In another dike/harzburgite contact at 250 m (Sample 95Z-2, 50–53 cm), prehnite, talc, and chlorite are present in an alteration zone on the contact (Fig. F23). Orthopyroxene relics are also preferentially preserved in harzburgite within a few millimeters of the gabbro contact (Fig. F23E, F23F).

Clinopyroxenite dikes

Clinopyroxenite is the second most important dike type in the sequence with a total thickness of 39 cm through the whole core. Clinopyroxenite dikes and orthopyroxene bands have very similar appearance in fresh rock, but the nature of the contact between these lithologies and the harzburgite is consistently different, allowing distinction between dikes and bands. Dikes were inferred when a sharp contact between the dike and the host rock was observed, whereas gradational transitions were used as primary criteria to identify banding. XRD analysis supports these criteria (e.g., Fig. F19C; Sample 99Z-2, 71 cm; Table T4).

Typically, clinopyroxenites are granular, coarse to medium grained, equigranular, subequant to prismatic, and have average grain sizes of 0.3–0.8 mm. Modal abundance ranges 75%–90%. Olivine, based on observations of pseudomorphic lizardite, was subhedral, subequant, and present with modes to 25%.

Clinopyroxenites, like the other rock units in Hole BA3A, are extensively altered, although clinopyroxene is the phase that was most resistant to alteration. One sample from 120 m comprises a millimeter-thick clinopyroxenitic dike with two 0.2 mm clinopyroxenite dikes in harzburgite; clinopyroxene is altered and pseudomorphed by tremolite, which appears red in hand specimen (Sample 52Z-1, 66–71 cm, Fig. F20C). This identification is supported by XRD (Fig. F24A).

As with the gabbro dikes, metasomatic changes are observed at the dike/harzburgite contact. Serpentine takes a characteristic shape, orthopyroxene is preferentially preserved (Fig. F24B, F24C, F24E, F24F), and chalcopyrite is locally altered to cuprite, bornite, and native copper (Fig. F24D).

Lithologic summary

Core from Hole BA3A provides an almost 300 m long homogeneous section of harzburgite below a few meters of alluvium. Within the harzburgite section, dunite, comprising 2% of the core by volume, is present only in the upper 190 m. Gabbroic and clinopyroxenite dikes comprise 0.4% of the core and show no systematic changes with depth. The mineral assemblage of the harzburgite is mostly monotonous with the exception of clinopyroxenite-rich zones in the lower part of the core. The abundance of sulfides and the chromite/magnetite ratio also increase in the lower parts of the core.

Every rock examined has undergone pervasive and almost complete alteration. Harzburgite is altered to serpentine, with brucite in places. Gabbroic dikes are commonly pseudomorphically replaced by Ca-bearing phases such as prehnite, hydrogrossular, and tremolite and by Ca-free phases such as lizardite and chlorite. Evidence of metasomatic changes within a few millimeters of dike contacts is provided by high-variance zoned assemblages of Ca-bearing phases at dike margins and by preferential preservation of orthopyroxene in harzburgites in the vicinity of dike margins. Oxidation is common throughout the core, with the uppermost parts pervasively oxidized and localization of oxidation to fractures in the lower parts.

The lithostratigraphy of Hole BA3A is shown in Figure F25.

Veins

In the following sections, we describe the vein assemblages in the cores sampled from Hole BA3A and their variation as a function of depth below the surface. Unlike Hole BA1B core, in which dunite dominates the host rock in the upper 160 m, the host rock for veins in Hole BA3A is mainly harzburgite from

top to bottom. Hole BA3A is also further "downstream" in Wadi Laywani and east of the main drainage, so it probably has a different erosional history. Whereas Hole BA1B was spudded into <1 m of gravel overlying a bedrock outcrop visible on the surface 3–4 m away, drilling in Hole BA3A began in ~3 m of gravel and conglomerate in an area where no bedrock was visible on the surface for more than 100 m in any direction.

General characteristics of the vein types were recorded for the depth intervals in which they occurred within the core. Continuous downhole observations for Hole BA3A are given in the vein log in supplemental Table ST3. Excel spreadsheets used for calculations and downhole plots are given in supplemental Table ST4 (see supplemental Table ST5 for calculations for plots). Abbreviations used in the text and figures are defined in Table T5 in the **Methods** chapter.

Overviews of the overall downhole variation in vein mineralogy and area percent of veins, together with a summary of crosscutting relationships between different vein types, are shown in Figures F26, F27, F28, and F29.

The vein group defined an open-ended list of vein types, which is discussed more extensively in Veins in the **Site BA1** chapter. We used these without modification in describing the veins encountered in Hole BA3A core. As discussed previously, we departed somewhat from the common practice of defining a series of vein generations. We expected that there could be mutually crosscutting relationships between vein types rather than a specific sequence from V1, V2 … V*n*, and indeed this is borne out by the quantitative crosscutting statistics shown in Figure F26. For example, though waxy green serpentine veins generally crosscut all other vein types, Figure F26 shows that in ~10% of crosscutting relationships they are cut by white (vein type Sf, 9 observations), dark (Sa + Sc + Sd, 4 observations), and composite (Se, 2 observations) serpentine veins.

Before we discuss vein frequency and proportion in the core, some caveats are necessary. Estimates of vein frequency in the peridotites are complicated by pervasive development of a microscopic serpentine mesh texture where mesh veins surround polygonal to rounded mesh cores with typical vein spacing as small as tens of micrometers. The smallest throughgoing veins arise via coarsening of linear zones of mesh veins. To varying degrees and depending on the color of microscopic mesh veins and the host rock matrix, some of the veins emerging from the mesh vein network are more or less visible. These were not logged consistently in describing the core recovered from Hole BA1B. Toward the top of Hole BA1B, these were sometimes visible as brown veins or white veins with brown halos in the orange, oxidized dunites (logged as vein types Sc and sometimes Sf). Deeper in Hole BA1B, the larger veins emerging from the mesh network were black (logged as vein type Sa).

As a result of the inconsistent recording for description of veins arising from the serpentine mesh in Hole BA1B, we did not log veins emerging from the mesh network at all in the Hole BA3A core. Thus, the darker colored veins that were logged (Sa, Sd) in Hole BA3A are larger, tabular features and distinct vein sets and networks superimposed on the mesh network. It remains the case, as in the core from Hole BA1B, that these darker vein sets tend to be older than the calcite-bearing, waxy green serpentine and white serpentine veins.

As in Hole BA1B, veins are most numerous and comprise the largest proportion of the core in the upper half of Hole BA3A (Figs. F27, F28). (Note: We struggled to estimate the area or overall intensity of veins in core from Hole BA1B using observations of vein density and vein width. Considerable empiricism was required. As a result, we added a column to the visual core description [VCD] spreadsheet for Holes BA3A and BA4A for estimates of the percent area occupied by a vein, vein set, or vein network over specific depth intervals in the core. As a result, [a] the quantitative estimates of cumulative vein area are far more reliable for Holes BA3A and BA4A than for Hole BA1B, and [b] unfortunately, caution is required when comparing the vein area estimates for Hole BA1B with those for Holes BA3A and BA4A.) The estimated area of the Hole BA3A veins per meter downhole is about one order of magnitude lower than that below 200 m depth in both Holes BA1B and BA3A. The fact that this is true for both suggests, again, that the transition from dunite above to harzburgite below in Hole BA1B was not the main control on the decrease in vein area downhole, since this decrease is also observed in Hole BA3A where harzburgites dominate the lithology throughout the core.

Veins comprise a larger proportion of the core in Hole BA1B compared to Hole BA3A (Fig. F27). Whereas these estimates are based on different types of data in the two holes, the quantitative estimates conform to our qualitative impression during visual core description that veins are less abundant in Hole BA3A. The reasons for this may include a different erosional history, where regolith is more regularly eroded and removed from Hole BA3A compared to Hole BA1B.

As in Hole BA1B, based on crosscutting relationships, many of the youngest veins in Hole BA3A are calcite bearing (composite with serpentine and others that are ~100% calcite). Calcite-bearing veins decrease in frequency and proportion downhole and are very rare below ~100 m. There is a high proportion of waxy green veins in the upper 200 m of the hole (Figs. F28, F29). "White serpentine" veins re-

main relatively abundant throughout Hole BA3A, with distinct peaks in frequency associated with fault zones. They are joined by white xonotlite-bearing veins in gabbro dikes that cross contacts into peridotite. Where they can be distinguished, waxy green veins generally cut white serpentine veins and are perhaps coeval with the xonotlite-bearing veins.

Observations

Macroscopic identification of vein types

In this section, we provide exemplary illustrations from Hole BA3A of vein types used in the VCD logs. Readers are referred to **Macroscopic identification of vein types** in the **Site BA1** chapter for a more complete description of the vein types.

Carbonate-bearing veins

Ca veins. Ca veins are layered composite veins composed of green to black serpentine and carbonate minerals. They are pervasive in the uppermost cores. Ca veins are divided into three groups by their appearance:

- Ca1 veins have dark-colored serpentine cores with carbonate rims (Fig. F30A).
- Ca2 veins have carbonate cores with serpentine rims (this vein type was not observed in Hole BA3A).
- A few Ca3 veins include waxy green serpentine and carbonate minerals (Fig. F30B).

For the most part, in describing the core from Hole BA3A we did not record subtypes based on whether the cores or the rims were calcite bearing, unlike in the description of the upper 200 m of the core from Hole BA1B.

Cb veins. Cb veins are white monomineralic, granular veins of carbonate minerals (Fig. F30C). They occur in the uppermost cores together with Ca veins. The abundance of both Ca and Cb veins decreases systematically with depth, and they were not observed in the core below 100 m.

Serpentine veins. Serpentine vein types were classified based on color and texture. "Ideal" examples of each vein type were clearly distinct in the core and dominated the veins we described, though of course ambiguous instances also occur.

Sa veins. Sa veins are black network or branched veins of serpentine with cryptocrystalline magnetite (Fig. F30D). Sa veins occur throughout the core, irrespective of depth. In most cases, Sa veins are cut by other types of veins.

Sb veins. Sb veins are waxy green to waxy white serpentine veins (Fig. F30E), described in more detail in **Veins: Hole BA1B** in the **Site BA1** chapter.

Sc veins. Sc veins are thin (typically <0.5 mm) brown to brownish white serpentine veins (Fig. F30F).

Sd veins. Sd veins are dark green serpentine veins (Fig. F30G). Serpentine veins in shear zones are usually classified as type Sd veins.

Se veins. Se veins are composite serpentine veins composed of more than one distinctly different color of serpentine (Fig. F30H).

Sf veins. Sf veins are thin (typically < 0.5 mm) white serpentine veins (Fig. F30I).

Sg veins. Sg veins are bluish green (horrible green) (Fig. F30J), generally >5 mm, and restricted to the lowermost cores, where they replace and surround highly deformed blocks of magmatic rocks.

Xonotlite-bearing veins. X veins contain xonotlite, a translucent white mineral (Fig. F30K).

Observations of veins in thin sections

The major lithology in Hole BA3A is serpentinized harzburgite. Upon serpentinization, orthopyroxenes contained in these rocks form pseudomorphic bastite textures. The formation of typical mesh texture from olivine is most concentrated in areas of low orthopyroxene density.

Tiny magnetite-serpentine veins are present, emerging from the mesh in serpentinized harzburgite. The largest of these are macroscopically visible in the core where black veins circle around pyroxene pseudomorphs.

Examples of larger through-going veins are shown in Figure F31. Subparallel serpentine veins (Fig. F31A, F31B; Sample 56Z-2, 77–79 cm) emerge in close relation to the prevalent mesh texture but form long-range vein networks. In places, these veins contain intraveinous magnetite (Fig. F31C, F31D; Sample 15Z-2, 46–49 cm). In some intervals such veins form subparallel sets, through-going orthogonal crosscutting networks, or "Frankenstein" structures (Fig. F31E; Sample 106Z-4, 0–5 cm). In "crosscutting Frankenstein" texture, a large central vein is orthogonally cut by numerous smaller veins. In Hole BA3A, these veins exhibit macroscopic color variations from green to dark green for the composite or banded core and crosscuts of various colors (white, waxy white). In places, both vein networks of white type Sf and Frankenstein veins (occurring either as single veins or vein sets) have a brown halo. In thin section, the possible presence of brucite within these halos is inferred from orange-brown discoloration in mesh rim serpentine veins and mesh centers (Fig. F31F; Sample 13Z-2, 29–32 cm) in pervasively serpentinized mesh regions adjacent to vein/vein networks, as observed elsewhere (Kahl et al., 2015). However, the small grain size of serpentine and brucite makes unambiguous microscopic identification difficult. Brucite was identified

in the brown-haloed veins in the harzburgites by XRD (**Supplementary material** > **F3_XRD data**).

Opaque minerals

Reflected light microscopy of opaque phases indicates that the most common sulfides in Hole BA3A are Ni sulfides (e.g., heazlewoodite and pentlandite) and chalcopyrite. Sulfide minerals including pentlandite, heazlewoodite, and chalcopyrite in thin section occur mainly in macroscopic serpentine veins and/or in the background mesh veins, suggesting that they are part of the alteration assemblage (Fig. F32A; Sample 31Z-1, 35–38 cm; Fig. F32B; Sample 79-2, 36–41 cm). Highly reduced assemblages, including native copper and awaruite, rimmed by magnetite were identified in some samples throughout Hole BA3A (Fig. F32C; Sample 33Z-1, 78–82 cm). In some highly serpentinized samples, sulfides are finely distributed in the matrix and could not be identified microscopically.

Magnetite occurs as dispersed grains (<0.05 mm) in fine-grained veins cutting across the mesh texture (Fig. F32D; Sample 15Z-2, 46–49 cm) and/or intergrowths with alloys, native copper, and Ni sulfides (Fig. F32B; Sample 79-2, 36–41 cm). Ferritchromite was observed in margins and within fractures of some chromian spinels in most samples (Fig. F32E; Sample 12Z-2, 0–5 cm).

XRD results for vein samples

XRD analyses of material from Hole BA3A were performed using a PANalytical CubiX^3 X-ray diffractometer. A compilation of the spectra and sample locations in the core is given in **Supplementary material** > **F3_XRD data**. Results of XRD analyses of altered peridotites and magmatic rocks are provided in **Background description**.

The main target of the 41 XRD analyses of vein samples was to identify minerals in different vein types, especially when this was uncertain based on macroscopic core description alone. Thus, many XRD samples may be "pathological" rather than exemplary cases.

Veins identified as Sb, with waxy green color ranging from white to light green, contain serpentine as the main phase (Table T5). One of the veins identified as Sb (Sample 98Z-3, 19 cm) contains chlorite in addition to serpentine. That vein cuts a magmatic dike, in contrast to other pure-serpentine Sb veins that occur exclusively in peridotite.

Composite veins classified as Se are rich in magnetite with a noticeable fibrous structure (Samples 30Z-3, 60 cm; 40Z-3, 16 cm) and serpentine and magnesium iron oxide as other present phases. Two Se veins (Samples 33Z-2, 25 cm; 42Z-3, 37 cm) from fractured and faulted domains also have talc in addition to serpentine.

White serpentine veins classified as Sf contain serpentine as the only phase, except for Sample 33Z-2, 25 cm, which includes hydrogarnet as other phases. White vein Sample 49Z-1, 78 cm, even shows hydrogarnet as the major phase followed by serpentine.

Vein type X, rich in xonotlite, is present in veins cutting gabbroic dikes extending into peridotite, except for Sample 30Z-1, 50 cm, which also has hydrogarnet as the major phase besides xonotlite and serpentine. Other veins cutting magmatic dikes contain chlorite and amphibole in addition to serpentine. Some of these veins also show clinopyroxene identified by XRD, whereas others have minor amounts of hydrogarnet and chlorite. Brucite was not identified in any of the 41 vein samples subjected to XRD analysis.

Discussion

Near-surface gradients in fO_2 and $CaCO_3$ solubility

It is striking that vein intensity, the abundance of carbonate veins, and the abundance of waxy green, amorphous serpentine veins all decline with depth in both Holes BA1B and BA3A. The waxy green serpentine veins that are abundant in Holes BA1B and BA3A are typical of low-temperature serpentinization in other localities in Oman and elsewhere, as described more fully in **Veins** in the **Site BA1** chapter.

In addition, in both holes, hematite (and perhaps Fe oxyhydroxide) minerals are present in oxide veins and the surrounding serpentinized host rock in the upper part of the core, whereas highly reduced phases including awaruite and native copper are present in deeper parts of the core.

Although this vertical zonation in carbon content, low-temperature serpentine, and Fe^{3+}-rich oxides may be a coincidence, we hypothesize that these trends indicate that substantial alteration occurred in a low-temperature, near-surface weathering environment with a top close to the present-day bedrock surface. In this context, it is noteworthy that some of the young waxy green veins contain magnetite. If our inference is correct, that these veins formed at low temperature during near-surface weathering, this indicates that magnetite can form during low-temperature serpentinization under some conditions. This is somewhat at odds with the hypothesis that magnetite is a product of higher temperature serpentinization, whereas relatively iron-rich serpentine without magnetite generally forms at lower temperature (e.g., Evans et al., 2009; Klein et al., 2009, 2013; Streit et al., 2012).

The highly oxidized zone at the top of Hole BA3A is much less extensive (down to ~8 m) than in Hole BA1B (intermittently down to ~150 m). Also, the gradient of increasing pH with depth recorded during

geophysical logging of Hole BA3A is much steeper than in Hole BA1B, reaching pH 10.8 at ~30 m in Hole BA3A, whereas the pH in Hole BA1B had a shallow gradient from ~9 at 30 m to 10.8 at ~140 m (Fig. F33). And finally, there are two peaks in calcite vein abundance in Hole BA3A, near the surface and at a depth of ~60 m. The lower peak is present below the pH gradient in present-day water in the hole, so calcite-bearing vein abundance in Hole BA3A is not correlated with pH. This is different from Hole BA1B, in which the abundance of calcite-bearing veins declines steadily with depth and is well-correlated with pH in borehole waters.

Structural geology

Structural logging of the core recovered from Hole BA3A focused on definition and measurement of structural features and fabrics throughout the core. We present the results from core descriptions and thin section observations performed on *Chikyu* (Leg 4), based on a structural scheme defined and detailed in **Structural geology** in the **Methods** chapter. The orientation, thickness, and other characteristics of lithologic contacts and alteration veins—defined by the background group and vein group, respectively—were measured and are reported below. Deformation structures and fractures were defined, characterized, and measured, as was the peridotite fabric where observable through the overprinting serpentinization. All dips were measured relative to the core reference frame (CRF); consequently, the measurements are reported in a reference frame that is rotated ~30° compared to the mantle reference frame of the Oman ophiolite.

Crystal-plastic fabric in harzburgites

The relatively high degree of alteration present in the harzburgites makes recognition of crystal-plastic deformation difficult. In Hole BA3A, crystal-plastic fabric was defined by elongation of pyroxenes. Harzburgites in Hole BA3A exhibit strongly foliated to protomylonitic texture both in relatively shallow (e.g., Sections 49Z-3 through 52Z-1; 115.5–120.4 m) and deeper (e.g., Sections 101Z-1 through 114Z-4; 263.7–302.78 m) intervals. Most dip angles of elongated pyroxenes are near 30° (Fig. F34), independent of depth. Mainly in the interval 8.8–89.6 m (Sections 7Z-1 through 39Z-4), harzburgites show protogranular to porphyroclastic texture based on isotropic or rounded pyroxene; elongated pyroxene exhibits partially strongly foliated texture (e.g., Sections 37Z-1 through 38Z-2; 82.2–85.5 m). Harzburgites in the interval 90.2–135.0 m (Sections 40Z-1 through 56Z-4) exhibit porphyroclastic to protomylonitic texture by slightly to strongly elongated pyroxene. Figure F35 (Sample 44Z-1, 60–62 cm) shows rounded pyroxene forming porphyroclastic texture. Within the interval 134.7–176.7 m (Sections 57Z-1 through 71Z-4), harzburgites show mainly porphyroclastic texture formed by rounded pyroxene and partially strongly foliated to protomylonitic texture by intensely elongated pyroxene. In the interval 176.7–221.7 m (Sections 72Z-1 through 86Z-4), most harzburgites show porphyroclastic texture in the shallower intervals (e.g., Sections 75Z-1 through 79Z-3; 185.7–200.2 m) and strongly foliated to protomylonitic texture in the deeper intervals (e.g., Sections 84Z-3 through 85Z-4; 215.7–218.8 m; Fig. F35). In interval 221.7–263.7 m (Sections 87Z-1 through 100Z-4), mostly harzburgites show porphyroclastic texture by slightly elongated pyroxene. Few sections exhibit strongly foliated texture defined by intensely elongated pyroxene (e.g., Sections 91X-4 through 92Z-2; 236.3–238.1 m). In interval 263.7–302.78 m (Sections 101Z-1 through 114X-4), harzburgites frequently show strongly foliated to protomylonitic texture (e.g., Sections 104Z-1 through 104Z-4; 272.7–275.7 m) due to elongated and aligned pyroxenes.

Lithologic contacts

Hole BA3A is principally composed of harzburgite with dunite intercalations crosscut by variably rodingitized clinopyroxenite, gabbro, and olivine-gabbro dikes and veins. A number of primary magmatic contacts between gabbroic dikes and the host peridotite were recovered (see also **Background description**; Figs. F36, F37, F38), and orientations of 219 contact surfaces and 192 thickness measurements between the top and the bottom of the contacts were taken, including 20 magmatic contacts between harzburgite and dunite. The type of magmatic boundary varies from sharp to transitional and from straight to irregular; a majority of the contacts are irregular. The dip angle of the contacts is variable downhole, mostly oblique to the porphyroclastic fabric in the harzburgite (Fig. F34). Magmatic contacts are often characterized by alteration halos and are crosscut by veins or reworked as tectonic contacts. In places the halos obscure the primary contact and make it difficult to distinguish between the magmatic and the metasomatic contact with the host rock. Contacts have been identified and measured also when the original composition of the dike or vein is not determined. Throughout the core, the dikes and veins are typically partially to completely serpentinized or rodingitized. The uppermost dike appears at 27.8 m (Section 15Z-2) in the harzburgite. Along the core recovered from Hole BA3A, 121 dikes were measured, occurring principally in harzburgite. At 69.9 and 97.6 m depth (Sections 31Z-2 and 42Z-3), there are few dikes apart from some deformed and undetermined dikelets. The number of gabbroic and clinopyroxenite dikes increases downhole in the harzburgite.

Harzburgite/dunite contacts

The largest dunite unit is 2 m thick, occurs at ~20.75 m, and has a dip of 14° and a faulted lower contact at 22.745 m (Sections 13Z-1 through 13Z-3). Other logged lithologic contacts are mainly related to minor patches and/or lenses in harzburgite. A second large occurrence of dunite exists between 171.26 and 186.18 m (Sections 71Z-1 through 75Z-1) with 10 dunite layers. Farther downhole, no more dunite was identified by the background team. These dunite layers are mostly irregular and gradational, with the gradation occurring over ~1–4 cm (Fig. F36). These irregular and gradational contacts are often curved and typically difficult to measure. Contacts between dunite and harzburgite show dips ranging 20°–51° (maximum ~ 40°–50°), apart from two cases (20.75 m: dipping at 14°, and 84 m: dipping at 73°) (Figs. F37, F38).

Dikes and contacts with host peridotite

Gabbroic dikes

In Hole BA3A, 66 magmatic dikes (thickness > 0.5 mm) were defined by the background team, as well as a large number of small gabbro and rodingitized (garnet bearing) gabbro dikes (thickness > 0.2 mm) (Figs. F37, F38). Pyroxene-rich layers in the harzburgite were measured from 93.9 m (Section 41Z-2), where they begin to be clearly visible. In total, orientations of 219 contacts were measured related to gabbro dikes (including olivine gabbro, rodingitized gabbro, serpentinized gabbro, and garnet-bearing gabbro [82], clinopyroxenite [39], pyroxene rich-layers [45], and undetermined [31]) of magmatic origin with highly variable and altered appearance (even if their mineralogical composition is remarkably variable and not always easy to ascertain from the cores). Figures F37 and F38 show dip angles and thickness of the dikes and the pyroxene layers. In Hole BA3A, no wehrlite or leucocratic dikes were identified. The wider gabbroic dikes do not show magmatic layering (Sections 30Z-1, 42Z-3, 64Z-5, and 60Z-3). Some crosscutting relationships (Sections 100Z-3 and 96Z-3) and dike networks (Sections 74Z-4, 112Z-2, and 112Z-4) are also reported.

Clinopyroxenite dikes

Clinopyroxenite dikes or dikelets occur throughout Hole BA3A (Figs. F37, F38), except for intervals 69.9–147.8 m (Sections 31Z-2 and 61Z-2) and 201.6–223.1 m (Sections 80Z-2 and 87Z-2). The uppermost recovered dike is located at 27 m depth (Section 15Z-1) and is completely deformed; the deepest one occurs at 300.9 m (Section 114Z-2). The thickness of clinopyroxenite dikes mostly ranges 0.2–1.8 cm, with the exception of one larger dike (9.5 cm at 26.99 m depth; Section 15Z-1). They show sharp and straight contacts when their grain size is <1 mm; however, when coarse grained, they have mostly irregular contacts (Fig. F36). The dip angles of pyroxenite dikes range 10°–65° throughout Hole BA3A (Figs. F37, F38) and appear to decrease at 201.63–300.9 m. The orientation of pyroxenite dikes is usually discordant with respect to the peridotite foliation (Fig. F34).

Gabbro dikes

Apart from an interval at 69.9–97.6 m, gabbroic dikes or dikelets occur throughout all of Hole BA3A (Figs. F37, F38) (Sections 31Z-2 and 42Z-3). The intrusive contacts of gabbro dikes and dikelets (including rodingitized gabbro) are mostly irregular and generally have irregular or sharp top and bottom contacts (Fig. F36). Gabbroic dikes occur throughout the recovered cores with the first occurrence at 27.8 m (Section 15Z-2) and the deepest at 299.6 m (Section 113Z-4); thicknesses range 0.2–14.1 cm, decreasing with depth (Fig. F37). The widest dike (14.1 cm thick) occurs at 66.48 m (Section 30Z-1) (Fig. F37). The dip angles of gabbroic dikes range 14°–75° (maximum = 30°–40°) (Fig. F38). The dip distribution with depth downhole is relatively homogeneous (Fig. F38). The orientation of gabbro dikes is mostly discordant with respect to the peridotite foliation.

Pyroxene-rich layers

Pyroxene-rich layers appear in the harzburgite unit and are clearly visible at 93.9–278.7 m (Sections 41Z-2 and 106Z-1). Their contact with the host harzburgite is always gradational (Fig. F36). They occur frequently throughout the core (Fig. F37), with a thickness ranging 1–13.5 cm (majority = 1–5 cm). Their thicknesses increase with depth at 93.9–145.9 m and do not vary much farther down to 278.7 m (Section 106Z-1). The largest reported pyroxene-rich layer occurs at 185.4 m depth and measures 28.5 cm in thickness (Fig. F37; Section 74Z-4). Dip angles of these layers are relatively similar in the upper part of Hole BA3A (19 layers with dip angles of 35°–50°) but become more variable below 195 m (26 layers with dip angles of 15°–50°; see Fig. F38). The orientation of the pyroxenite-rich layers in the core is usually discordant with respect to the peridotite foliation (Fig. F34).

Deformation structures

Deformation structures and zones were observed throughout Hole BA3A with variable intensity, morphology, and frequency. The deformation is dominated by brittle features and is mostly accommodated by shear veins and fault or cataclastic zones. Semibrittle deformation is not frequently observed in the upper part of Hole BA3A; however, semibrittle or crystal-plastic shear zones do increase in abundance in the lower 100 m of the hole and are often associated with gabbroic dikes. The orientations (in the CRF), damage zone thickness, intensity, and

downhole distribution of deformation structures in Hole BA3A were logged, and the fracture and vein density was assessed in intervals throughout the core (see **Structural geology** in the **Methods** chapter).

In total, 418 deformation features or zones were logged. The orientations of veins and vein sets that were not interpreted to have accommodated shear were recorded separately and are discussed at the end of this section. The data on deformation structures are summarized in Figure F39, which shows the damage zone thickness of each structure (Fig. F39B), along with intensity (Fig. F39C) and a plot of the fracture/vein density with depth (Fig. F39D). A lithologic log of the hole is also given for correlation, with fault and cataclastic zones indicated (Fig. F39A). The top few meters of the hole is affected by surface-related fracturing and brecciation, limiting the amount of reliable data and measurements that can be collected on true deformation structures. The main observation to be garnered from these plots is a significant change in the character of deformation at ~120 m depth. The upper part of the hole contains numerous relatively wide and intensely deformed zones and is characterized by generally high values of vein and fracture density. Below 120 m, deformation is accommodated by fewer, narrower zones of intense deformation among a background of lower intensity deformation in general. Dip angles vs. depth of all deformation structures are shown in Figure F40. There is a very slight increase in steeply dipping structures at 150–200 m related mainly to the presence of substantial numbers of steeply dipping shear veins in this interval. This trend is also matched by the fault zone measurements. In general, however, there is little correlation between depth and the steepness of dip angles. With regard to feature type, it appears that sharp, narrow deformation structures, such as shear veins and joints, dip on average at higher angles than wider cataclastic, fault, or shear zones throughout the cores of Hole BA3A (Fig. F41).

Fault zones

Fault zones are distributed throughout Hole BA3A but are most concentrated (and generally of greater thickness) in the upper 120 m. For the fault zones recorded at very low depths this may be, to some extent, an artifact of the occurrence of surface-related deformation near the top of the core, which often bears a resemblance to true fault rock. However, care was taken to record fault zones only where some form of evidence for displacement—such as a strong planar fabric, slickensides, or the presence of facoids—was observed. Many similar heavily damaged regions were logged as cataclastic zones where the fracturing did not possess a clear planar fabric or where the presence of significant displacement was uncertain. Figure F42 displays the position of fault and cataclastic zones alongside a lithologic log of the entire hole and examples of fault zone and cataclastic zone structures. Most fault zones consisted of multiple different types of fractures and grades of cataclasis or brecciation but were logged as single zones unless clear and unequivocal crosscutting relationships were observed.

Unlike in Hole BA1B, there is no single major fault zone in Hole BA3A, and those that are present do not show clear evidence of very large displacements. That being said, their distribution throughout the hole and the fact that they represent the regions of highest deformation intensity suggests brittle fault zones are responsible for accommodating a significant proportion of strain within the sequence. This is also evidenced by the association of cataclastic zones and other deformation structures with fault zones where they occur. Fault zones in Hole BA3A range in thickness from 80.0 cm to 0.7 cm. Fault zones logged in the middle part of the hole (100–200 m depth) typically have slightly steeper dips than those above and below, correlating with an abundance of steeply dipping shear veins in this region (Fig. F40). No strong correlation between depth and thickness was observed.

Shear veins and slickenlines

Shear veins are by far the most abundant deformation feature in Hole BA3A with a total of 253 logged. Similar to Hole BA1B, veins are present in large quantities throughout the hole and many also accommodate significant strain. Shear veins could be distinguished from nonshear veins by the presence of mineral lineations and polished surfaces (Fig. F43), by the apparent displacement of a dike or another vein, or in some cases, by the presence of riedel-type fractures and veinlets cutting diagonally across the body of the vein. Shear veins are also generally straighter, more planar features than other veins, although they were sometimes observed to be anastomosing or splayed. A commonly recovered feature in Hole BA3A is parallel sets of thin white riedel shear veins that are not associated with a larger main vein (Fig. F43). These sets range from 54 cm wide to just a few narrow veins within 1 cm and consist of short incipient veinlets a few millimeters to a few centimeters long, stacked in en echelon arrays. Such vein sets are inferred to represent a fairly homogeneous distribution of strain within the host rock, especially where they occur in wide decimeter-scale bands.

The shear veins in Hole BA3A are generally low-intensity deformation features with a mean apparent offset of 2 cm (where an offset was present and measurable). It should be noted however that large displacements are not observable in drill core (largest observed was 6.5 cm) and that in the majority of cases where no apparent offset could be measured,

this was likely because it was greater than the width of the borehole. Despite their low intensity, the high abundance of shear veins make them an important component of the deformation history of the harzburgites of Hole BA3A, potentially accommodating a significant amount of strain distributed throughout the hole. Shear veins occasionally contain clear lineations or slickenlines on exposed surfaces that were measured to yield information on the shear sense of that plane. Plunges are generally steep (mostly >30°) in the upper part of the hole but become shallower (mostly <40°) below ~120 m (Fig. F44), coinciding roughly with the change in deformation intensity previously described. A few steep plunges are measured again at the very base of the hole, where the fracture intensity also increases. The plunge of a shear vein lineation can be plotted against the dip of its plane to give an indication of the shear sense (dip-slip/strike-slip/oblique-slip) of the structure (Fig. F44). In Hole BA3A there are more dip-slip planes than strike-slip, although interestingly the steepest dipping planes are mostly strike-slip in character.

Shear zones

Shear zones were logged where semibrittle or crystal-plastic deformation was believed to have occurred. They are not a common feature throughout most of Hole BA3A; however, their distribution is strongly concentrated within the lower 100 m of the core (Fig. F40). Their thickness ranges from 27 to 0.1 cm (mean = 3.7 cm). Narrow shear zones are often associated with the upper or lower surfaces of dikes, indicating that they seemingly exploited the rheological discontinuity. Microstructural analysis of one of these narrow shear zones (interval 64Z-5, 22–26 cm) revealed much of the shear zone to be composed of fibrous serpentine with a strong crystallographic preferred orientation (Fig. F45). Larger shear zones not associated with dikes were encountered at 81 and 214 m depth and most likely contain a significant element of brittle or semibrittle deformation (Fig. F43). These wider structures are characterized by strong foliation in the host rock and apparent crystal-plastic flow but also by significant fracturing and some cataclasis, making the distinction between these and fault zones somewhat ambiguous at the macro scale.

Cataclastic zones

Cataclastic zones were logged in Hole BA3A where regions of brittle damage or brecciation were observed but displacement or faulting could not be confirmed. In this way, zones of extensive in situ cataclasis or fracturing could be logged without assigning a fault zone character. That being said, in many cases where cataclastic zones were logged, they are closely associated with identifiable fault or shear zones. The downhole distribution of cataclastic zones and their thicknesses are plotted in Figure F42 as blue bars, and fault zones are given in red. In total, 40 cataclastic zones were logged, distributed fairly evenly throughout the core. They vary in character from narrow fracture networks to large sections of highly fractured and damaged material. The damage zone thickness of cataclastic zones varies from 53 to 0.6 cm (mean = 5.3 cm).

Joints

Joints were logged in Hole BA3A where fractures were observed with no observable mineral vein fill. Open fractures were not logged as joints if they were believed to have been derived from the drilling process or from fracturing during core processing. Drilling commonly produces core axis–normal fractures or isolated upright conjugate pairs of fractures. In addition, fractures readily form along preexisting planar features such as dikes, shear zones, or shear veins, and these structures were logged as such rather than as joints. Joints are somewhat uncommon throughout the sequence of Hole BA3A, as most fractures are better described as veins with precipitation of serpentine, carbonate, or other minerals. The joints that were logged are typically 1–2 mm wide and show a slight tendency towards a decrease in dip angle with depth.

Orientations of alteration veins

Orientations of 1141 alteration veins were measured in Hole BA3A. Of these, 45 are carbonate or carbonate-bearing veins and 1069 are serpentine veins. Individual veins, vein sets, and vein networks were defined and grouped into carbonate-serpentine veins (type Ca), carbonate veins (Cb), xonotlite veins (X), and different serpentine vein generations based on their color and texture (types Sa, Sb, Sc, Sd, Se, and Sf) by the vein team (Fig. F46; see Veins). No changes to this vein type classification have been made in comparison to Hole BA1B. Crosscutting relationships are similar to those in Hole BA1B, with high ambiguity in apparent age relations between different vein generations, apart from a clear distinction between the earliest black serpentine veins (Sa) and the youngest waxy green serpentine (Sb) and carbonate(-bearing) vein generations. Composite vein generations (Se) often show reopening or exploitation of previous serpentine vein generations by younger serpentine and carbonate veins.

Orientation measurements are given in the same data set as that used by the vein team as true dip and apparent dip azimuth in the CRF. Dip azimuths and true dips of vertical and subvertical veins could rarely be measured accurately but were included for statistical analysis of dip angles using generic dip azimuth/dip values (0/89.9° and 0/85°). In intervals with high vein densities (see Veins), measurements were limited to orientations of single veins and rep-

resentative orientations in systematic vein sets. For conjugate vein sets of the same vein type, we measured two or three predominant orientations where well defined. Chaotic, strongly branching, or anastomosing vein networks, polygonal (e.g., "turtle"-textured; see **Veins**) networks, and veins that do not crosscut the core surfaces (e.g., small ladder crack/"Frankenstein" vein sets of type Sb; see **Veins**) were not measured. Variations in dip angles of all measured veins with depth are shown in Figure **F46**, and the dip distributions of carbonate(-bearing) veins and selected serpentine vein types are additionally illustrated in rose diagrams (Fig. **F47**). Dip angle distributions presented in rose diagrams have been weighted using the vein density index (defined as values 1–5; see **Veins**) as a factor in order to accommodate for the fact that only one measurement was taken in systematic vein sets. However, high-density vein sets with more than 5 veins/10 cm are still underrepresented in the rose diagrams shown in Figure **F47**.

Dip angles of alteration veins in Hole BA3A are variable, similar to Hole BA1B, showing on average a slight steepening with depth (fewer veins dipping < 45° downhole; Fig. **F46**). Minor shallow-dipping veins (dips < 30°) occur down to 70 m and below 230 m but are rare at 70–230 m. The apparent lower abundance of relatively shallow dipping veins in the latter interval coincides with lower fracture/vein intensity and lower deformation intensity compared to the uppermost and lowermost parts of Hole BA3A (Fig. **F39**). Like in Hole BA1B, some subhorizontal and shallow-dipping carbonate(-bearing) veins occur in the uppermost 30 m of Hole BA3A but are rare further downhole (Fig. **F47**). Below 60 m depth, dip angles of carbonate-bearing veins are similar to those of serpentine veins, with dips scattering at 40°–80° (Fig. **F47**). No major differences in dip angles with depth can be discerned for the different types of serpentine veins (Fig. **F47**). As in Hole BA1B, waxy green serpentine veins (picrolite; type Sb) are on average somewhat shallower dipping (mean dip = 48°) than the other serpentine vein types. All serpentine vein types show a slight bimodal distribution of dip angles in rose diagrams (Fig. **F47**), in accordance with the common observation of conjugate sets and en echelon and riedel shear sets.

Microstructural observations

As the most common and widespread deformation structures in Hole BA3A, shear veins and narrow faults with observable displacement were targeted for more detailed structural analysis. These features were also deemed to be the ones for which microscale observations would be the most useful with regard to determining the mechanisms and chronology of deformation.

One form of shear vein that was often observed in Hole BA3A is 2–3 mm wide green serpentine veins with Riedel-type shear fractures forming diagonally across their width and sets of short green veinlets arrayed perpendicular to their margins. Microstructural analysis shows this vein type to be composed of concentric bands of fine-grained serpentine layers, typical of composite veins that have been sheared along numerous planes aligned orthogonal to the vein margins (Fig. **F48**). Individual bands or sequences of bands can be traced across these shear planes or microfaults, revealing them to have a range of offsets roughly proportional to their thickness, with larger offsets evident across the thicker, more defined shear planes. In many places the serpentine layers exhibit microfolding structures, suggesting an incipient crystal-plastic phase of deformation before these folds develop into through-going shear planes. The overall effect of the displacement across these planes is stretching of the vein material through domino-type faulting, as with stacked normal faults. The short green veins arrayed perpendicular to the vein margins seem to be associated with many of the largest of these microfault planes and originate at the terminations of the microfault planes (Fig. **F48**). These Frankenstein-type veins are therefore inferred to be syntectonic features that form as Mode 1 fractures in the host rock during shear of the vein. What is also clear from the observed relationships is that the formation of the composite vein must predate the deformation in order for such continuous banding to have been formed and subsequently faulted. This serves as evidence that fine-grained, preferentially aligned serpentine in veins is a valid reciprocal for the localization of strain throughout the sequence of Hole BA3A.

Contrasting but similarly important deformation structures in Hole BA3A are very narrow faults with displacements of several centimeters. These structures accommodate greater displacement than the veins described above and within a significantly narrower zone of deformation. Many are logged as shear veins with observable displacement, as they contain mineral fill and it is not clear at the macroscale whether veining or faulting occurred first. Microstructural analysis of one such structure (Sample 101Z-2, 40–43 cm) reveals a very sharp slip surface <0.5 mm wide that has offset a small dike by 2 cm (Fig. **F49**). Symmetric syntaxial growth of undeformed serpentine crystals occurred to varying degrees along its length, highlighting a slightly undulating surface with voids and promontories. These observations suggest the observed offset was accommodated during a single or at most very few deformational events. Sample 111Z-2, 20.5–23.5 cm, potentially represents a more mature example of a similar feature, in which the deformation has been

accommodated within a narrow network of anastomosing slip surfaces forming a slightly wider (~3 mm) deformation zone (Fig. F49).

Carbonate veins in the uppermost 10 m of Hole BA3A exhibit a different kind of brittle microstructure that is not related to deformation but exhibits similar localized fragmentation as fault and cataclastic zones. Here, subhorizontal carbonate veins show fragmentation of serpentinite clasts by Ca carbonate veins, forming localized carbonate-serpentine breccia domains (Fig. F50; Sample 3Z-3, 33–37 cm). Close to fragmented serpentinite clasts, carbonate crystals occur in open cavities, suggesting that brecciation may have been driven by crystallization as opposed to stress-related brittle deformation.

Summary

Here are summarized some of the main outcomes from the structural logging. Hole BA3A is mainly composed of harzburgite with minor clinopyroxenite and pyroxene-rich layers cut by gabbroic dikes or veins. The abundance of gabbroic dikes recovered (<200) is quite different than from Hole BA1B (>700). Like in Hole BA1B, the gabbroic dikes in Hole BA3A seem to play an important role in localizing deformation and fluid circulation. They are often associated with sheared or fractured/veined contacts. Sheared and veined contacts show repeated episodes of crack and seal and/or slip, testifying to multiple phases of fluid infiltration and fluid-rock interaction accompanied by episodes of deformation at different temperatures. Pyroxene-rich layers are often associated with sheared or fractured/veined contacts and may also play an important role in localizing deformation and fluid circulation. Deformation in Hole BA3A has taken place on a variety of different structures and at a range of scales. The most abundant deformation structures observed throughout the core are shear veins (268 identified). Whereas these are typically low-intensity structures, their high abundance implies an important role in the deformation history of the predominantly harzburgitic sequence, in particular as a mechanism for distribution of small amounts of strain. Their abundance relative to other structure types may also be related to the fact that several different types of features fell under the category of shear veins. Microstructural analysis of structures displaying both shear and vein characteristics revealed that some formed first as slip surfaces, along which vein minerals subsequently precipitated, whereas others were initially undeformed veins along which strain was localized, possibly due to the weakness of a plane of preferentially aligned serpentine. Fault zones and cataclastic zones contrast with shear veins in that they were infrequent but high-intensity structures that each serve to accommodate a large amount of strain. They dominate deformation in the upper ~120 m of the hole but are somewhat sparser below, where shear veins and narrow crystal-plastic or semibrittle shear zones become the most important deformation structures. In contrast to Hole BA1B, no major fault zones with large inferred displacements were observed.

Geochemistry

Whole-rock chemical analyses were performed on 62 variously altered samples collected from Hole BA3A: 58 harzburgites, 2 dunites, and 2 gabbros. A total of 31 samples were selected by the shipboard science party as representative of the lithologies recovered from Hole BA3A. A thin section was taken systematically next to each geochemistry sample (see supplemental Tables ST1, ST2). The 31 samples collected on-site every 10 m during operations were powdered and analyzed at the University of Southampton (see Geochemistry in the **Methods** chapter). A thin section was taken for each on-site sample and XRD analyses were also performed on each on-site geochemistry sample for detailed mineral characterization.

LOI, CO_2, and H_2O contents

The samples recovered from Hole BA3A yielded loss on ignition (LOI) values with minor variability. LOI values for all recovered samples correlate with lithology: LOI values of harzburgites throughout the hole range 9.3–14.4 wt% (average = 12.6 wt%), whereas LOI values for the two sampled dunites are higher, 13.5 and 15.9 wt%. The two gabbro dikes sampled have LOI values of 10.2 and 12.7 wt% (Figs. F51, F52). Concentrations of H_2O correlate well with the measured LOI values, whereas CO_2 concentrations are poorly correlated (Fig. F52), indicating that the majority of volatile loss is due to dehydration of secondary hydrous minerals.

The average H_2O concentration in Hole BA3A core samples is 13.1 wt%, which indicates high degrees of serpentinization. It is however lower than the average water concentration in overlying dunitic rocks measured in Hole BA1B (16.2 wt%; see Geochemistry in the **Site BA1** chapter). The highest water content was recorded in harzburgite Sample 83Z-1, 0.0–7.0 cm (209.7 m) with an H_2O concentration of 14.9 wt%, whereas the lowest value observed for Hole BA1B was harzburgite Sample 14Z-3, 39.0–44.0 cm (25.8 m) with an H_2O concentration of 9.7 wt%. These samples are highly serpentinized and contain also brucite as confirmed by XRD analyses (see Supplementary material > **F3_XRD data**).

The average concentration of CO_2 in all Hole BA3A samples is 0.26 wt%, with a minimum of 0.15 wt% in harzburgite Sample 87Z-3, 77.0–83.0 cm (228.3 m) and a maximum of 0.6 wt% in harzburgite Sample 27Z-1, 0.0–5.0 cm (59.7 m). The average CO_2 con-

centration of the harzburgites is 0.25 wt%, whereas the two sampled dunites both contain CO_2 concentrations of 0.37 wt%. For the two sampled gabbros, CO_2 concentrations are 0.58 and 0.23 wt%. It should be noted that gabbro Sample 112Z-3, 90.0–95.0 cm (CO_2 concentration = 0.23 wt%) was taken on site and contains both harzburgitic background and a 1 cm thick gabbro dikelet. The 4 samples with the highest CO_2 concentrations (i.e., 3 harzburgites and 1 gabbro) occur at relatively shallow depths above 100 m, and these high values correlate to high $CaCO_3$ content (0.31–1 wt%). These results are consistent with XRD (identification of carbonate minerals; see **Supplementary material** > **F3_XRD data**) and with VCDs indicating that carbonate veins were observed only in the upper ~100 m of Hole BA3A. At ~69 m, $CaCO_3$ content appears to decrease systematically downhole to 0.18 wt%. The two sampled dunites at 175 and 186 m are exceptions, as they retain elevated carbonate levels (0.72 and 0.87 wt%) compared to the background harzburgites.

Gabbro Sample 31Z-1, 0.0–0.5 cm (68.7 m), and harzburgite Samples 27Z-1, 0–5 cm (59.7 m), and 34Z-1, 6–11 cm (77.8 m), show total organic carbon (TOC) concentrations of 0.07, 0.049, and 0.039 wt%, respectively. TOC is calculated as the difference between total carbon and total inorganic carbon. This difference is generally interpreted to represent the actual total organic carbon content, but carbon analyses of OmanDP Hole BT1B samples showed that it might also reveal the presence of magnesite, which is not measured using the classical on-board inorganic carbon analytical techniques (see **Geochemistry** in the **Site BT1** chapter). Further on-shore studies will allow determination of the actual contribution of organic carbon to the carbon budget for those samples.

Nitrogen and sulfur were below detection limits in all Hole BA3A samples.

Whole-rock major and minor elements

Hole BA3A samples are characterized by a generally narrow range of compositions, reflecting the dominantly harzburgitic lithology recovered along the core (Tables **T6**, **T7**). As illustrated in Figure **F51**, major element compositions correlate with the lithologic units sampled downhole. In order to detail the chemical composition along Hole BA3A, three main lithologic groups were defined: harzburgite, dunite, and gabbro.

Harzburgites, representing 58 of the 62 Hole BA3A samples, display a narrow range of Mg# (defined as the molar ratio of Mg to Mg + Fe, with all Fe calculated as Fe[II]) of 90.3–91.9 (average = 91.2). Despite such downhole uniformity, we observed a small Mg# excursion in harzburgite samples at 20.5–43.5 m (maximum Mg# = 91.9). Additionally, there is a small but discrete jump in Mg# at 249.5 m, below which measured samples yield consistent Mg# of 91.2–91.6. CaO_3, Al_2O_3, and TiO_2 concentrations in harzburgites from Hole BA3A range 0.13–2.0 wt%, 0.35–1.6 wt%, and 0.015–0.103 wt%, respectively (Fig. **F53**, **F54**).

Compared to peridotites from the Wadi Tayin (WT) Massif in the Oman ophiolite (Godard et al., 2000; Hanghoj et al., 2010), Hole BA3A peridotites have a similar composition (Fig. **F55**) in terms of Mg# (WT range = 90.2–92.74, average = 91.44), CaO concentrations (WT range = 0.02–2.50 wt%), and Al_2O_3 concentrations (WT range = 0.26–2.10 wt%). SiO_2 concentrations appear slightly enriched compared to WT harzburgites, however (WT average = 42.66 wt%; Hole BA3A average = 44.25 wt%).

The composition of the two interlayered dunite samples of Hole BA3A overlap with the Hole BA3A harzburgite samples described above. These dunites display Mg# of 91.0 and 90.6, CaO concentrations of 0.86 and 0.29 wt%, Al_2O_3 concentrations of 0.52 and 0.21 wt%, and TiO_2 concentrations of 0.023 and 0.017 wt%. The two sampled gabbros from Hole BA3A have Mg# of 89.7 and 83.2, CaO concentrations of 4.1 and 9.9 wt%, Al_2O_3 concentrations of 2.72 and 7.01 wt%, and TiO_2 concentrations of 0.20 and 1.21 wt%. Predictably, these gabbros yield the highest TiO_2 and CaO values as well as lowest Mg# of all recovered Hole BA3A samples. Compared with gabbros from previous OmanDP Holes GT1 and GT2, however, the gabbros from Hole BA3A appear to have higher MgO and Fe_2O_3 and lower Al_2O_3 and CaO concentrations (Fig. **F56**).

Whole-rock trace elements

Trace element compositions in Hole BA3A harzburgites display a wide range of variation (Figs. **F54**, **F55**; Tables **T6**, **T7**) for the elements Ni (1995–2415 ppm; mean = 2254 ppm), Co (69–104 ppm; mean = 87 ppm), Cr (1806–3988 ppm; mean = 2539 ppm), and Cu (4 ppm to a particularly enriched sample having 115 ppm; mean = 15 ppm). Although Ni concentrations appear uniform with depth, Cr slightly decreases with depth, whereas Co shows a weak positive correlation with depth (though highly variable from sample to sample). Cu data show random variability downhole but no overall correlation with depth. The two analyzed dunites have similar trace element signatures for Ni (2416 and 2669 ppm), Co (82 and 108 ppm), Cr (2601 and 1794 ppm), and Cu (16 and 9 ppm).

The Hole BA3A peridotite trace element compositions above are similar to peridotites from Wadi Tayin Massif, Oman, analyzed by Godard (2000) and Hanghoj et al. (2010) (Ni = 1957–2760 ppm, Co = 96.58–145.56 ppm, Cr = 1326–11094 ppm, and Cu = 2.9–113.4).

The two gabbro units sampled in Hole BA3A also have comparable trace element concentrations as the Hole BA3A harzburgite and dunite units (Ni = 1890 and 1083 ppm, Co = 66 and 76 ppm, Cr = 2022 and 1338, and Cu = 19 and 10 ppm). These gabbros appear enriched in vanadium (76 and 293 ppm) compared with the average Hole BA3A peridotite concentration of 41 ppm. Additionally, the gabbro Sample 112Z-3, 90.0–95.0 cm (296.02 m) appears relatively enriched in Zn (61 ppm) and Zr (21 ppm). Trace element data acquired by X-ray fluorescence (XRF) was at or below the detection limit for the elements Y, Rb, Ga, and Sc for most of the peridotite samples.

Comparison with Sites CM1, CM2, and Hole BA1B

Compared to Sites CM1 and CM2, which represent the crust–mantle transition zone (CMTZ) and were described during Leg 3 of OmanDP, Hole BA3A harzburgites show less variability in terms of Mg# (CM1 = 82.4–92.8; CM2 = 83.3–91.9). This variability may be explained by the higher frequency of distinct interlayered lithotypes throughout the harzburgites at Sites CM1 and CM2 compared to Hole BA3A. In terms of H_2O content, Hole BA3A harzburgite samples compare similarly to harzburgites of Sites CM1 and CM2 (average H_2O = 13.0 and 10.5 wt%, respectively). Major element concentrations of harzburgites in Hole BA3A also compare similarly to those measured at Sites CM1 and CM2 (CM1 average CaO = 1.1 wt%, Al_2O_3 = 0.74 wt%, TiO_2 = 0.029 wt%; CM2 average CaO = 1.0 wt%, Al_2O_3 = 0.78 wt%, TiO_2 = 0.027 wt%). Lastly, whereas downhole trends were recognized in major elements at Sites CM1 and CM2 (see **Geochemistry** in the **Site CM1** chapter and **Geochemistry** in the **Site CM2** chapter), there appears to be little correlation in changes of major element concentrations with depth for Hole BA3A harzburgites.

Compared to harzburgites sampled from Hole BA1B described during Leg 4 of OmanDP, harzburgites from Hole BA3A have a similar average Mg# (90.3 vs. 90.8). CaO content differs, however: Hole BA1B harzburgites have average CaO of 1.85 wt% vs. 1.01 wt% in Hole BA3A. Higher CaO content in Hole BA1B may be due to greater clinopyroxene content, melt interactions in highly interlayered igneous units, or more plagioclase-bearing gabbroic dikes being included in quarter-core sampling, particularly during on-site sampling where samples were chosen every 10 m without specific regard to lithology. Al_2O_3 content for Hole BA1B harzburgites is also higher, with an average of 1.27 wt% (compared with Hole BA3A Al_2O_3 average of 0.77 wt%).

Summary

A total of 62 samples from Hole BA3A were analyzed for volatile, major element, and trace element chemistry using a variety of analytical techniques on board *Chikyu*. Harzburgite samples, representing the majority lithotype of the hole, yielded geochemical compositions typical of those previously analyzed at Wadi Tayin Massif and from holes studied earlier during the Oman Drilling Project. Dunite samples from Hole BA3A yielded compositions similar to surrounding harzburgites, indicative of a formation through melt-rock interactions. Gabbro samples from Hole BA3A were determined to be refractory compared to gabbroic samples from the lower crust (e.g., OmanDP Holes GT1 and GT2).

Microbiology

Phase 2 microbiology results are reported in **Microbiology** in the **Site BA1** chapter.

Paleomagnetism

Remanent magnetization

Magnetic remanence measurements were made at the University of Iceland in 2019 on discrete sample cubes taken from the working half cores from Hole BA3A. A total of 92 discrete samples were measured, of which approximately one-third (30 samples) were thermally demagnetized and all others were subjected to stepwise alternating field (AF) demagnetization in tumbling mode to isolate the characteristic remanent magnetization (ChRM) direction. Some irregularly shaped and broken samples were omitted from measurements.

Natural remanent magnetization (NRM) intensity values range 0.015–1.8 A/m (geometric mean = 0.12 A/m) (Table **T8**; Fig. **F57**). NRM magnitudes are scattered throughout the hole. Positive NRM orientations of variable inclination predominate in the uppermost 50 m of the hole, whereas nearly all samples from greater depths have negative NRM inclinations of <34° (Fig. **F58**). Principal component analysis of demagnetization data was used to identify remanence vector components.

A stable ChRM that trends to the origin at the highest field and temperature steps was identified in 82 samples. Several samples from the uppermost 40 m of the hole had complex demagnetization behavior, seen as curved paths on orthogonal vector diagrams (Figs. **F59**, **F60**), from which no stable vector could be identified. ChRM orientations have a mean inclination of –24.6° (k = 114, $\alpha 95$ = 1.5°, n = 82) calculated using the Arason and Levi (2010) maximum likelihood method (Table **T8**). Inclinations are

largely uniform below 80 m (Fig. F58), whereas samples above 80 m have a slightly shallower mean inclination of around –17°. The direction of the ChRM vectors determined by thermal demagnetization and AF demagnetization are very similar, indicating that both demagnetization methods isolated the same remanence component.

Remanence vector components with lower coercivities or unblocking temperatures and distinct orientation compared to the ChRM could not be identified in most samples. In many cases, especially for thermally demagnetized samples, continuous changes in remanence directions occurred with progressive demagnetization due to overlapping coercivity or unblocking temperature distributions between components (Figs. F59, F60). For many other samples, the secondary components held only minor amounts of remanence and were removed after the first AF step. In both cases, it was not possible to define a separate remanence vector in addition to the ChRM.

AF demagnetization was effective in Hole BA3A samples (Fig. F59A), with >90% of remanence removed by 80 mT in nearly all samples (Fig. F59B). Median destructive field (MDF) values range 3.2–36 mT (mean = 23 mT) (Table T8). There is a weak trend of increasing MDF values with depth (Fig. F61).

Thermal demagnetization was performed up to 650°C (Fig. F60A). More than half of the samples measured still had >10% of their NRM intensity remaining after demagnetization at 650°C. Normalized curves of remanence intensity as a function of heating temperature are variable in shape, with drops in remanence intensity occurring around 300°, 500°, 550°, and 620°C in various samples (Fig. F60B). The highest-temperature component was interpreted as the ChRM if it trended to the origin. Changes in magnetic susceptibility were observed after selected thermal demagnetization steps. Bulk susceptibilities generally increased with progressive heating, reflecting growth of secondary minerals during thermal alteration of the rocks. Median destructive temperatures (MDT) range 236°–626°C (mean = 570°C) and lack any trend with depth (Fig. F61). The high MDT values indicate a mineral other than pure magnetite as the dominant remanence carrier. Because AF demagnetization was able to remove most remanence by 80 mT, a high-coercivity mineral such as hematite is not likely present. Further mineralogical analysis in these samples is needed to identify the high-unblocking-temperature magnetic phase that holds the magnetization in Hole BA3A.

Magnetic susceptibility

Bulk magnetic susceptibility

Volume susceptibility values range between 1.31 and 56.0 × 10^{-3} SI (Fig. F57, Table T9) (geometric mean = 3.3 × 10^{-3} SI). With the exception of the uppermost 30 m of the hole, which is characterized by exceptionally high bulk susceptibilities, the downhole profile of bulk magnetic susceptibility is similar to that of NRM intensity, both of which likely reflect variations in magnetic mineral concentrations.

Koenigsberger ratios, Q, range 0.088–2.7 (geometric mean = 1.3). Q values for most samples in the uppermost 50 m are <1.0. Coupled with the high bulk susceptibility values in this depth range, the Q values suggest the presence of high concentrations of ferromagnetic minerals with relatively low remanence stability (Fig. F57; Table T9). Below 50 m, Q values are generally >1.0, indicating greater remanence stability and smaller contributions from induced magnetization to total in situ magnetization.

Anisotropy of magnetic susceptibility

Anisotropy of magnetic susceptibility (AMS) determinations were performed on all discrete samples prior to stepwise demagnetization to characterize the shape-preferred orientations of magnetic minerals in the core samples. Magnetic fabrics are dominantly characterized by magnetic foliations, although fabric shapes range from strongly oblate (T = 0.87) to strongly prolate (T = –0.87) (Fig. F62A). Many samples are distinctly triaxial, as seen by small T values associated with high degrees of anisotropy (Fig. F62A). Fabric intensities indicated by the P' parameter are moderately strong throughout the hole (mean = 1.09). The degree of anisotropy is not strongly correlated with bulk susceptibility (K_{mean}) (Fig. F62B).

K_{max} axes are consistently oriented subhorizontally (average inclination = 22°) (Fig. F62A). Furthermore, the K_{max} axes display tight clustering near the ±X direction of the CRF (Fig. F63). K_{min} axes are dispersed along a plane normal to the K_{max} maxima (Fig. F63), approximately parallel to the ±Y direction of the CRF. Magnetic fabric orientations do not vary systematically with depth.

Physical Properties

Physical properties of ultramafic rocks and gabbroic dikes from Hole BA3A were characterized through a series of measurements on whole-round sections, section halves, section-half pieces, and discrete samples (see **Physical properties** in the **Methods** chapter). All whole-round sections were run through the X-ray computed tomography (XCT) scanner and measured for gamma ray attenuation (GRA) density, magnetic susceptibility (MS), noncontact electrical resistivity (NCR), and natural gamma ray radiation (NGR) on the Whole-Round Multisensor Core Logger (MSCL-W). Whole-round P-wave velocity was not measured because of a mechanical issue with the transmitter. We measured also point magnetic susceptibility (MSP) and reflectance spectroscopy and

colorimetry (RSC) with the Split Half Multisensor Core Logger (MSCL-C), and linescan color image with the Multisensor Core Logger (MSCL-I) on the split surface of archive halves. Thermal conductivity was measured on section-half pieces. Compressional wave (*P*-wave) velocity (V_P), electrical resistivity (IMP), and density and porosity (MAD) were measured on discrete minicube samples (20 mm × 20 mm × 20 mm). MAD measurements were also conducted on some irregular shaped discrete samples. The rock names reported in data tables correspond to the primary lithologies described in **Background description**.

Whole-round and section-half measurements

A total of 408 whole-round and archive-half sections were measured from Cores 1Z through 114Z. Downhole data plots are shown in Figure **F64** for whole-round measurements. All data are shown in supplemental Tables **ST6** and **ST7**.

X-ray computed tomography

XCT was continuously logged for all 408 whole-round core sections recovered from Hole BA3A. The XCT number of minerals is essentially a function of the density and chemical composition of the sample. Hence, XCT numbers in the core sections result from a combination of their mineral composition and pore structure in a voxel (0.625 mm × 0.175 mm × 0.175 mm). Figure **F65** shows examples of XCT images from Sections 55Z-1 and 107Z-1. The veins and fractures are visible in these images, and the dip angle can be analyzed through the whole-round image. Orthopyroxene porphyroclasts (bastite) are also identified by different XCT numbers, and the average XCT number of the deeper section (107Z-1) is markedly higher than the shallower section (55Z-1), possibly reflecting different extents of alteration.

An XCT image of the archive-half split surface, with XCT number represented on a color scale, was generated for every section. The average and the mode of XCT numbers for every scan slice (0.625 mm thick) were also computed and plotted downhole (Fig. **F64**). Average XCT number is susceptible to the effect of cracks in the core section because the XCT number of air is significantly lower than that of minerals (XCT number of air ~ –1000; see **Physical properties** in the **Methods** chapter). On the other hand, mode of XCT numbers tends to reflect a representative lithology in a scan slice, although it overlooks some minor but dense minerals (e.g., Cr-spinel).

In Hole BA3A, ultramafic rocks have average XCT numbers of ~2800. The shallow portions show lower XCT numbers, reflecting extensive weathering and high porosity. Harzburgite shows relatively high XCT numbers compared to dunite. This reflects either the higher abundance of orthopyroxene or a lower degree of serpentinization in harzburgite compared to dunite.

Because XCT numbers of a core section depend on mineral composition and porosity, the trends of the average and mode of XCT numbers clearly follow that of the GRA density in the downhole plot (Fig. **F64**). All lithologies show a relation between XCT number and GRA density. These correlations can be controlled by several factors such as modal abundances of low-density minerals (e.g., serpentine), abundance of high atomic number elements in minerals (e.g., calcium in diopside, iron in magnetite, and chromium in Cr-spinel), and pore structure. Overall, variability in the XCT number downhole trends reflects the lithologic and structural variations observed in Hole BA3A.

Colorimetry

RSC data were obtained for 408 sections of archive halves from Cores 1Z through 114Z. The specular component included (SCI) setting was used for measuring Hole BA3A cores, and this setting provides data that are closer to the actual color than those of the specular component excluded setting (SCE; see **Physical properties** in the **Methods** chapter). Color data acquired from reflectance spectroscopy and high-resolution images can provide insights into the variability of different lithologic units recovered from Hole BA3A. Lightness (L*) and chromaticity (a* and b*) variables were generated from the reflected light collected through the spectrophotometer every 2 cm. High L* value indicates lighter colors (0 represents black and 100 represents white). Directions toward more +a* denote a shift toward red from green, whereas +b* depicts a shift toward yellow from blue. High-resolution (100 pixels/cm) half-section images produced by the MSCL-I provide an alternative source of 2-D color data. Although a* and b* are nearly constant or gradually change with depth, harzburgites show markedly higher L* values compared to dunites. This is most likely because of less hydration and relatively low porosity in harzburgite.

Gamma ray attenuation density

GRA density was measured on 408 sections at a spacing of 4 cm. Data are summarized in Figure **F64**. The GRA values at shallow depth are significantly lower than the deeper sequence because of weathering and high porosity. The depth profile of the bulk density obtained by the discrete sample measurement seems to follow nearly upper bound of the GRA depth profile. Figure **F66** shows a correlation between the GRA density and XCT value. The GRA density is correlated to XCT value at density >2.5 g/cm^3, whereas it is highly scattered with low density, possibly due to relatively high porosity in the samples.

Electrical resistivity

The NCR data indicate that the cores from Hole BA3A are relatively resistive (Fig. F64). Most readings in this sequence are saturated and equal to the maximum measurable value (~85 Ω·m); therefore, actual averages of NCR for these sections could be higher than those shown in Figure F64. Although variation of resistivity is large even in a single lithology, resistivity tends to increase with depth. The resistivity of ultramafic rocks is generally related to hydration (serpentinization) resulting from the formation and connection of magnetite, suggesting less hydration in the deeper portion relative to shallow portion, similar to those observed in Hole BA1B. We note that NCR is systematically about 20× lower than the electrical resistivity measured from discrete samples (Figs. F64, F67). This can be due to low accuracy of the NCR measurements for high-resistivity samples because the instrument is designed for measuring resistivity in porous and conductive ocean wet sediments, whereas overall characteristics of NCR in a depth profile are quite similar to that of the discrete sample data.

Whole-round magnetic susceptibility

MS of whole-round core sections before splitting was measured using the MSCL-W with a 125 mm loop sensor. Whole-round MS (WRMS) values are shown in the downhole plots (Fig. F64). Magnetic susceptibility is ~1000 × 10^{-5} SI for ultramafic rocks in Hole BA3A. Figure F66 shows a correlation between MS and the inverse of NCR (i.e., the electrical conductivity) measured at the same depth. MS and inverse NCR show a linear correlation.

Natural gamma ray radiation

NGR in Hole BA3A is generally low (Fig. F64). There seems to be no or few correlations with other physical property data and structural observations.

Discrete sample measurements

P-wave velocity

P-wave velocity was measured in Hole BA3A on 100 cube samples along the three principal directions *x*, *y*, and *z* in the CRF (see Tables T10, T11; Fig. F67). *P*-wave velocity is 5.27 ± 0.09 km/s on average for dunites and 5.32 ± 0.47 km/s on average for harzburgites. *P*-wave velocity at shallow depths is relatively scattered, possibly due to weathering and relatively large variations of porosity. Harzburgites from deeper levels show a slight increase of velocity with depth, suggesting less serpentinization in the deeper portion (Fig. F67), which is similar to that observed in Hole BA1B. *P*-wave velocity of dunites is slower than that in the surrounding harzburgites.

Azimuthal anisotropy (A_V) of *P*-wave velocity is calculated as follows:

$$A_V = (V_{max} - V_{min})/V_{mean}, \quad (1)$$

where V_{max} and V_{min} are the maximum and minimum velocities and V_{mean} is the average velocity of the three orthogonal directions (Birch, 1961). The azimuthal anisotropy mostly ranges 1%–7% (Fig. F68), and anisotropy increases slightly with depth. *P*-wave velocity along the *z*-axis is slower than the other directions, consistent with that observed in Hole BA1B. The azimuthal anisotropy is possibly related to crystal fabric because V_P anisotropy tends to increase with the fabric intensity (see **Structural geology**).

Density and porosity

Bulk density, grain density, and porosity were calculated from measurements on 99 cube samples (20 mm × 20 mm × 20 mm) taken from the working half sections from Hole BA3A, approximately one sample per core and reflecting lithologic and alteration variation (Tables T10, T11; Fig. F67). Average bulk densities from Hole BA3A are 2.54 ± 0.03 g/cm³ for dunite and 2.59 ± 0.08 g/cm³ for harzburgite. As in the previous holes, the cube samples were mostly taken from relatively homogeneous intervals with fewer or no visible cracks or veins. Note that some samples exhibit an extremely high porosity (>10%), which might be due to chip-off during the MAD measurements. The highly altered or deformed samples have high porosities (up to 32%) and lower bulk densities (down to 2.20 g/cm³) and grain densities (2.50 g/cm³). Figure F67 shows that bulk density of the discrete samples increases slightly with depth, nearly consistent with the velocity data. The low grain densities of harzburgites (~2.60 g/cm³) at shallow depths suggest that olivine (density ~ 3.3 g/cm³) in these rocks is nearly 100% serpentinized (density of lizardite serpentine ~ 2.58 g/cm³; Mellini and Zanazzi, 1987). Grain density tends to slightly increase with depth, up to 2.72 g/cm³, suggesting less alteration in the deeper portions, as low as ~80% serpentinization, which is slightly higher than those observed in Hole BA1B.

The porosity of discrete cube samples ranges 0.8%–31% (mean = 1.96% for dunite and 2.35% for harzburgite). The shallow sequence shows a scattered and relatively high porosity up to 31%, reflecting weathering near the surface, whereas harzburgites in deeper portions show a nearly constant porosity or slightly decrease with depth (Fig. F67).

Relationship between densities, *P*-wave velocity, and porosity in Hole BA3A are shown in Figures F69 and F70 and compared to data from other OmanDP

holes. Bulk and grain densities and *P*-wave velocity are overall inversely correlated to porosity. Similar features are seen in ultramafic rocks from Hole BA1B (see **Physical properties** in the **Site BA1** chapter). *P*-wave velocity is linearly correlated with bulk density, whereas the correlation between *P*-wave velocity and grain density is slightly scattered (Fig. F69). A downhole plot of *P*-wave velocity with color scale of porosity reveals certain differences between the sequences and also between lithologies.

The relationship between porosity and XCT value is shown in Figure F71. Using a line fit to the Hole BA3A data for XCT < 2950, the downhole XCT data can be converted to a downhole porosity plot (Fig. F72). The major peaks in the 122 cm moving mean (blue) are related to deformation zones, whereas peaks in the 6.1 cm moving mean (red) are caused by open cracks. Notice that the porosity of discrete cube samples (Fig. F67D, F67E) tends to correlate with local minimum values in the porosity estimated based on XCT values, suggesting that the overall porosity of the core is higher than indicated by the discrete samples.

Electrical resistivity

Electrical resistivity was measured in 100 cube samples from Hole BA3A (Tables T10, T11; Fig. F67). Resistivity ranges 410–33,901 Ω·m. Samples from the uppermost 100 m show relatively scattered resistivity, whereas harzburgites from deeper portions show more or less constant resistivity. We measured both dry and wet resistivity, and wet resistivity is markedly lower than dry resistivity. The difference in dry and wet resistivity is likely related to the crack density and its connectivity in samples. The relatively large difference in dry and wet resistivity is found at shallow depths, which can be related to permeable zones related to fracturing.

Electrical resistivity has a weak correlation with bulk magnetic susceptibility of the same cube samples using the following equation (Fig. F73):

$$R = 73 \times B^{-0.76} \qquad (R^2 = 0.55), \qquad (2)$$

where R is dry resistivity of the cube sample and B is bulk magnetic susceptibility of the cube sample. Similar features are found in previous holes, including Hole BA1B. The correlation suggests a similar source between electrical conductivity and magnetic susceptibility, most likely the magnetite fraction in ultramafic rocks.

Magnetic susceptibility

Magnetic susceptibility was measured on 98 cube samples from Hole BA3A (Tables T10, T11; Fig. F67). Magnetic susceptibility ranges 0.001–0.025 ($\times 10^{-5}$ SI). Average magnetic susceptibility of cube samples from Hole BA3A are 0.0065×10^{-5} SI for dunite and 0.0043×10^{-5} SI for harzburgite. Bulk magnetic susceptibilities show no systematic variation with depth but are correlated to porosity and resistivity, where samples with high porosity and low resistivity show relatively high magnetic susceptibility. Magnetic susceptibility measured in three orthogonal directions displays contrasting patterns between bulk susceptibility and angular deviation of *x*-, *y*-, and *z*-axes. The directional deviation pattern of axial susceptibility is distinct for each axis, in which measurements along *x*-axis indicate a continuous increase in angular value, whereas no systematic deviation along *y*- and *z*-axes.

Thermal conductivity

A total of 87 measurements were taken on core pieces from the working halves from Hole BA3A (Tables T10, T12; Fig. F67). Thermal conductivity ranges 1.85–2.66 W/m·K. Thermal conductivity increases with depth, which agrees with less alteration in terms of *P*-wave velocity and grain density. This trend is similar to that observed in Hole BA1B, where thermal conductivity generally decreases with increasing depth. The thermal conductivities in this hole are similar to those reported in the harzburgites from Ocean Drilling Program (ODP) Leg 209 Hole 1274A, Mid-Atlantic Ridge 1520′N Fracture Zone (Kelemen et al., 2004). The thermal conductivity is correlated to XCT value as shown in Figure F74, suggesting that XCT value can be useful to infer alteration of ultramafic rocks.

Imaging spectroscopy

All sections of Hole BA3A were imaged onboard the *Chikyu* during Leg 3. The exception were the sections and portions of sections removed during drilling for microbiology analyses; these were not available to scan. The ~300 m of Hole BA3A core was imaged in six 12 h shifts over 3 days. A total of 406 sets of images (visible near-infrared [VNIR] and shortwave infrared [SWIR]) were acquired on core sections. A select number of images from the SWIR were processed to reflectance to check data quality. The remainder of the images, including all from the VNIR sensor, will be processed at Caltech, and mineral maps of each core section will be generated.

An example of preliminary mapping of Section 13Z-4 is shown in Figure F75. Spectral parameters in Figure F75B show the depths of three absorption features in the reflectance spectra at 2.12, 2.32, and 2.5 µm. The feature at 2.12 µm has not been definitively assigned to a vibration of a particular bond but is characteristic of serpentine (King and Clark, 1989). Absorption at 2.30–2.34 µm is present in carbonates due to the C-O bond (Hunt and Salisbury, 1971; Gaffey, 1987) and in serpentine due to a Mg-OH combination (King and Clark, 1989). Parameter

D2500 maps the drop in reflectance toward 2.5 µm; an absorption feature in carbonates is present at 2.5–2.6 µm (Hunt and Salisbury, 1971; Gaffey, 1987). In this figure, portions with more serpentine and less carbonate appear yellow to green and those with more carbonates are green to blue. Additional laboratory work is required to quantify the abundances of each mineral and validate the mineral identifications.

Downhole logging and hydrogeological testing

Downhole logging and hydrogeological testing operations and acquisition parameters for each borehole are available in Tables T55 and T56 in the **Methods** chapter. Raw and processed data from all downhole logs are available in the **Supplementary material** > **L_Wireline Logging** and in the ICDP Oman Drilling Project online data repository (**http://oman.icdp-online.org**).

References

Arason, P., and Levi, S., 2010. Maximum likelihood solution for inclination-only data in paleomagnetism. Geophysical Journal International, 182:753-771. https://doi.org/10.1111/j.1365-246X.2010.04671.x

Barrat, J.A., Zanda, B., Moynier, F., Bollinger, C., Liorzou, C., and Bayon, G., 2012. Geochemistry of CI chondrites: major and trace elements, and Cu and Zn isotopes. Geochimica et Cosmochimica Acta, 83:79–92. https://doi.org/10.1016/j.gca.2011.12.011

Birch, F., 1961. Velocity of compressional waves in rocks to 10 kilobars, Part 2. Journal of Geophysical Research, 66:2199–2224.

Cardozo, N., and Allmendinger, R.W., 2013. Spherical projections with OSXStereonet. Computers & Geosciences, 51:193–205. https://doi.org/10.1016/j.cageo.2012.07.021

Evans, B.W., Kuehner, S.M., and Chopelas, A., 2009. Magnetite-free, yellow lizardite serpentinization of olivine websterite, Canyon Mountain complex, NE Oregon. American Mineralogist, 94:1731-1734

Gaffey, S.J., 1987. Spectral reflectance of carbonate minerals in the visible and near infrared (0.35–2.55 µm): anhydrous carbonate minerals. J. Geophys. Res., 92:1429–1440. https://doi.org/10.1029/JB092iB02p01429

Godard, M., Awaji, S., Hansen, H., Hellebrand, E., Brunelli, D., Johnson, K., Yamasaki, T., Maeda, J., Abratis, M., Christie, D., Kato, Y., Mariet, C., and Rosner, M., 2009. Geochemistry of a long in situ section of intrusive slow-spread oceanic lithosphere: Results from IODP Site U1309 (Atlantis Massif, 30°N Mid-Atlantic-Ridge). Earth and Planetary Science Letters, 279:110–122. https://doi.org/10.1016/j.epsl.2008.12.034

Godard, M., Jousselin, D., and Bodinier, J.L., 2000. Relationships between geochemistry and structure beneath a paleo-spreading center: a study of the mantle section in the Oman ophiolite. Earth and Planetary Science Letters, 180(1–2):133–148. https://doi.org/10.1016/S0012-821X(00)00149-7

Hanghøj, K., Kelemen, P.B., Hassler, D., and Godard, M., 2010. Composition and genesis of depleted mantle peridotites from the Wadi Tayin Massif, Oman Ophiolite; major and trace element geochemistry, and Os isotope and PGE systematics. Journal of Petrology, 51(1–2):201–227. https://doi.org/10.1093/petrology/egp077

Hunt, G.R., and Salisbury, J.W., 1971. Visible and near infrared spectra of minerals and rocks. II. Carbonates. Mod. Geol., 2:23–30.

Kahl, W.-A., Jöns, N., Bach, W., Klein, F., and Alt, J.C., 2015. Ultramafic clasts from the South Chamorro serpentine mud volcano reveal a polyphase serpentinization history of the Mariana forearc mantle. Lithos, 227:1-20.

Kelemen, P.B., Kikawa, E., Miller, D.J., et al., 2004. Proc. ODP, Init. Repts., 209: College Station, TX (Ocean Drilling Program). https://doi.org/10.2973/odp.proc.ir.209.2004

Khedr, M.Z., Arai, S., Python, M., and Tamura, A., 2014. Chemical variations of abyssal peridotites in the central Oman ophiolite: Evidence of oceanic mantle heterogeneity. Gondwana Research, 25(3):1242–1262. https://doi.org/10.1016/j.gr.2013.05.010

King, T.V.V., and Clark, R.N., 1989. Spectral characteristics of chlorites and Mg-serpentines using high-resolution reflectance spectroscopy. J. Geophys. Res., Solid Earth, 94:13997–14008. https://doi.org/10.1029/JB094iB10p13997

Klein, F., Bach, W., Jons, N., McCollom, T., Moskowitz, B., and Berquo, T., 2009. Iron partitioning and hydrogen generation during serpentinization of abyssal peridotites from 15°N on the Mid-Atlantic Ridge. Geochimica et Cosmochimica Acta, 73:6868-6893.

Klein, F., Bach, W., and McCollom, T., 2013. Compositional controls on hydrogen generation during serpentinization of ultramafic rocks. Lithos, 178:55-69.

Lippard, S.J., Shelton, A.W., and Gass, I.G., 1986. The ophiolite of northern Oman. In Geol. Soc. Memoirs: Malden, Mass (Blackwell Sci.), 11:1–178.

McDonough, W.F., and Sun, S.S., 1995. The composition of the Earth. Chemical Geology, 120(3–4):223–253. https://doi.org/10.1016/0009-2541(94)00140-4

Mellini, M., and Zanazzi, P.F., 1987. Crystal structures of lizardite-1T and lizardite-2H1 from Coli, Italy. American Mineralogist, 72:943-948.

Miller, H.M., Matter, J.M., Kelemen, P., Ellison, E.T., Conrad, M.E., Fierer, N., Ruchala, T., Tominaga, M., Templeton, A.S., 2016. Modern water/rock reactions in Oman hyperalkaline peridotite aquifers and implications for microbial habitability. Geochimica et Cosmochimica Acta, 179:217-241.

Monnier, C., Girardeau, J., Le Mee, L., and Polve, M., 2006. Along-ridge petrological segmentation of the mantle in the Oman ophiolite. Geochem., Geophys., Geosys., 7(11). https://doi.org/10.1029/2006GC001320

Paukert Vankeuren, A.N., Matter, J.M., Stute, M., Kelemen, P.B., 2019. Multitracer determination of apparent groundwater ages in peridotite aquifers within the Samail ophiolite, Sultanate of Oman. Earth and Planetary Science Letters, 516:37-48.

Rempfert, K.R., Miller, H.M., Bompard, N., Nothalft, D., Matter, J.M., Kelemen, P., Fierer, N., Templeton, A.S., 2017. Geological and Geochemical Controls on Subsurface Microbial Life in the Samail Ophiolite, Oman. Frontiers in Microbiology, 8:56. https://doi.org/10.3389/fmicb.201700056

Rospabe, M., Benoit, M., Ceuleener, G., Hodel, F., and Kaczmarek, M.A., 2018. Extreme geochemical variability through the dunitic transition zone of the Oman ophiolite: Implications for melt/fluid-rock reactions at Moho level beneath oceanic spreading centers. Geochimica et Cosmochmica Acta, 234:1–23. https://doi.org/10.1016/j.gca.2018.05.012

Streit, E., Kelemen, P., and Eiler, J., 2012. Coexisting serpentine and quartz from carbonate-bearing serpentinized peridotite in the Samail Ophiolite, Oman. Contrib. Mineral. Petrol., 164:821-37.

Takazawa, E., Okayasu, T., and Satoh, K., 2003. Geochemistry and origin of the basal lherzolites from the northern Oman ophiolite (northern Fizh block). Geochemistry, Geophysics, Geosystems, 4(1021). https://doi.org/10.1029/2001GC000232

Figure F1. Photograph showing the BA3 drill site during coring operations, looking south from a small outcrop of serpentinized harzburgite to the north of the site. The NSHQ-14 borehole is located between the drill rig and the green core logging tent but is hidden behind the drill rig in this image.

Figure F2. Lithostratigraphic column for mode, Hole BA3A.

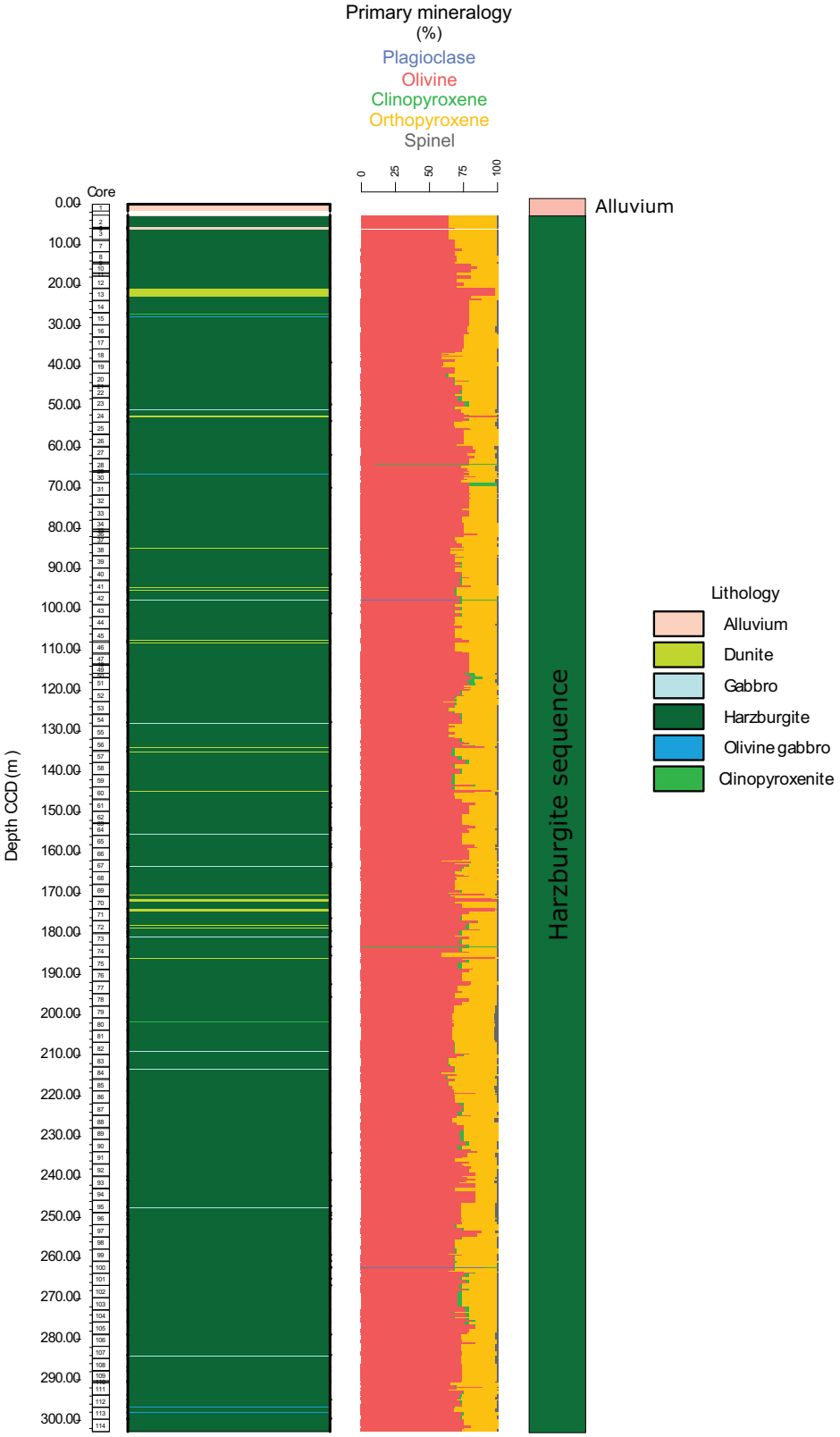

Figure F3. Pie charts showing lithology thicknesses and unit counts in percentages, Hole BA3B.

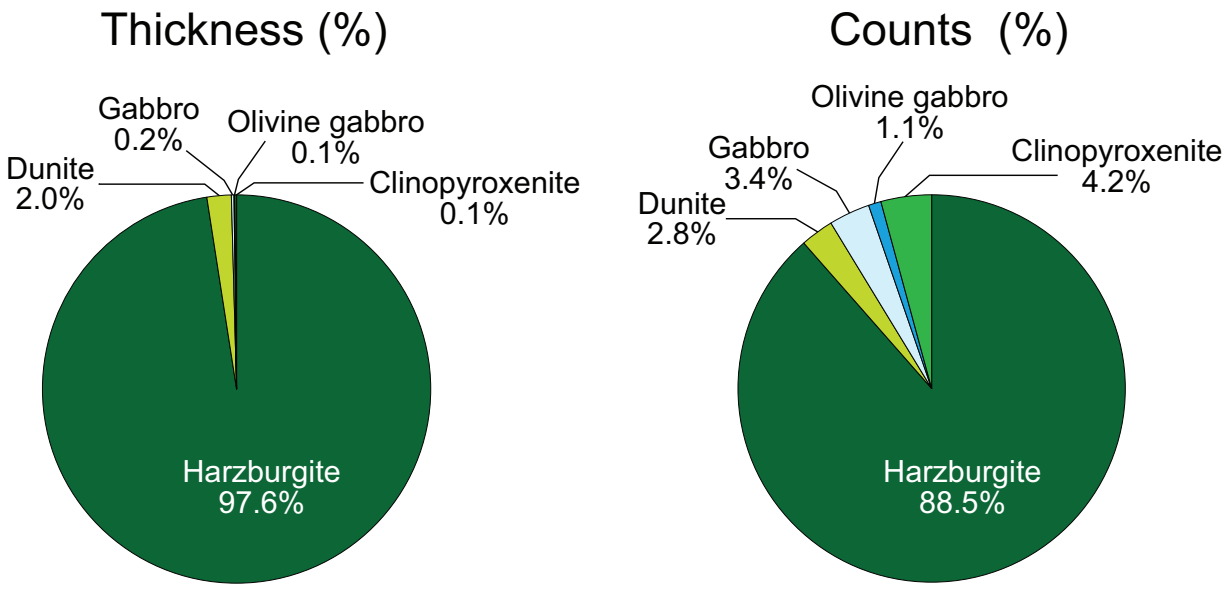

Figure F4. Breccia with carbonated matrix in the alluvium sequence, Hole BA3A (3Z-1, 41–67 cm).

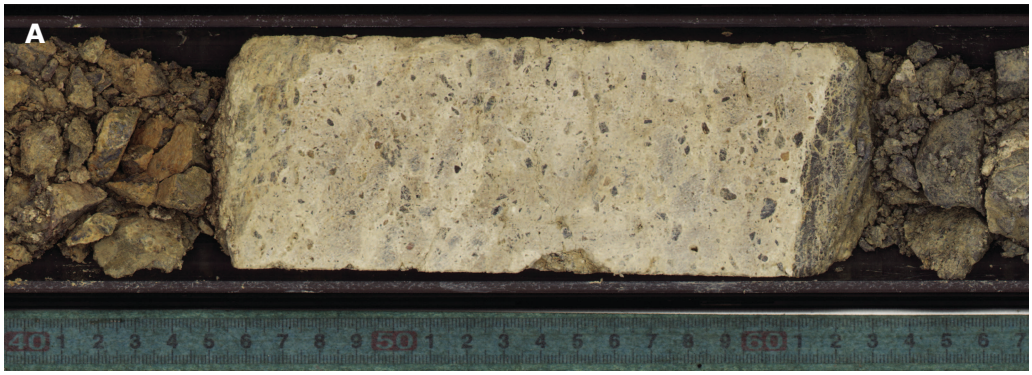

Figure F5. Downhole dunite vs. harzburgite and corresponding mineral composition evolution with depth, Hole BA3A.

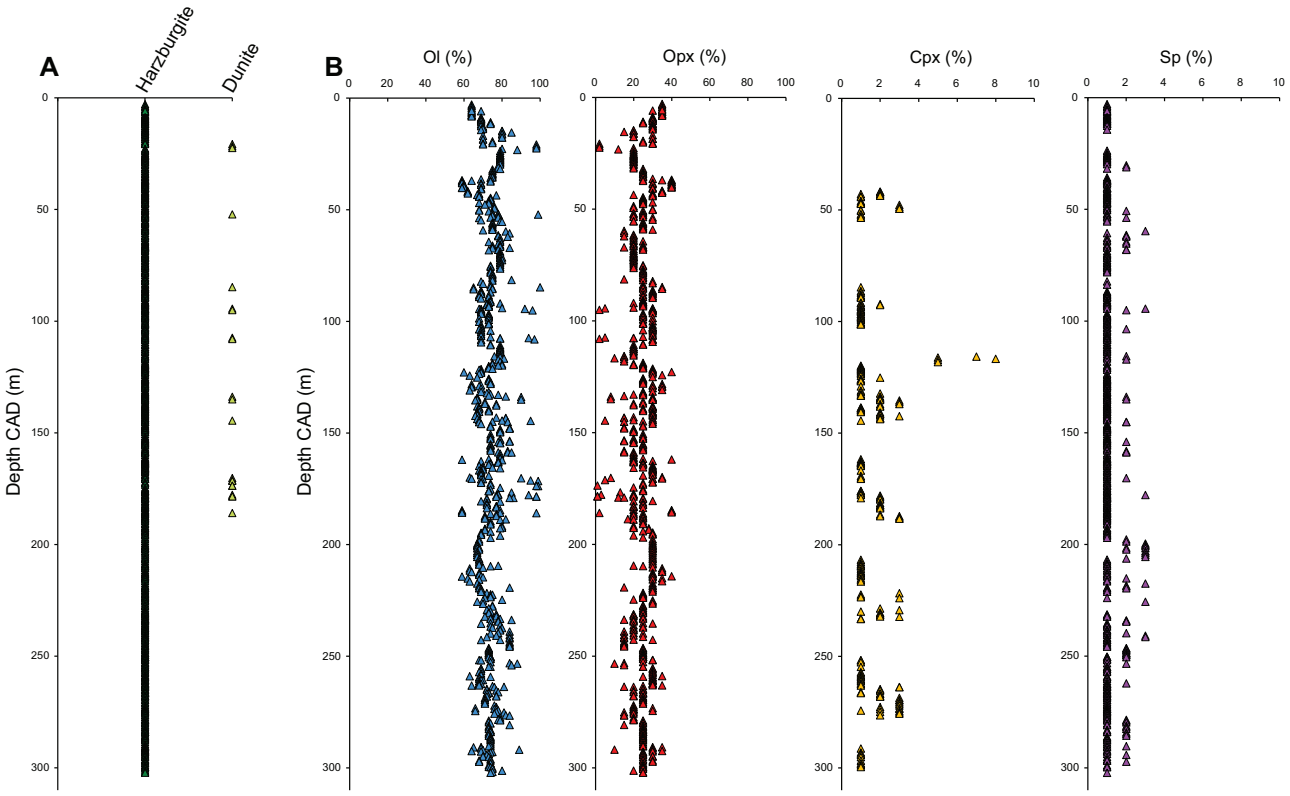

Figure F6. Typical harzburgite in harzburgite sequence, Hole BA3A. **A.** Harzburgite with weak foliation (41Z-1, 45–70 cm). **B.** Harzburgite with local bands of higher orthopyroxene concentration (18Z-3, 0–25 cm). **C.** Harzburgite with particularly high orthopyroxene concentration (74Z-4, 45–74 cm).

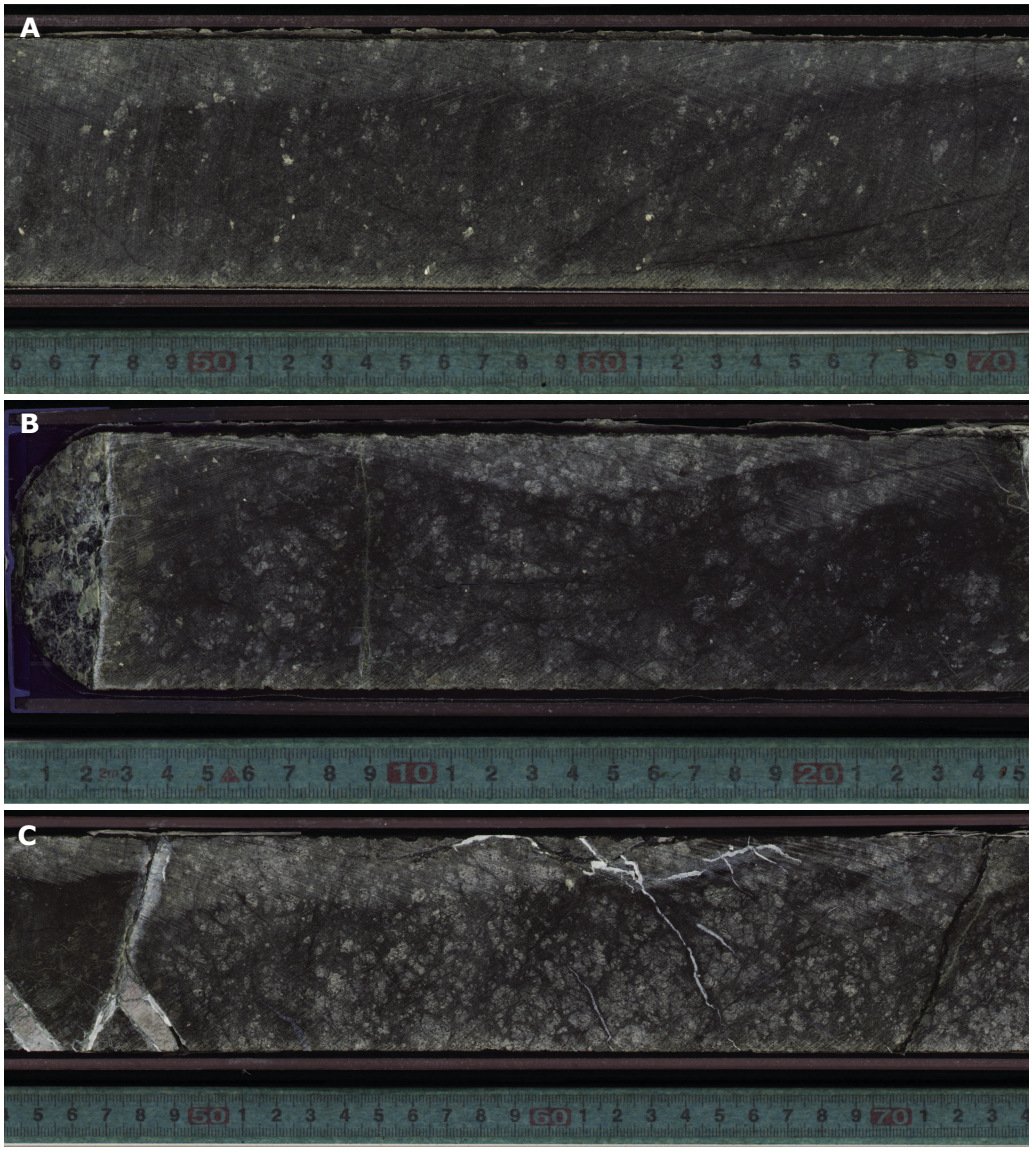

Figure F7. Harzburgite from harzburgite sequence, Hole BA3A. **A.** Section 73Z-1 marked with position of TS. **B.** TS in plane-polarized light (PPL), marked with positions of D and E. **C.** XRD result from background indicating serpentine (sp), olivine (ol), and orthopyroxene. **D, E.** Typical harzburgite with elongated orthopyroxene and vermicular spinel (D: PPL, E: cross-polarized light [XPL]) hgr = hydrogrossular, cpx = clinopyroxene.

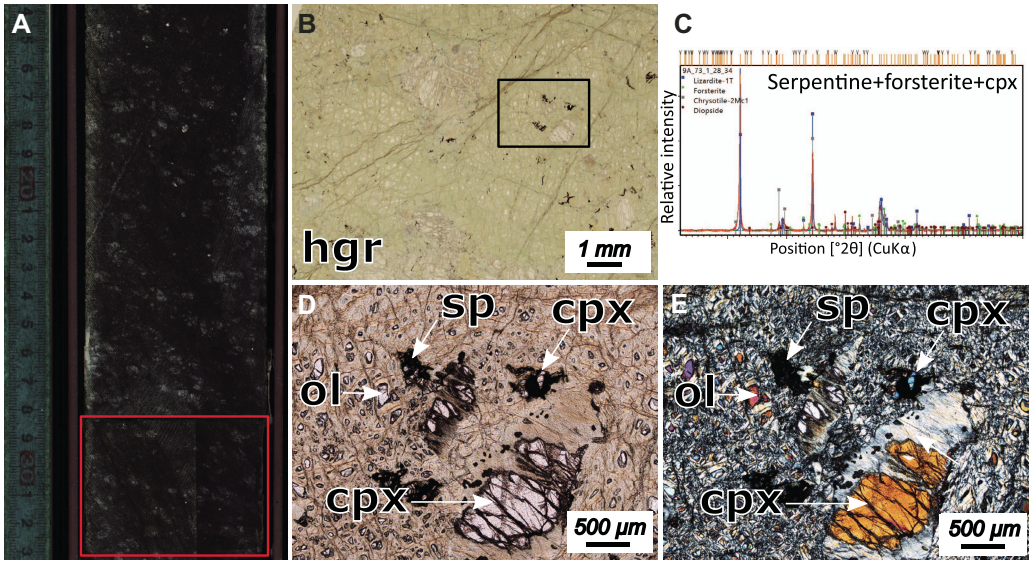

Figure F8. Harzburgite from harzburgite sequence, Hole BA3A. **A.** Section 76Z-4 marked with position of thin section (0–6 cm). **B.** TS (PPL) marked with positions of D and E. **C.** Single clinopyroxene (cpx) with altered orthopyroxene (opx) lamellae (110Z-1, 0–5 cm; reflected light [RL]). **D, E.** Orthopyroxene with clinopyroxene lamellae and multiple interstitial clinopyroxene (D: PPL, E: XPL). ol = olivine.

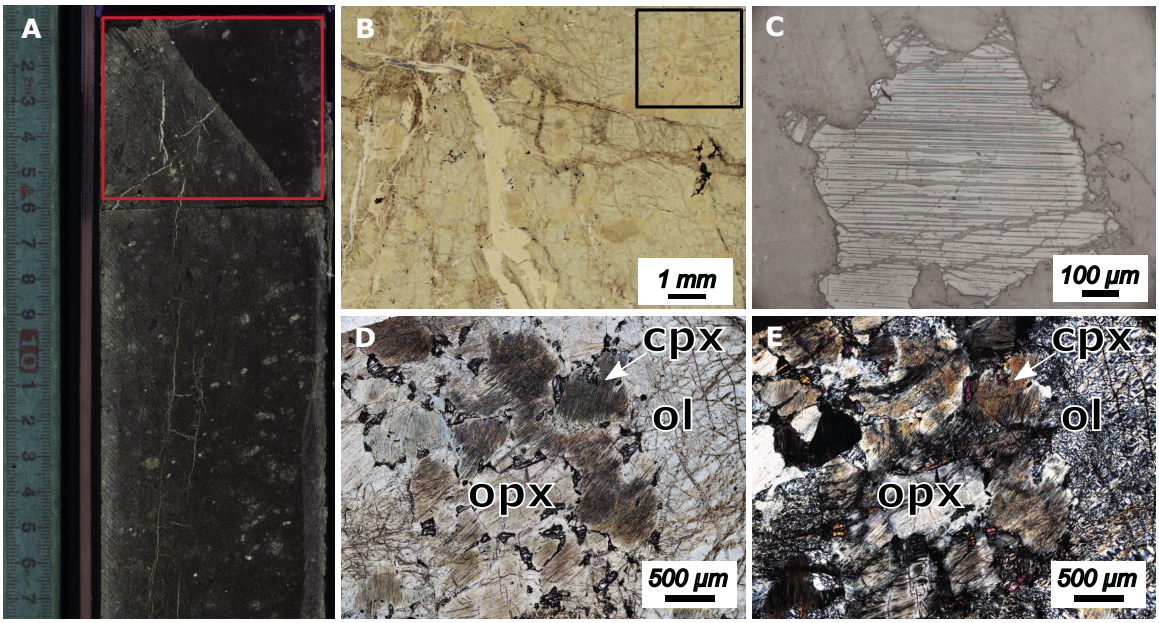

Figure F9. Harzburgite from harzburgite sequence, Hole BA3A. **A.** Section 106Z-4 marked with position of thin section (0–5 cm). **B.** TS (PPL) marked with positions of D and E. **C.** XRD result from background, indicating serpentine and clinopyroxene (cpx). **D, E.** Orthopyroxene (opx) with clinopyroxene intergrowth (D: PPL, E: XPL).

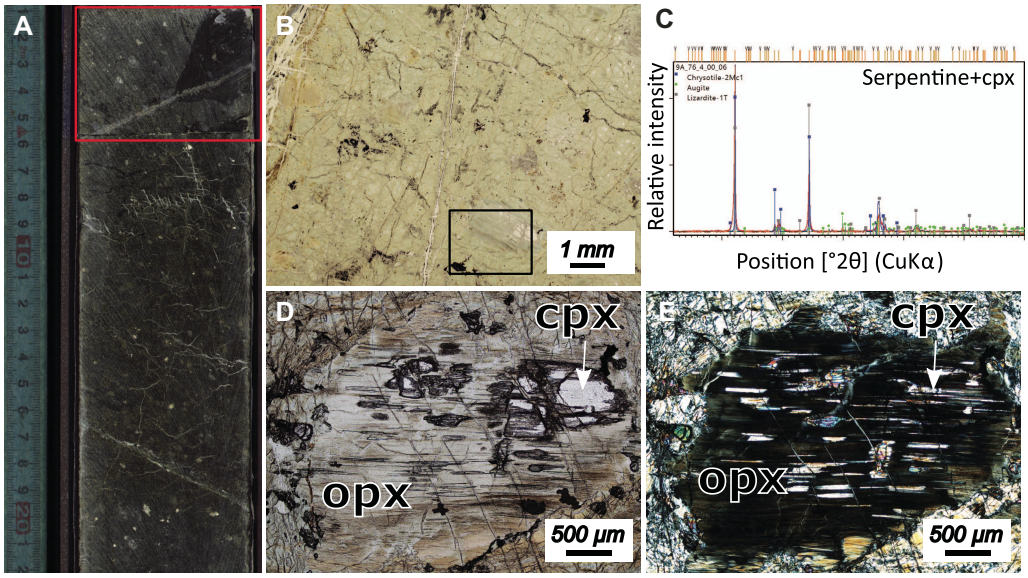

Figure F10. Harzburgite from harzburgite sequence, Hole BA3A. **A.** Section 12Z-2 marked with position of thin section (0–5 cm). **B.** TS (PPL) marked with position of E. **C.** Magnetite (mag) in a vein (RL). **D.** Section 23Z-4 marked with position of TS (0–5 cm). **E.** TS (PPL) marked with position of F. **F.** Chromite intergrowth with clinopyroxene (cpx) and magnetite replacing chromite (chr) (RL).

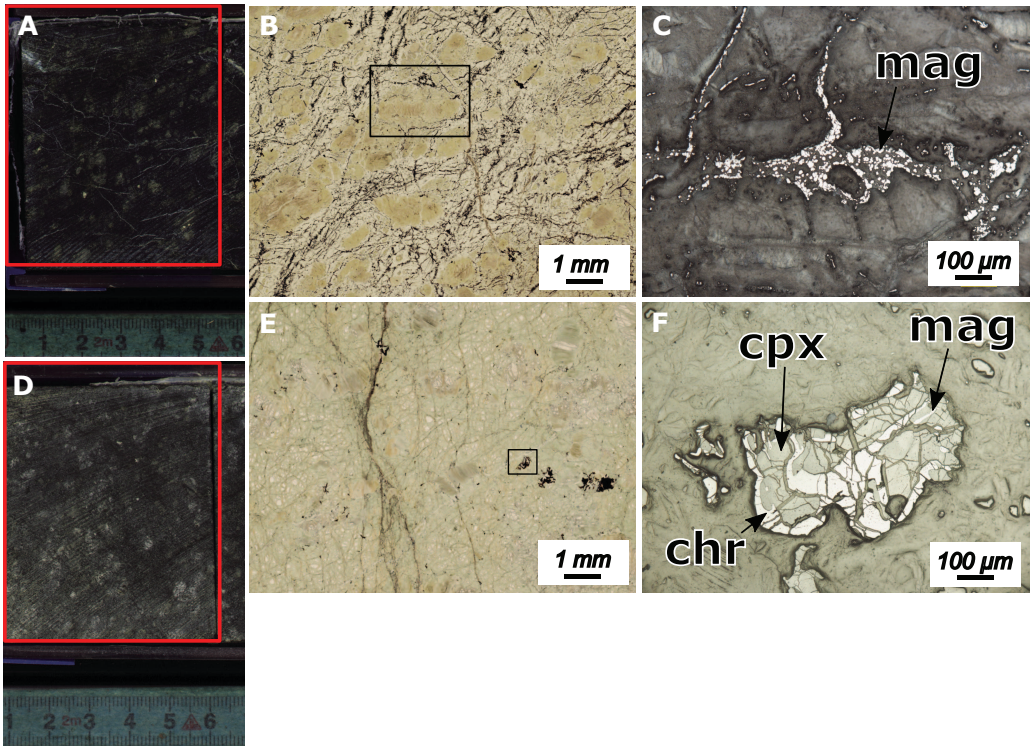

Figure F11. Harzburgite from harzburgite sequence, Hole BA3A. **A.** Section 99Z-4 marked with position of thin section (24–29 cm). **B.** TS (PPL) marked with the position of C. **C.** Group of various sulfides (RL). Chalcopyrite = pale yellow, cuprite = blue, bornite = dark orange, native copper = bright orange. **D.** XRD result from background, indicating serpentine, brucite, clinopyroxene, and orthopyroxene.

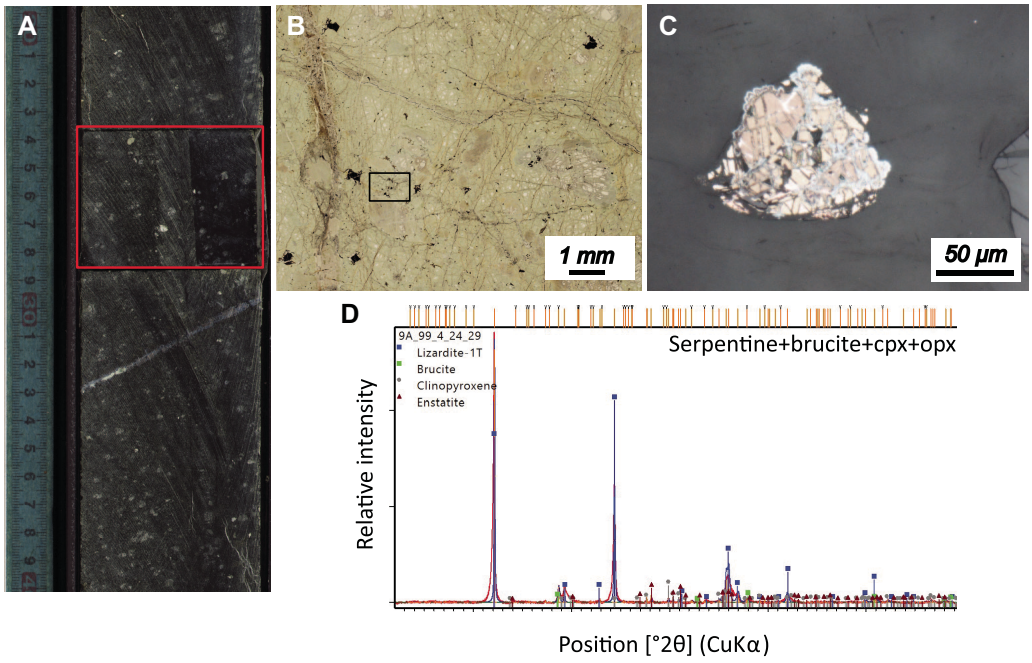

Figure F12. Typical alteration of harzburgite in harzburgite sequence, Hole BA3A. **A.** Highly altered and serpentinized harzburgite in a fracture zone (88Z-2, 31–70 cm). **B.** Oxidized harzburgite toward the top of the hole (31Z-1, 59–83 cm; 70 m). **C.** Harzburgite locally oxidized around a vein toward the bottom of the hole (86Z-3, 30–57 cm; 220 m).

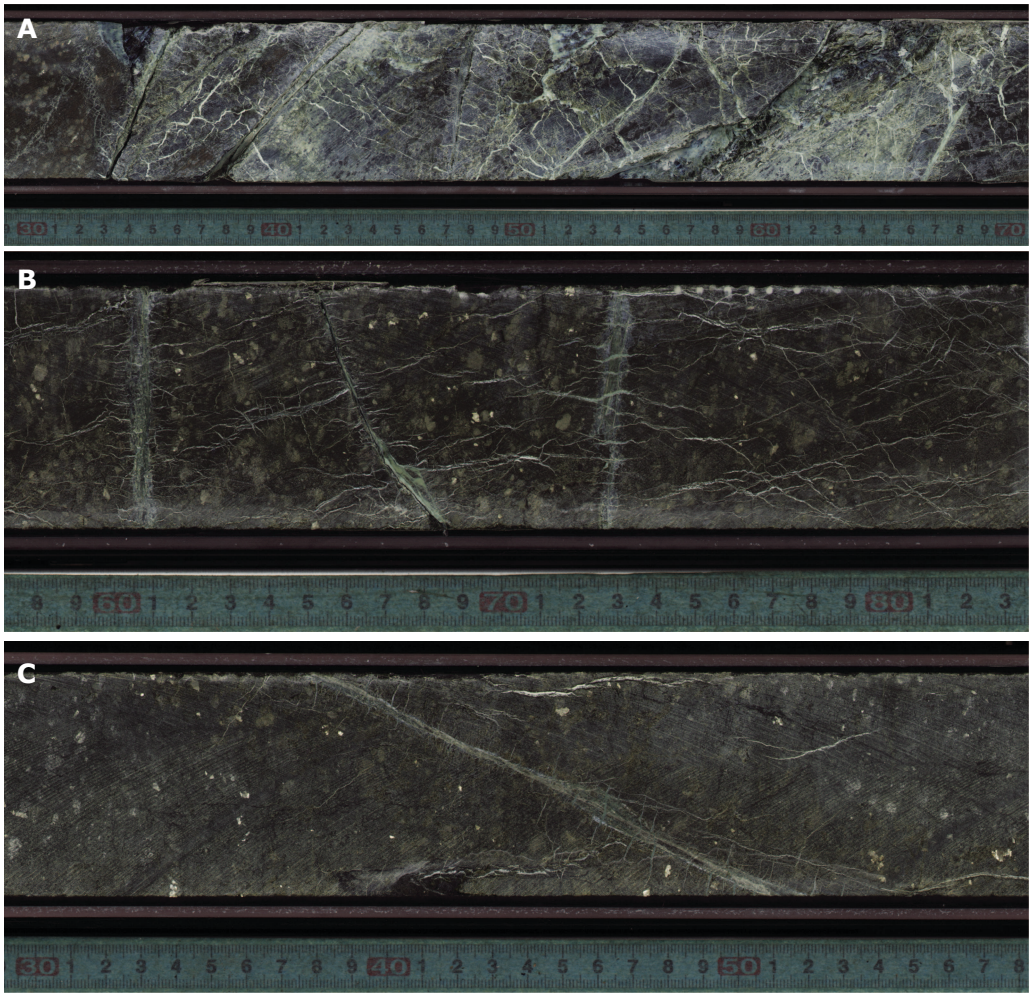

Figure F13. Harzburgite from harzburgite sequence, Hole BA3A. **A.** Section 34Z-1 marked with position of thin section (6–11 cm). **B.** TS (PPL) marked with the positions of D and E. **C.** XRD result from background, indicating serpentine and clinopyroxene (cpx). **D, E.** Overview of highly oxidized harzburgite without any fresh olivine (ol) or orthopyroxene (opx) relics; only clinopyroxene is preserved (D: PPL, E: XPL).

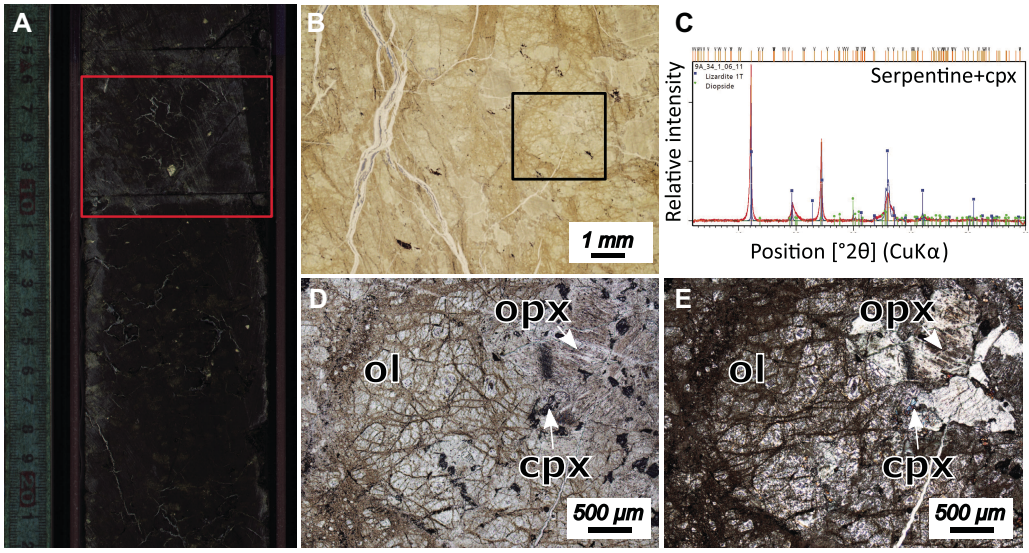

Figure F14. Depth profile of core length affected by oxidation per 10 m, Hole BA3A.

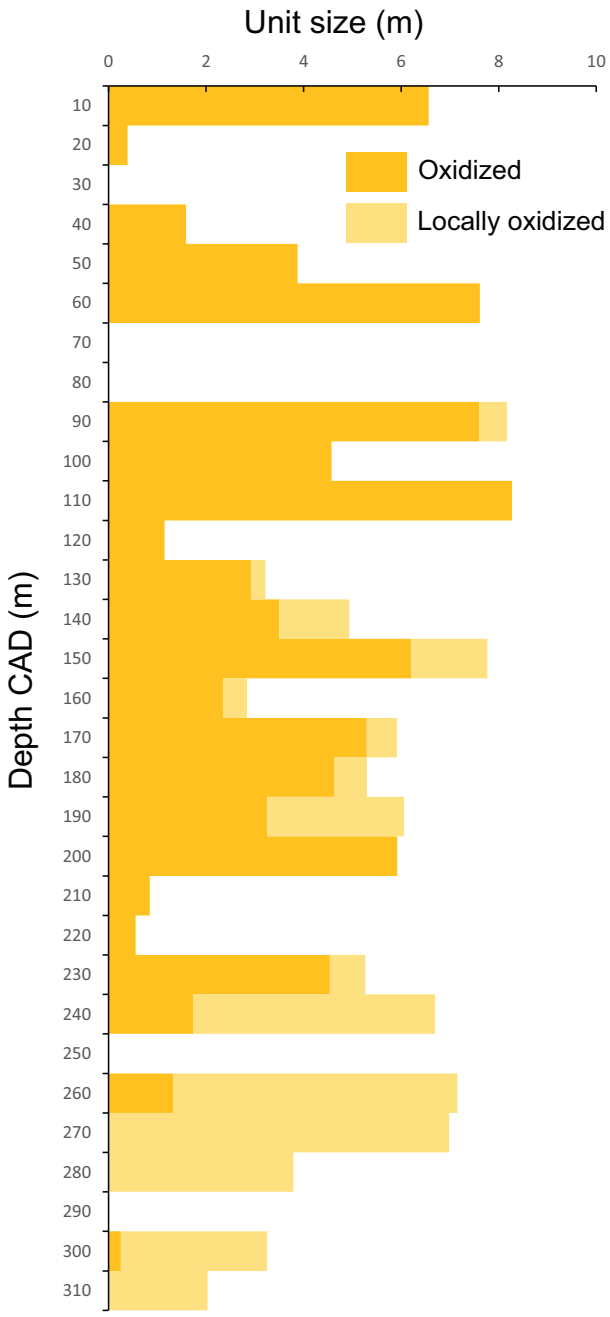

Figure F15. Typical dunite occurrences in harzburgite sequence, Hole BA3A. **A.** Dunite patch in harzburgite (72Z-2, 3–5 cm). **B.** Dunitic bands between orthopyroxene-rich layers (78Z-4).

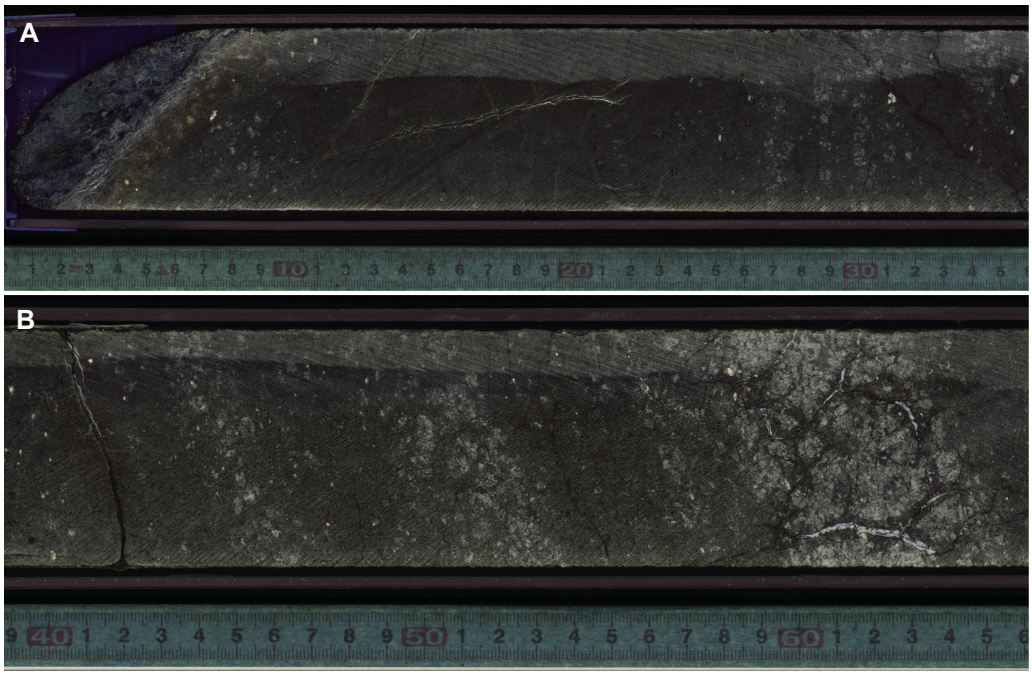

Figure F16. Dunite from harzburgite sequence, Hole BA3A. **A.** Section 13Z-2 marked with the positions of the thin sections (22–25 cm; 29–32 cm) in the dunitic zone. **B.** Completely serpentinized olivine with typical mesh texture. **C.** TS (PPL) marked with the positions of D and E. **D.** Magnetite (mag) replacing chromite (chr) (RL). **E.** Altered and eroded olivine with euhedral crystals growing into the gap (PPL).

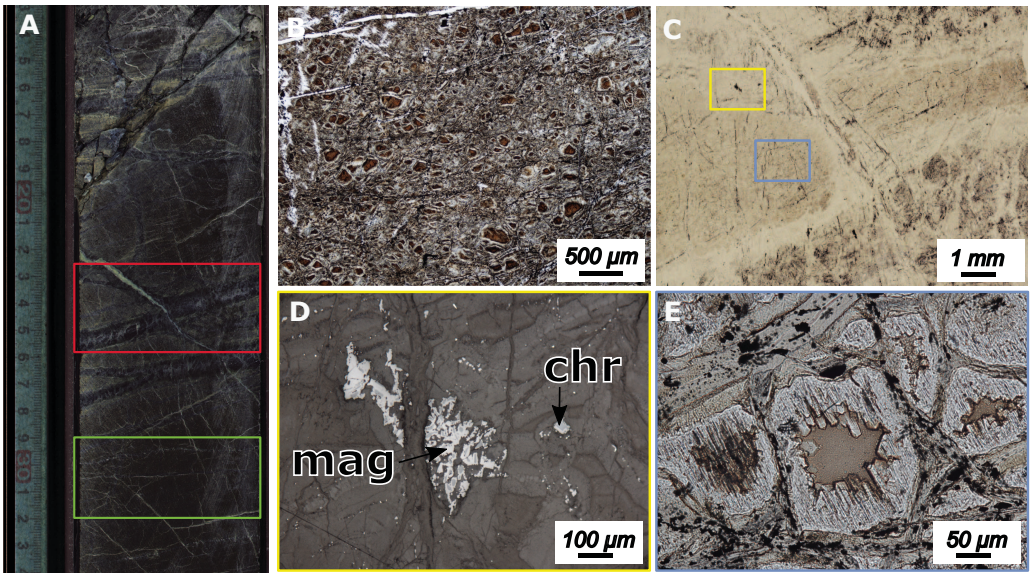

Figure F17. Dunite from harzburgite sequence, Hole BA3A. **A.** Section 75Z-1 marked with the position of the thin section (42–44 cm). **B.** TS (PPL) marked with the positions of D and E. **C.** XRD result from background, indicating serpentine and clinopyroxene. **D, E.** "Fingerprint" olivine close to serpentine vein network (D: PPL, E: XPL).

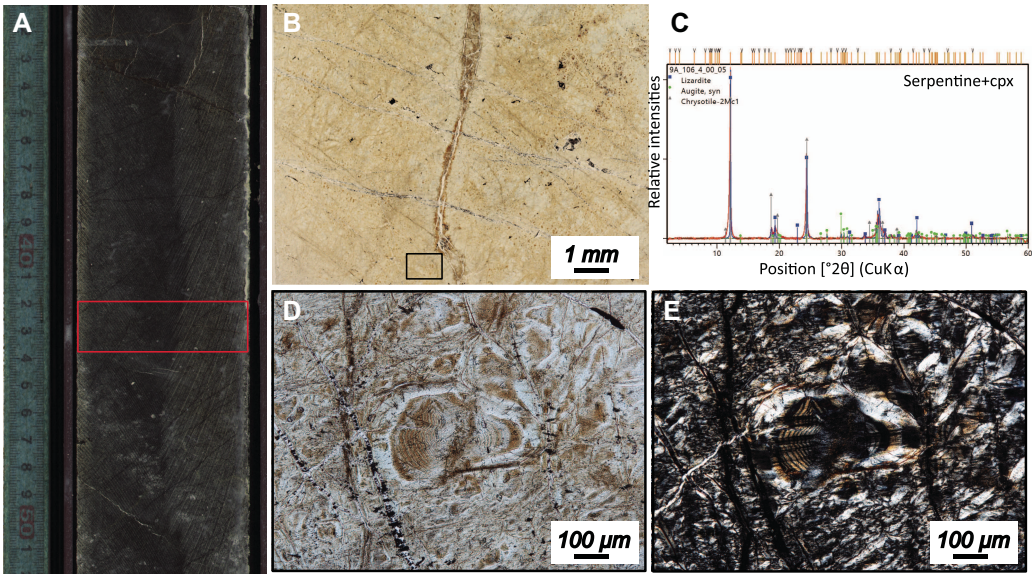

Figure F18. Variation of the (**A**) number and (**B**) composition of dikes with depth, Hole BA3A.

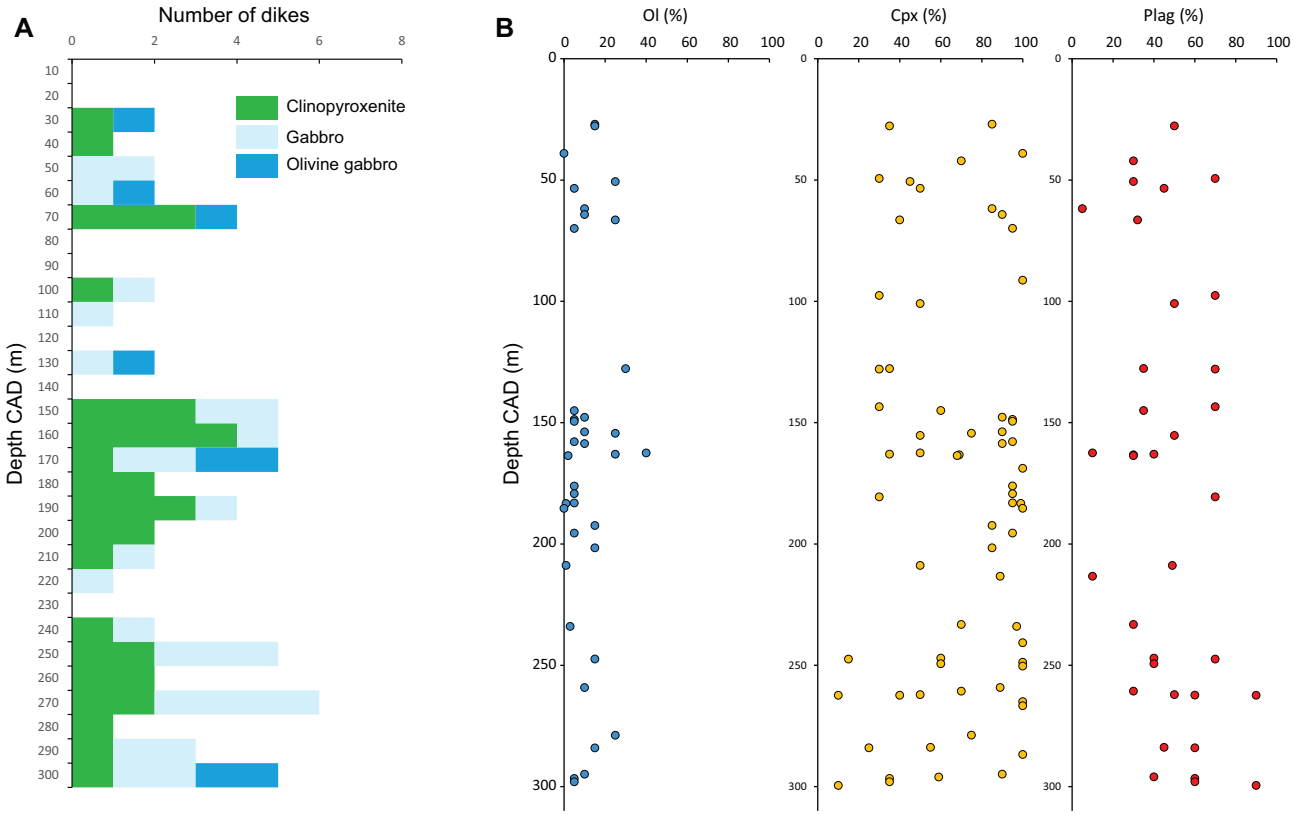

Figure F19. Examples of dikes in harzburgite sequence, Hole BA3A. **A.** Gabbroic dike (95Z-2, 44–60 cm). **B.** Clinopyroxenitic dike (80Z-2, 12–30 cm). **C.** Olivine-rich clinopyroxenitic dike (99Z-2, 64–81 cm).

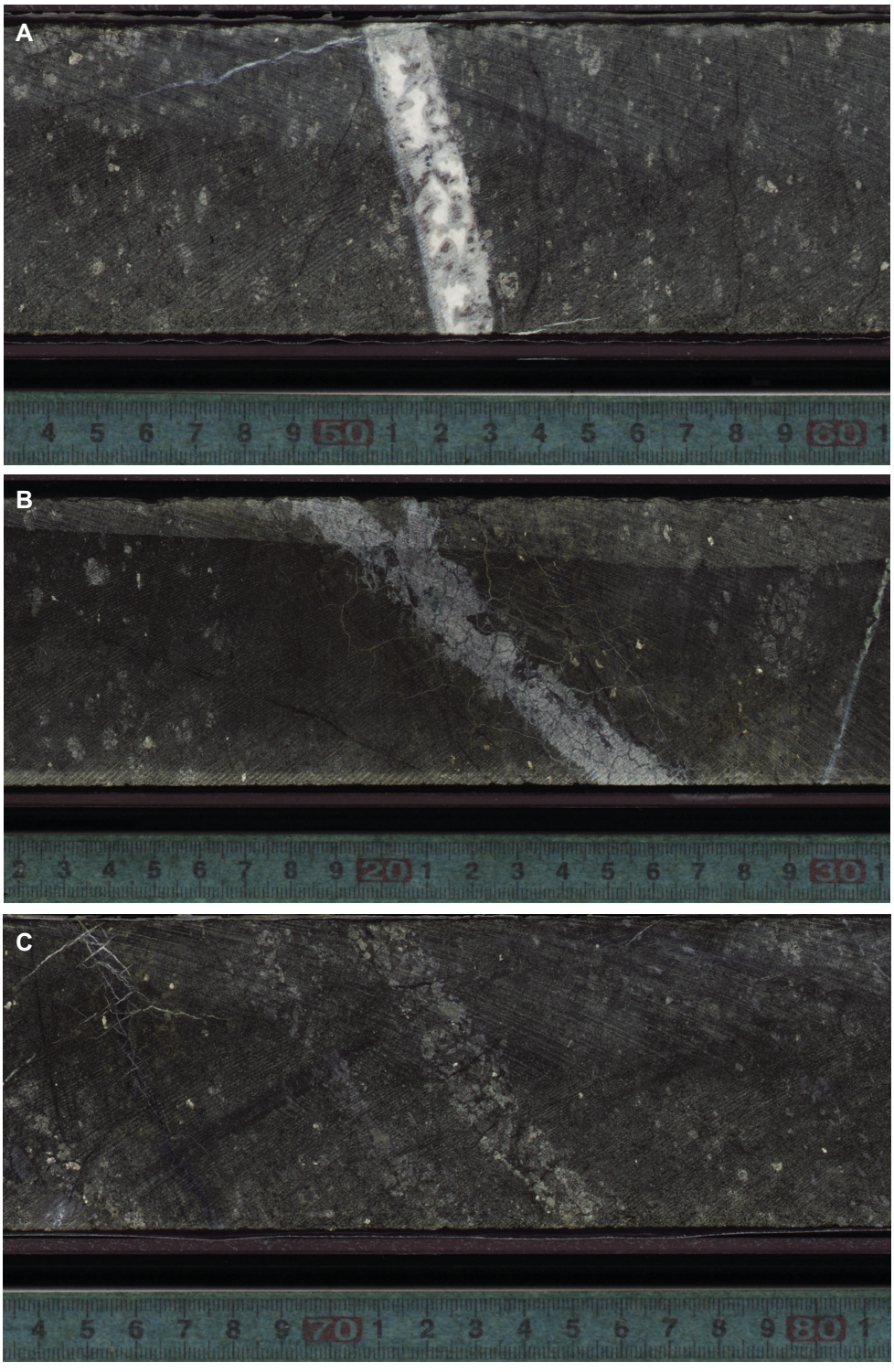

Figure F20. Examples of alteration in dikes of harzburgite sequence, Hole BA3A. **A.** Two highly altered dikes with uncertain primary mineralogy (91Z-1, 25–47 cm). **B.** Rodingitized gabbro (64Z-5, 16–33 cm). **C.** Altered red clinopyroxenite (97Z-1, 25–32 cm).

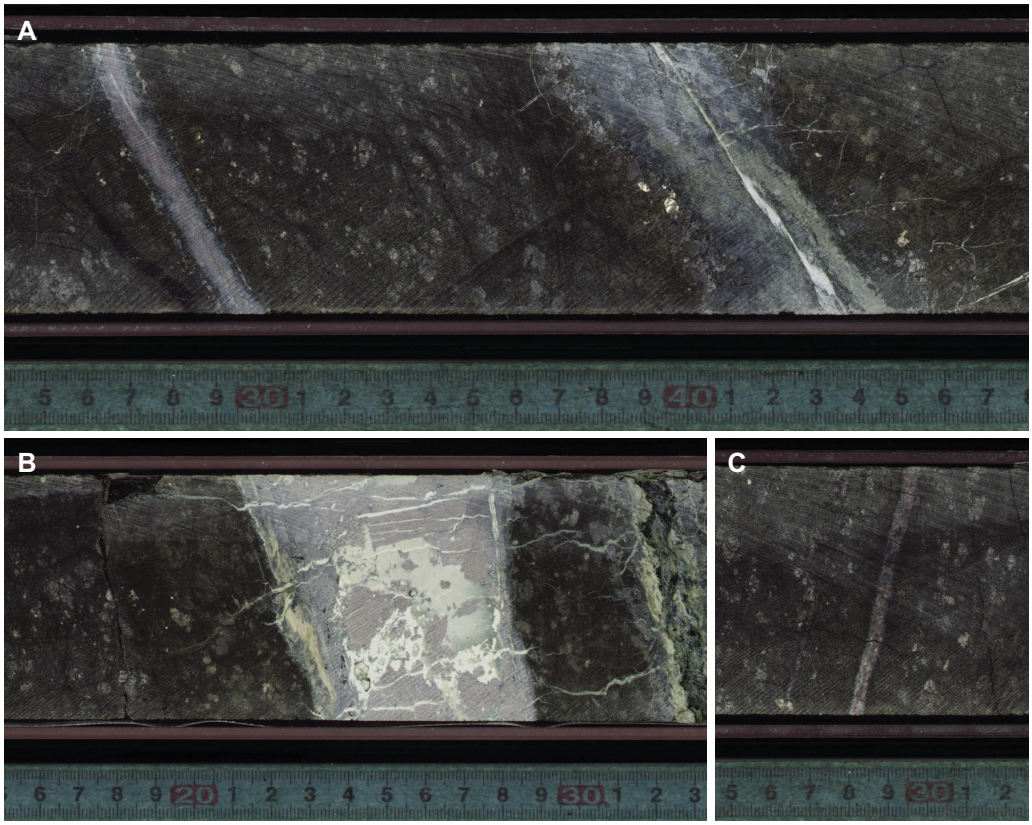

Figure F21. Gabbroic dikes from harzburgite sequence, Hole BA3A. **A.** Section 30Z-1 marked with the position of the thin section in red (49–52 cm) and of the XRD analysis in blue. **B.** TS (PPL) marked with the positions of C–E. **C.** Pyrrhotite in the gabbroic dike. **D, E.** Overview of a typical microgabbro with plagioclase replaced by hydrogrossular (hgr), olivine replaced by serpentine (serp), and clinopyroxene replaced by tremolite (tr) (D: PPL, E: XPL). **F.** XRD result from investigated sulfide phase.

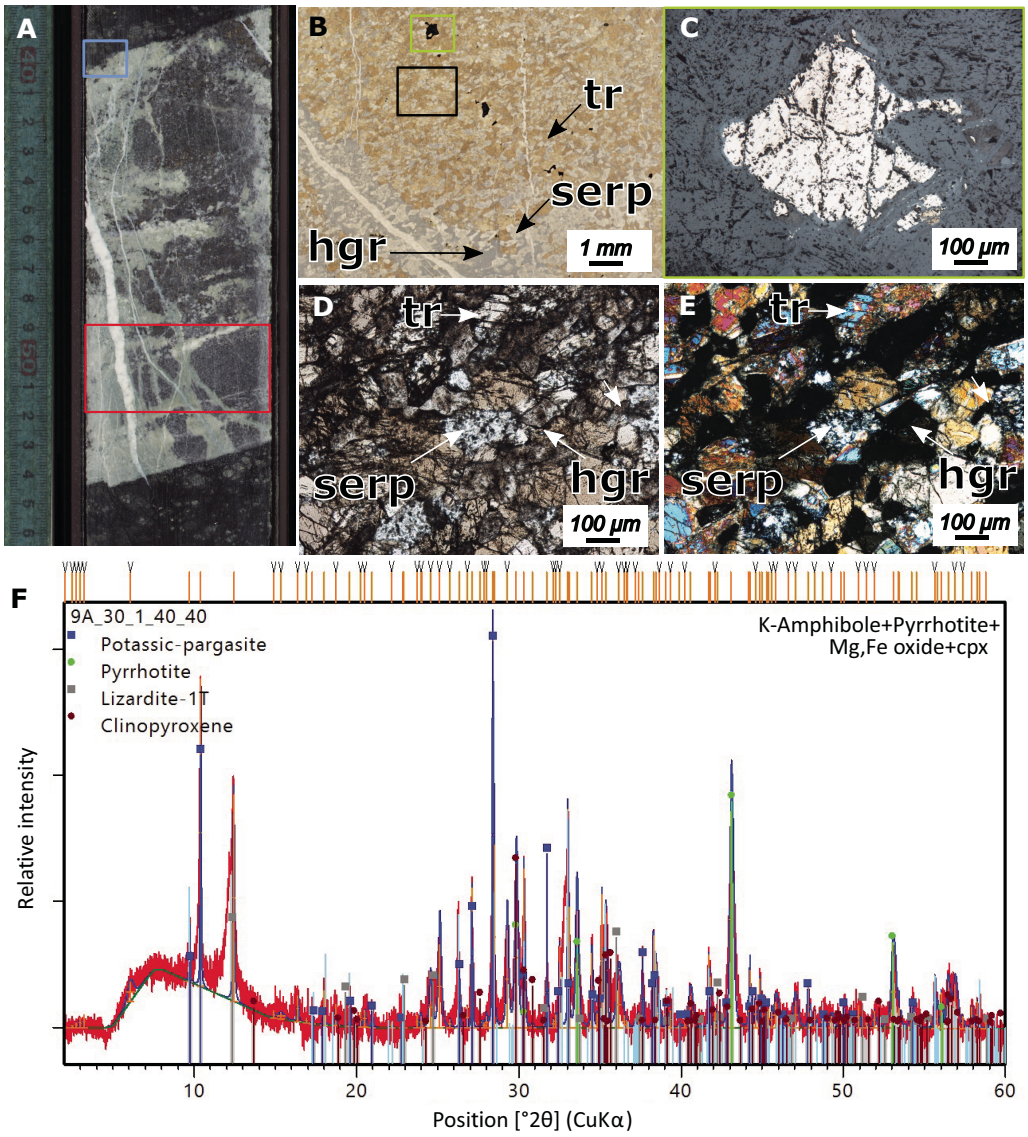

Figure F22. Gabbroic dikes from harzburgite sequence, Hole BA3A. **A.** Section 64Z-5 marked with position of thin section (22–26 cm). **B.** TS (PPL) marked with positions of C–I. **C.** Overview of altered gabbroic dike with plagioclase replaced by hydrogrossular (hgr), chromite replaced by magnetite (mag), and potentially orthopyroxene replaced by chlorite (chl) (RL). **D.** Close-up of plagioclase replaced by hydrogrossular (RL). **E.** Chlorite with prismatic clinopyroxene (cpx) crystals (PPL). **F, G.** Chlorite, serpentine (serp), and hydrogrossular in contact between gabbroic dike and harzburgite (F: PPL, G: RL). **H, I.** Chlorite at the contact between gabbroic dike and harzburgite (H: PPL, I: XPL).

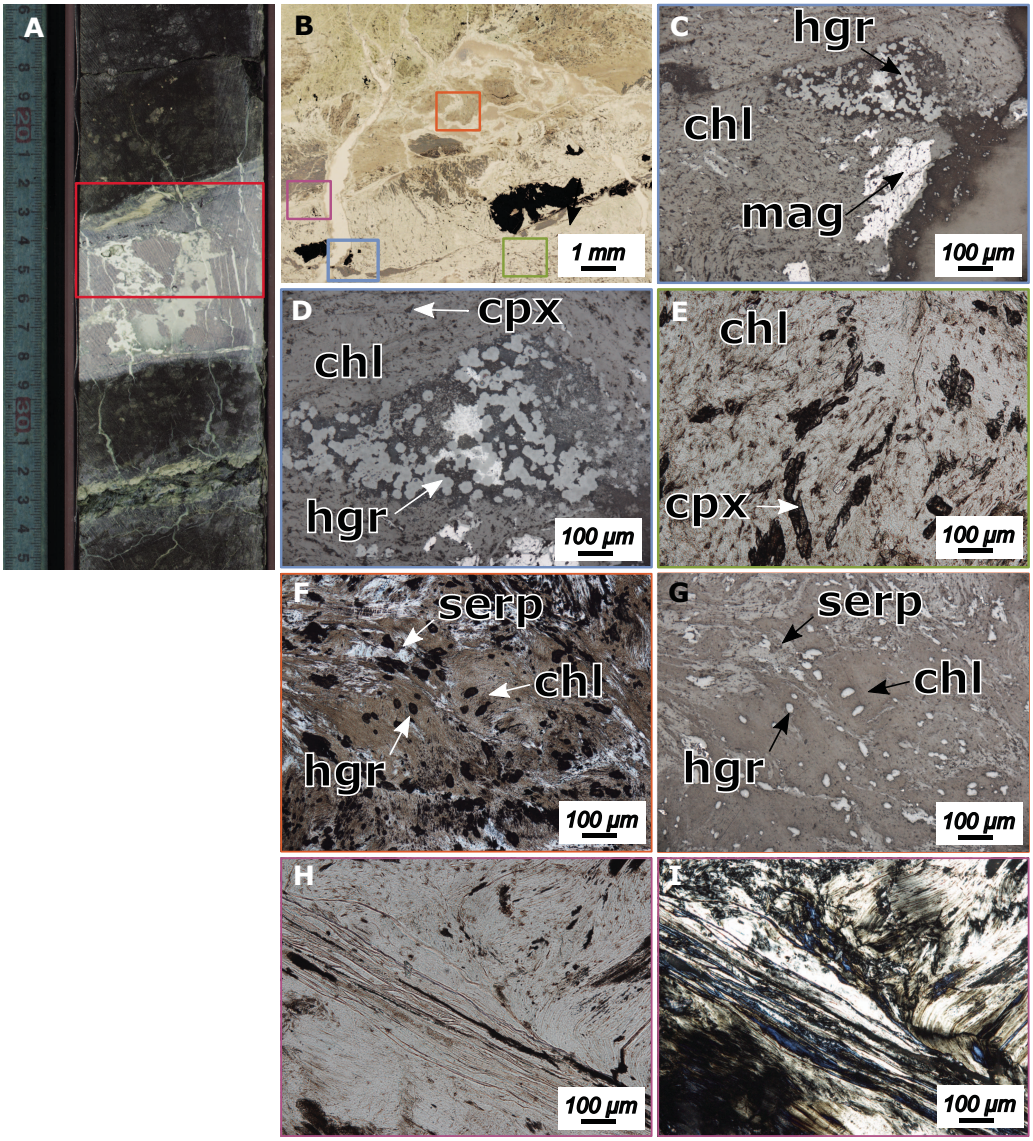

Figure F23. Gabbroic dikes from harzburgite sequence, Hole BA3A. **A.** Section 95Z-2 marked with position of thin section (50–53 cm). **B.** TS (PPL) marked with positions of C–F. **C, D.** Contact between gabbroic dike and harzburgite with chlorite (chl) and talc (TLC) in the contact and orthopyroxene (opx) (C: PPL, D: XPL). tr = tremolite. **E, F.** Contact between gabbroic dike and harzburgite with prehnite (prh) in contact and orthopyroxene next to it (E: PPL, F: XPL).

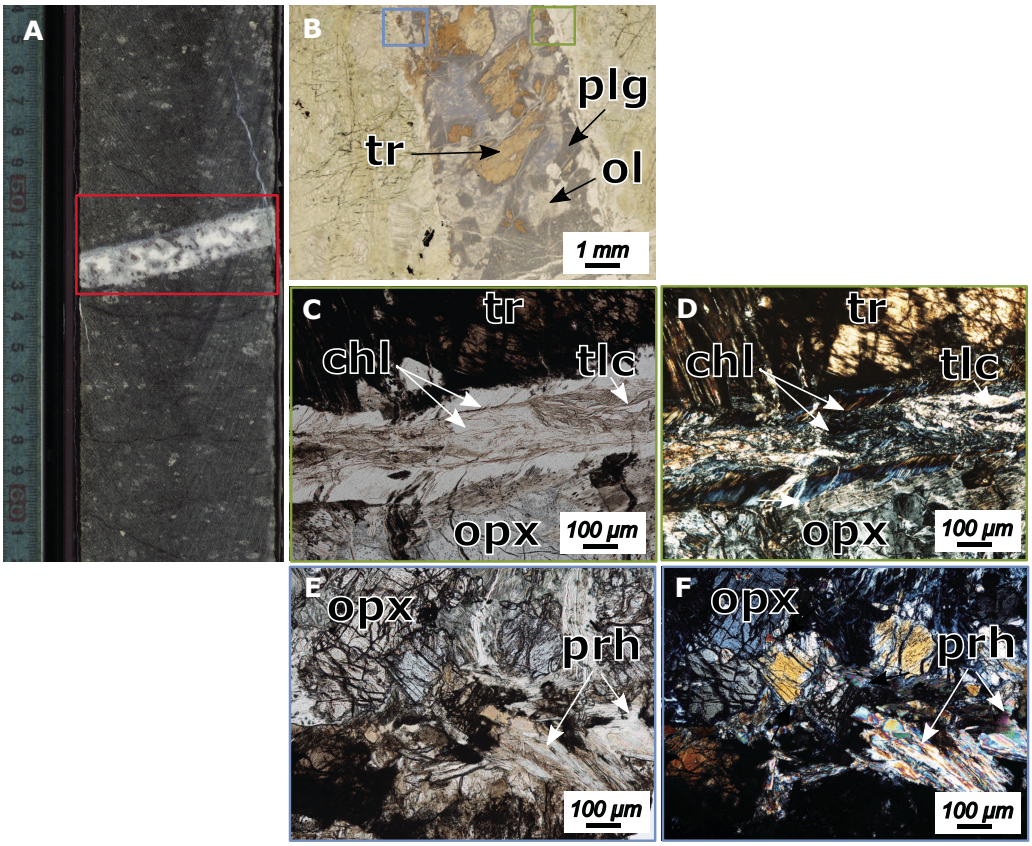

Figure F24. Clinopyroxenitic dikes from harzburgite sequence, Hole BA3A. **A.** XRD result from the background, indicating olivine, amphibole, and serpentine. **B.** Section 52Z-1 marked with position of thin section (66–71 cm). **C.** TS with red clinopyroxenitic dike (PPL). ol = olivine. **D.** A group of various sulfides next to clinopyroxenitic dike. Chalcopyrite = pale yellow, cuprite = blue, bornite = dark orange, native copper = bright orange (RL). **E, F.** Clinopyroxenitic dike replaced by tremolite (tr), orthopyroxene (opx), and serpentine (serp) next to the dike (E: PPL, F: XPL).

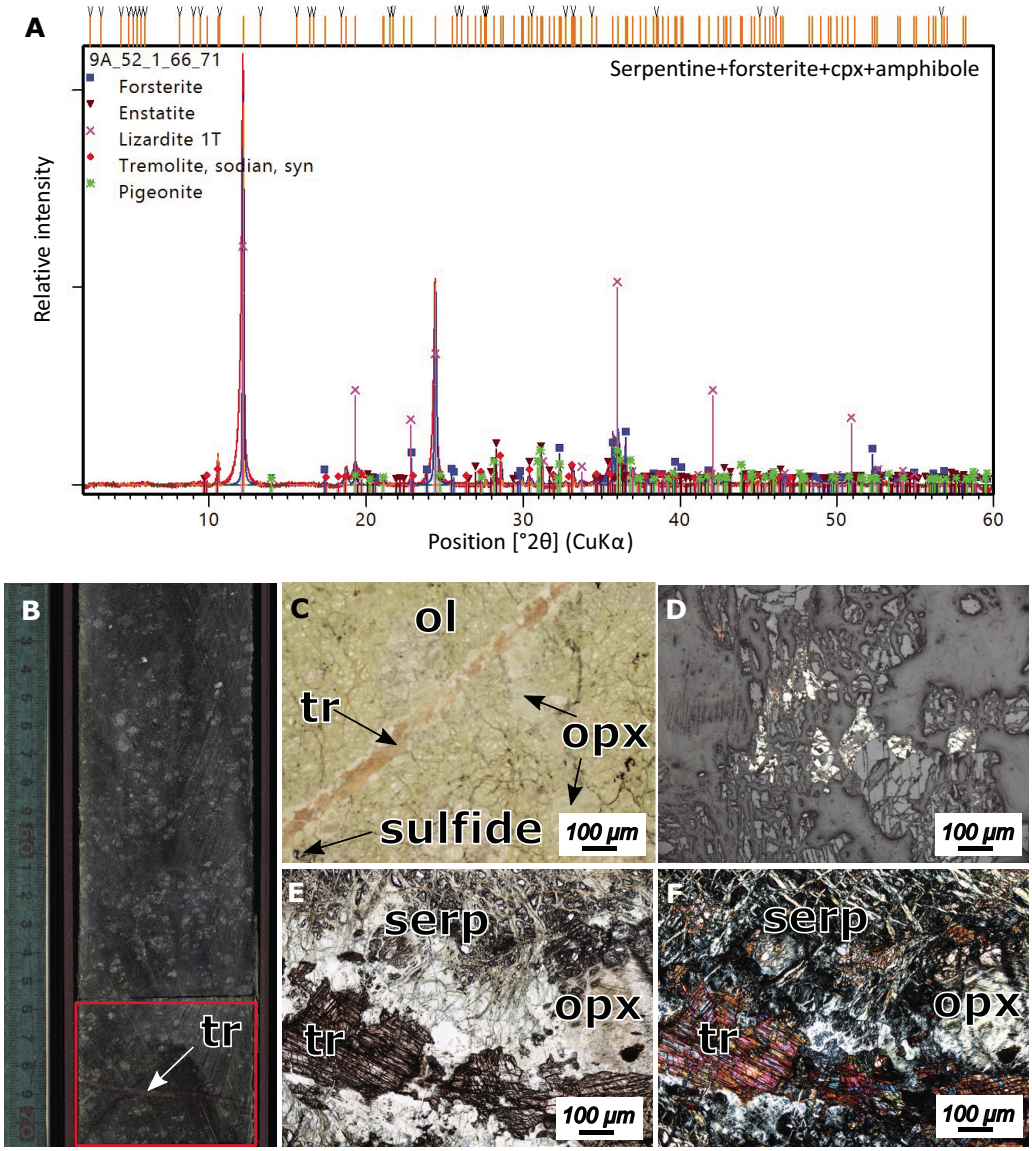

Figure F25. Lithology summary log, Hole BA3A.

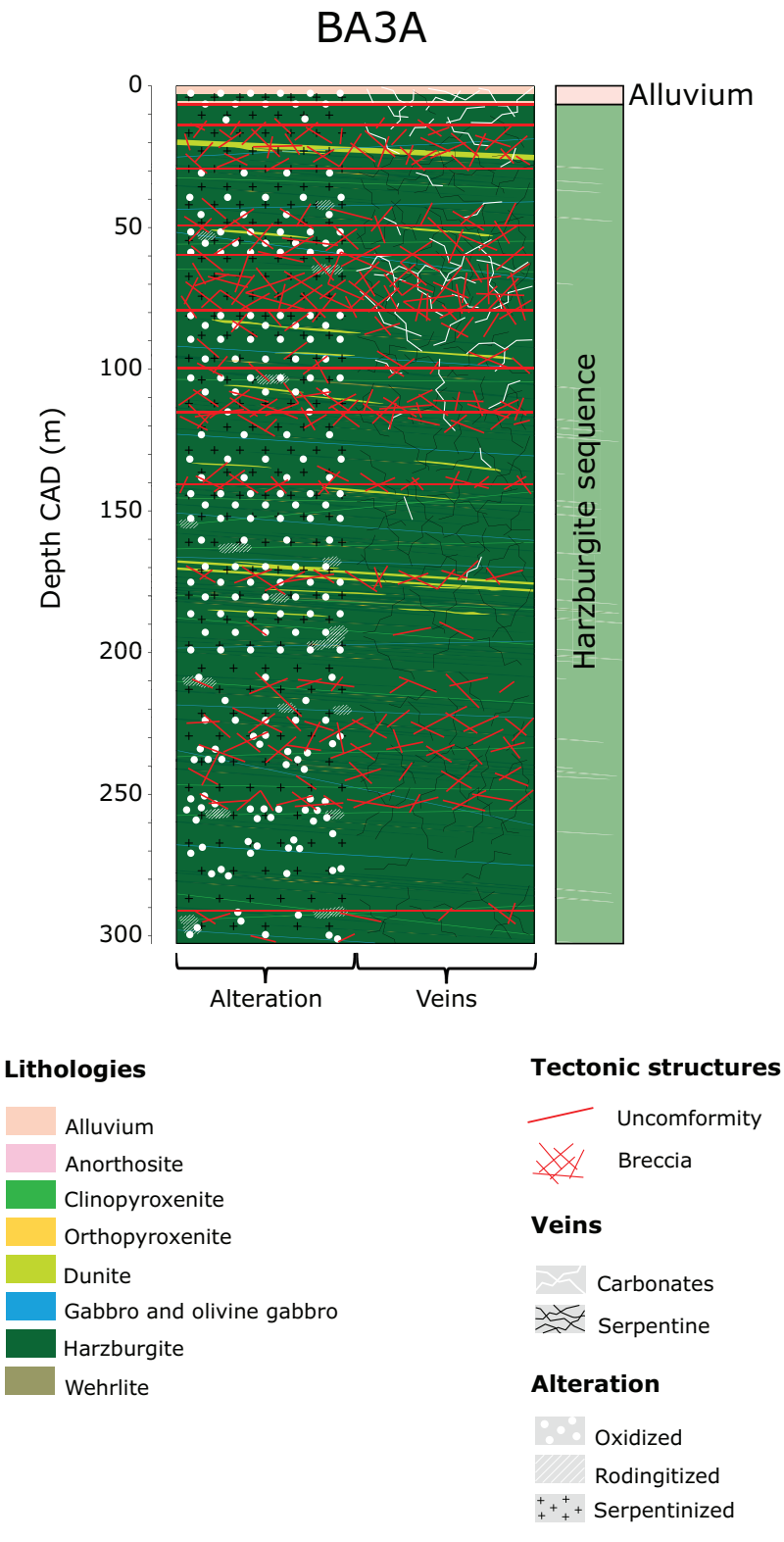

Figure F26. Crosscutting relationships of veins in core from Hole BA3A, compared to the same data for Hole BA1B. Symbols represent some of the most common younger vein types. For example, open symbols represent carbonate-bearing veins. Labeled points correspond to all of the vein types for which a significant number of crosscutting relationships were observed. The horizontal axis indicates the number of instances in which one of the many vein types was observed to cut one of the common types, and the vertical axis represents instances in which one of the common types cuts them. For example, though waxy green serpentine veins generally crosscut all other vein types, in ~10% of their crosscutting relationships, waxy green serpentine veins are cut by white (vein type Sf, 9 observations), dark (Sa + Sc + Sd, 4), and composite (Se, 2) serpentine veins.

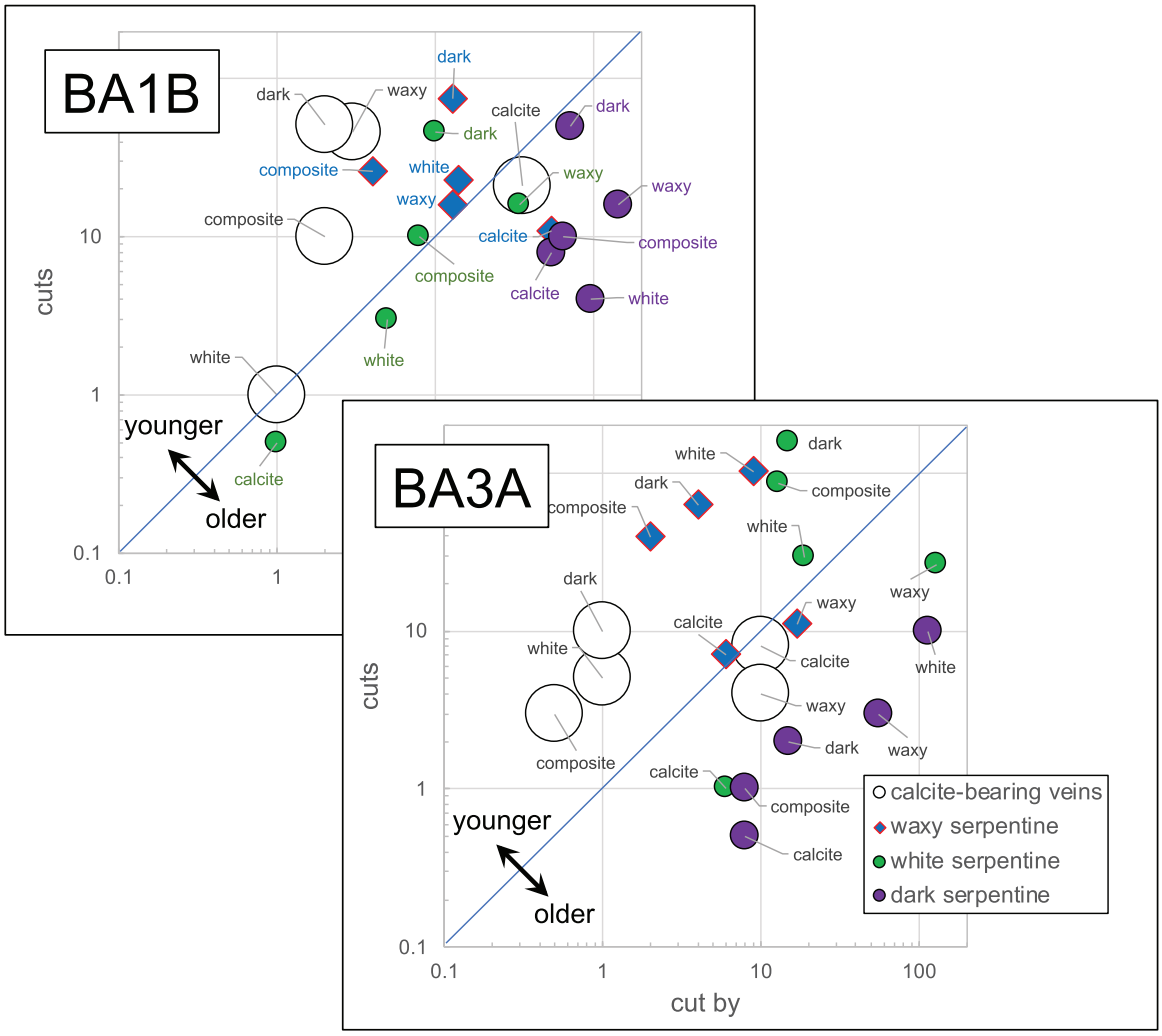

Figure F27. Variation of area percent veins observed in Hole BA3A, excluding patchy alteration of deformed magmatic blocks (Sg), compared to similar data for Hole BA1B. The red rectangle outlines the region of 5%–10% veins on this diagram, to make it easy to compare vein abundance in the top vs. the bottom of each hole and to compare vein abundance in one hole vs. the other. Unlike Hole BA1B, area proportions of specific veins, vein sets, and vein networks, within the depth intervals where they were observed, were estimated directly during visual description of core from Hole BA3A. For this reason, comparison of estimates for Hole BA1B (this figure, and Fig. F28) should be viewed as semiquantitative.

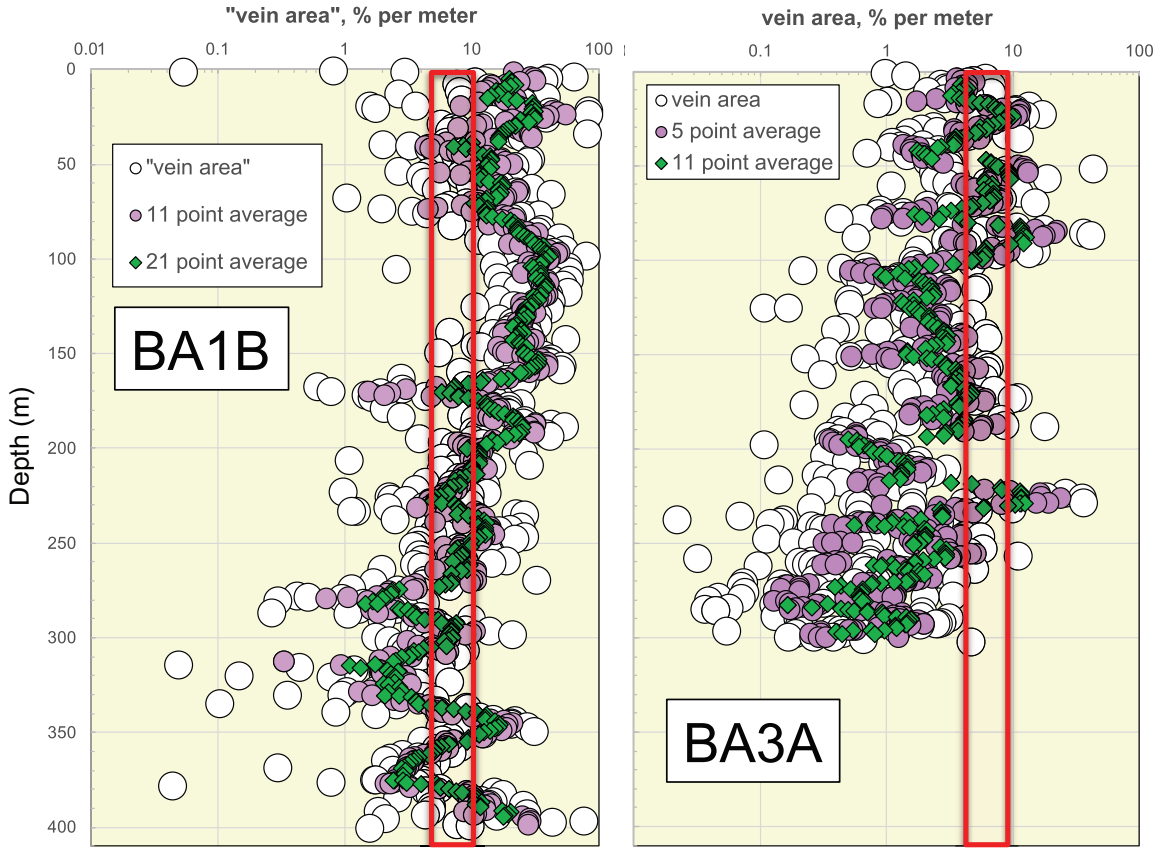

Figure F28. 25 m running average of the number of observations of specific vein types as a function of depth in Hole BA3A, compared to the same data for Hole BA1B.

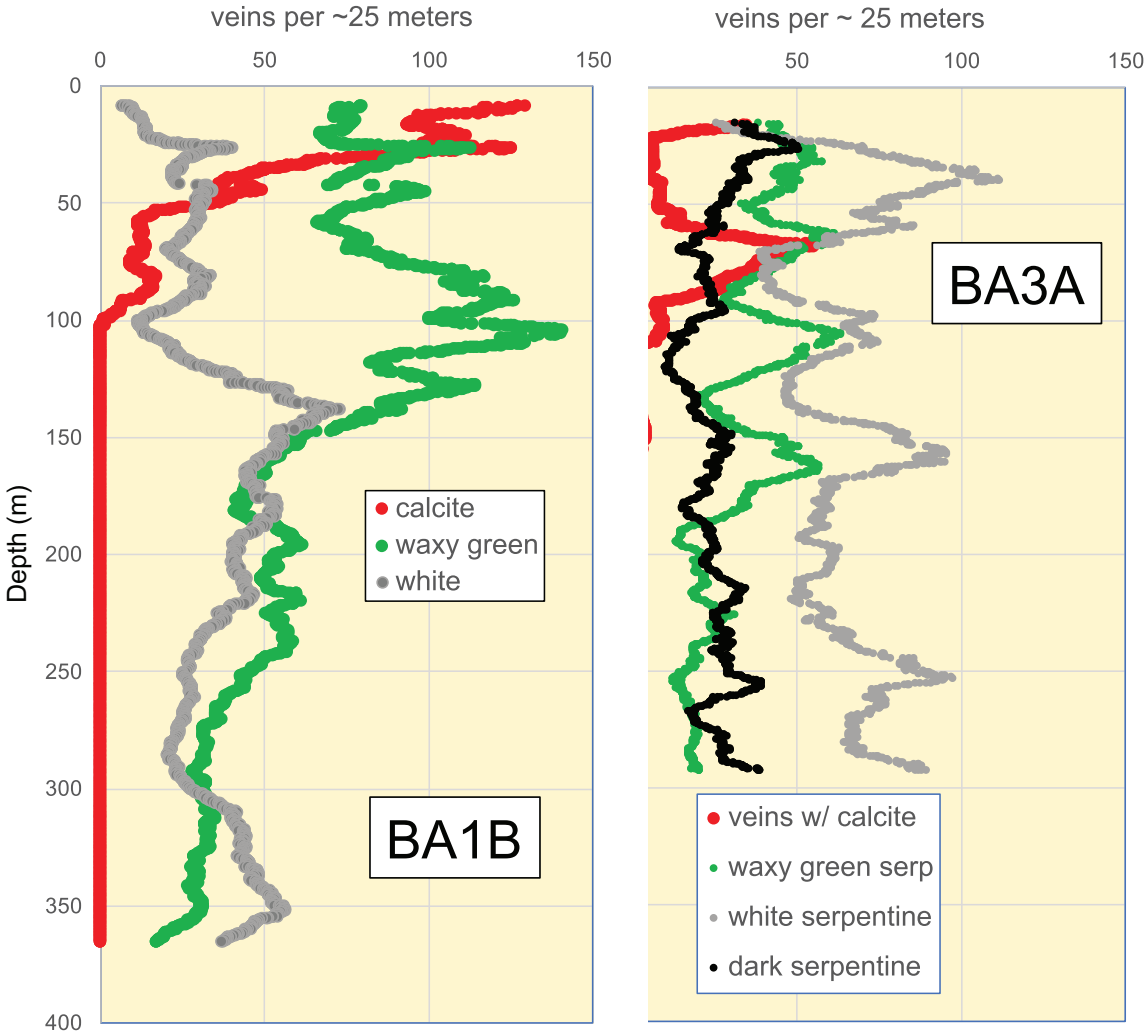

Figure F29. Observed vein types as a function of depth in Hole BA3A, compared to the same data for Hole BA1B.

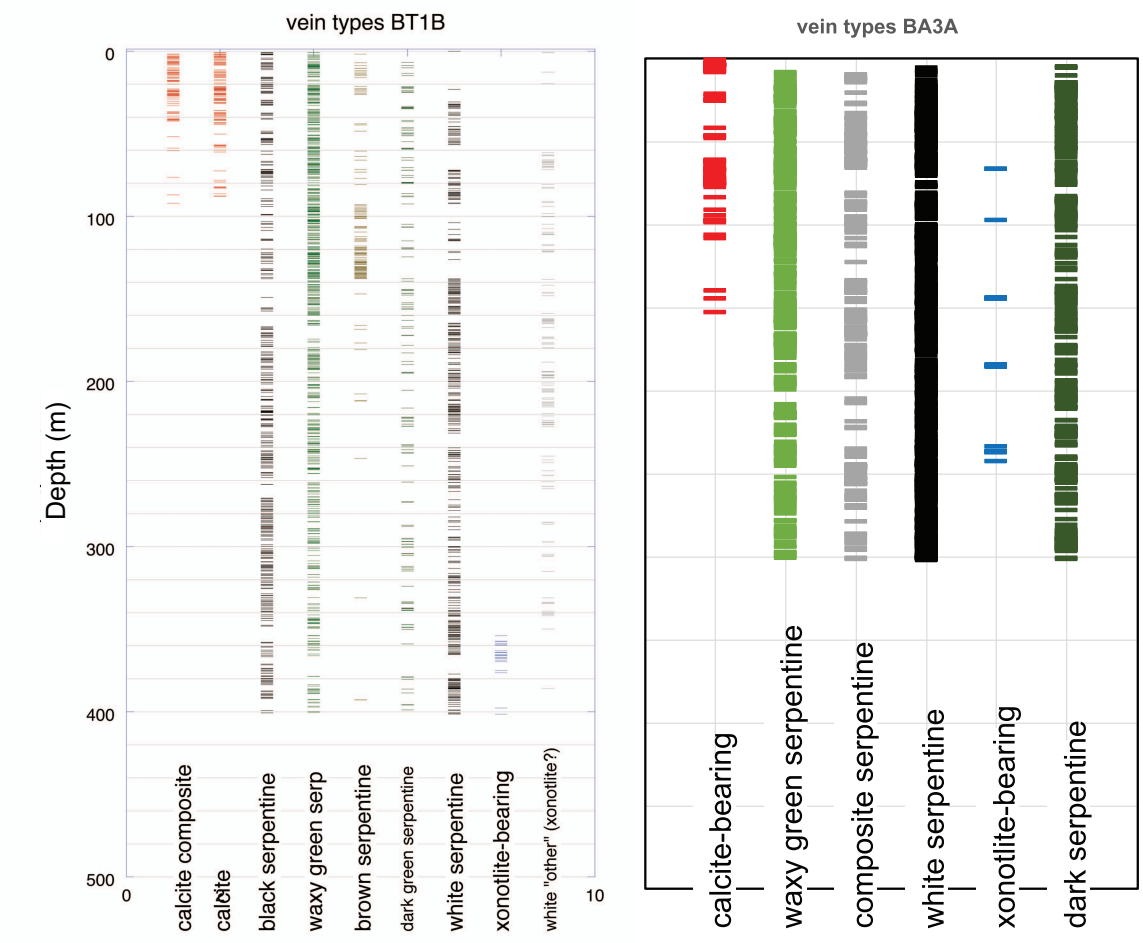

Figure F30. Vein types described in core, Hole BA3A. **A.** Type Ca1 (7.9 m). **B.** Type Ca3 (arrows; 75.3 m). **C.** Type Cb (3.3–3.4 m). **D.** Type Sa (240.8–241.0 m). **E.** Type Sb (78.6 m). (Continued on next page.)

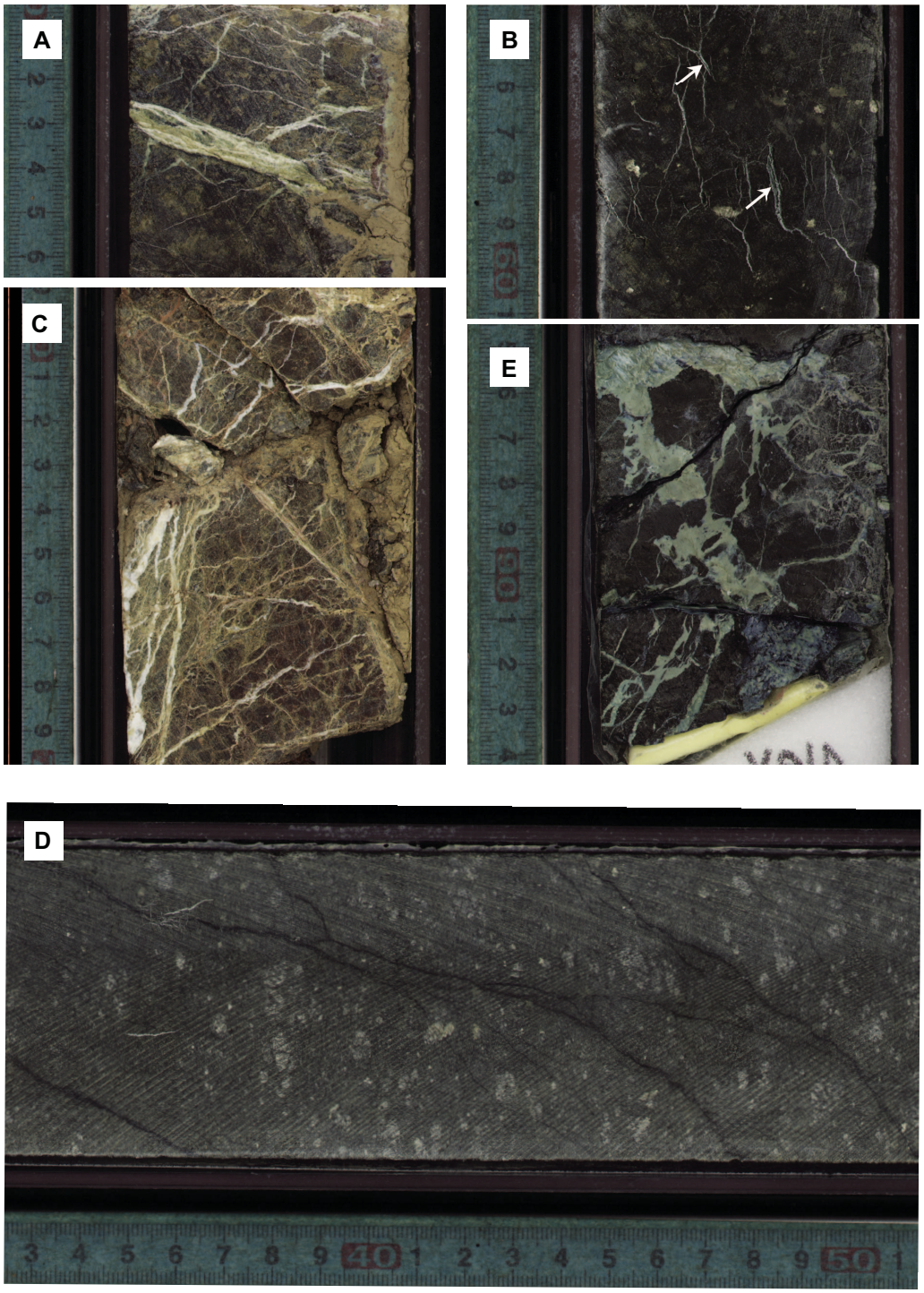

Figure F30 (continued). **F.** Type Sc (256.1–256.2 m). **G.** Type Sd (101.2–101.3 m). **H.** Composite of light green and dark green serpentine, type Se (49.4 m). **I.** Type Sf (59.2–59.3 m). **J.** Type Sg (105.6–105.8 m). **K.** White type X vein cutting a magmatic dike (97.6–97.7 m).

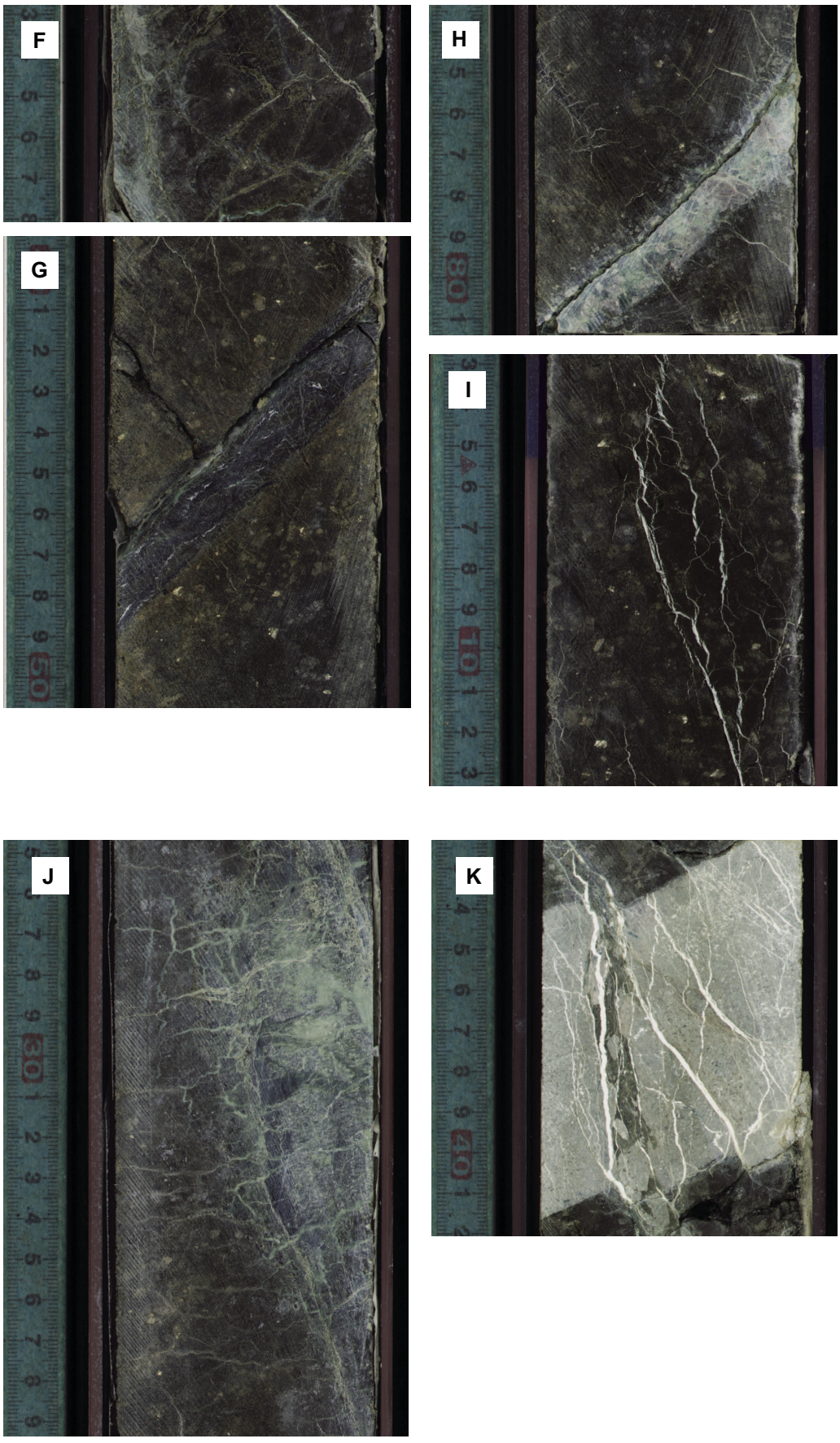

Figure F31. Typical veins in serpentinized ultramafic lithologies, Hole BA3A. **A, B.** Subparallel serpentine veins in the mesh part of the network form in close relation to the prevalent mesh texture. **C, D.** Serpentine vein containing intraveinous magnetite. **E.** Crosscutting "Frankenstein" vein. **F.** Frankenstein vein with brown halo. Mesh rims and mesh centers show orange-brown discoloration.

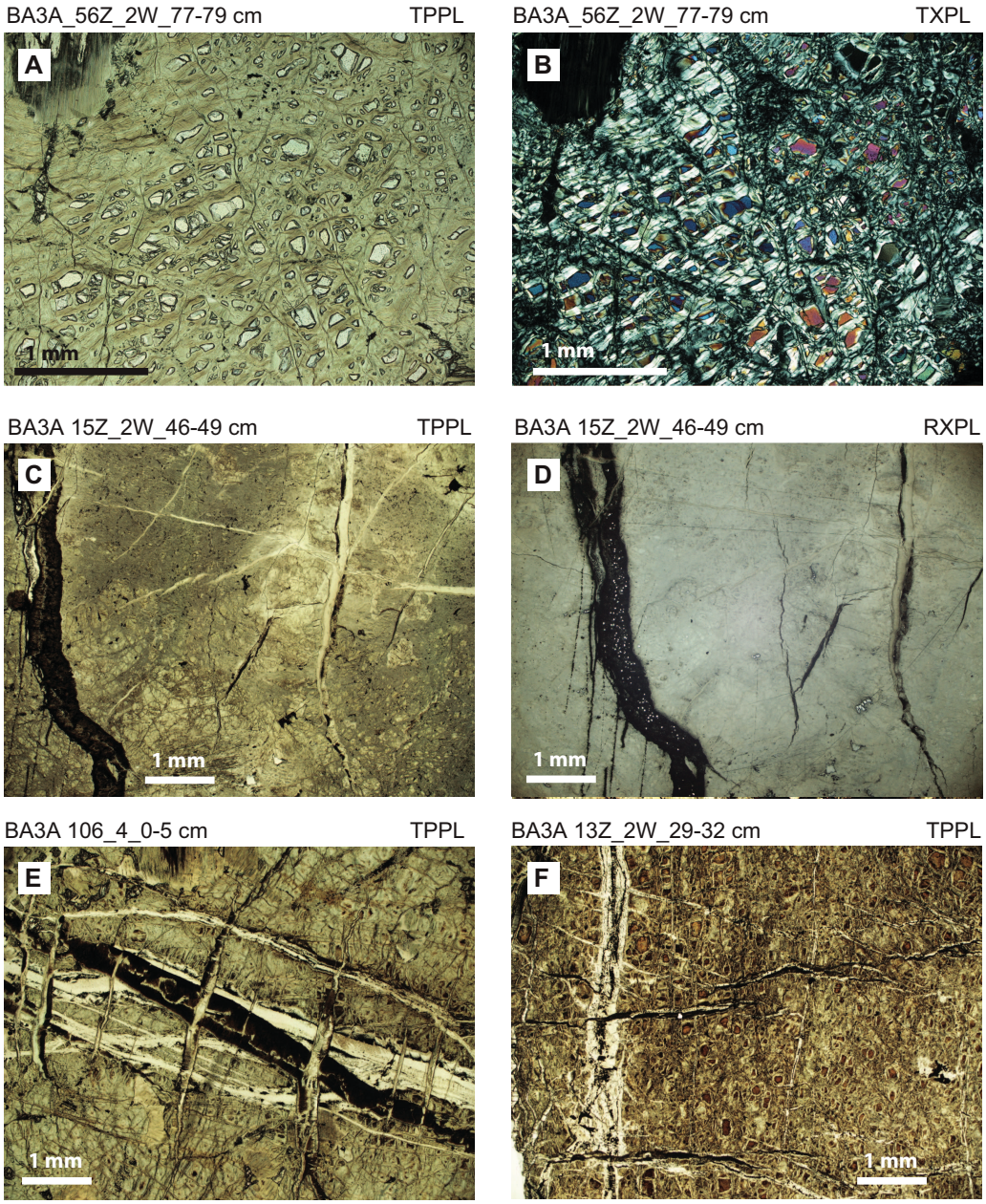

Figure F32. Microscopy (RL) of opaque minerals, Hole BA3A. **A.** Large heazlewoodite crystal in matrix of serpentinized harzburgite. **B.** Native copper rimmed by magnetite. **C.** Native copper-pentlandite-awaruite assemblage intergrown with magnetite. **D.** Dispersed magnetite grains in serpentine vein. **E.** "Ferritchromitization" along the rim of a chromite crystal.

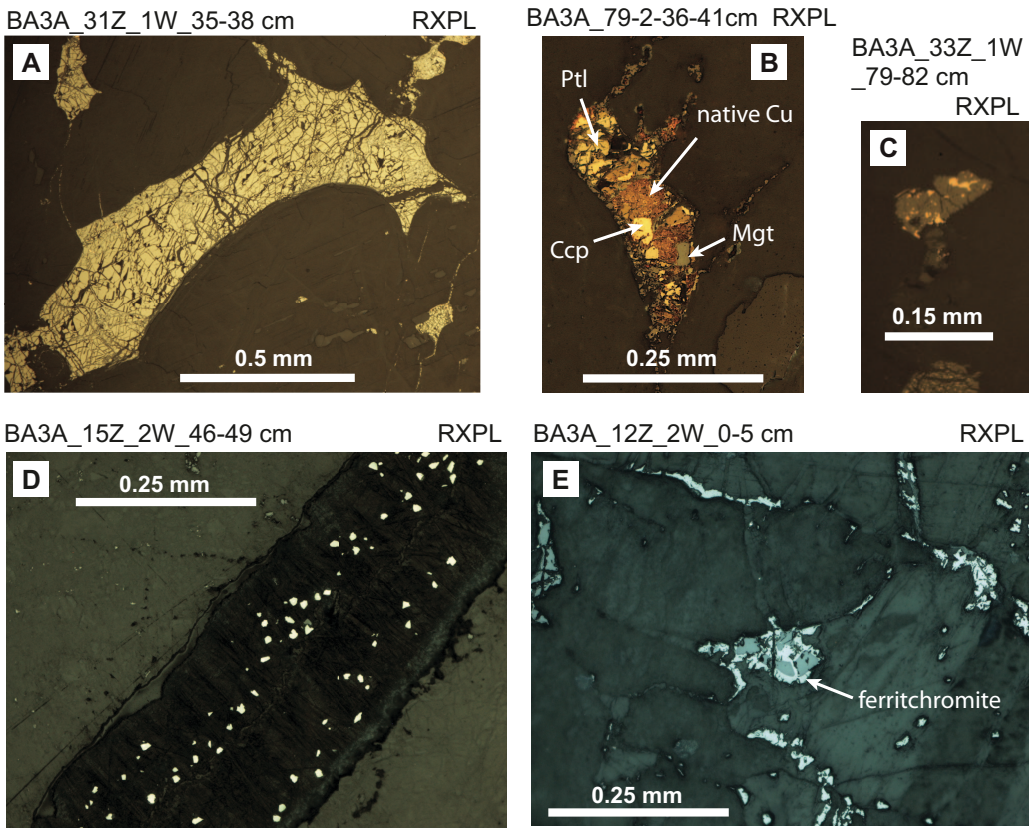

Figure F33. pH and temperature of water in Hole BA3A in March 2018, measured during geophysical logging (Pezard et al., pers. comm., 2018).

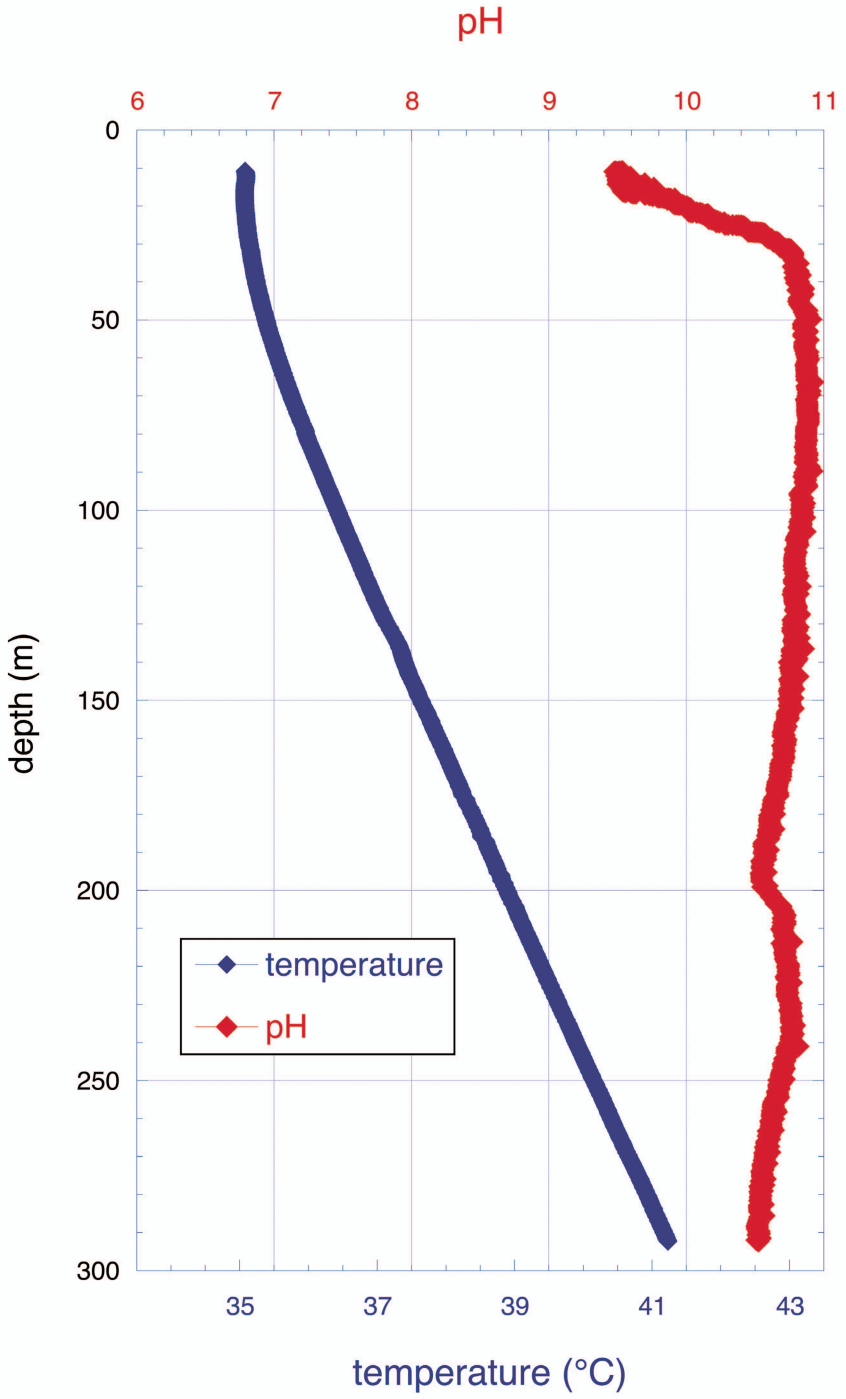

Figure F34. Dip angle and crystal-plastic fabric intensity of the foliation within dunites and harzburgites. **A.** Dip angle of pyroxene foliation in dunite and harzburgite and harzburgite foliation. **B.** Crystal-plastic intensity: 0 = undeformed-protogranular, 1 = weakly foliated (porphyroclastic), 2 = moderately foliated (porphyroclastic), 3 = protomylonite, 4 = mylonite, 5 = ultramylonite, 6 = pseudotachylite. **C.** Rose diagram for dip angle of pyroxene. Most dip angles of pyroxenes are ~30°.

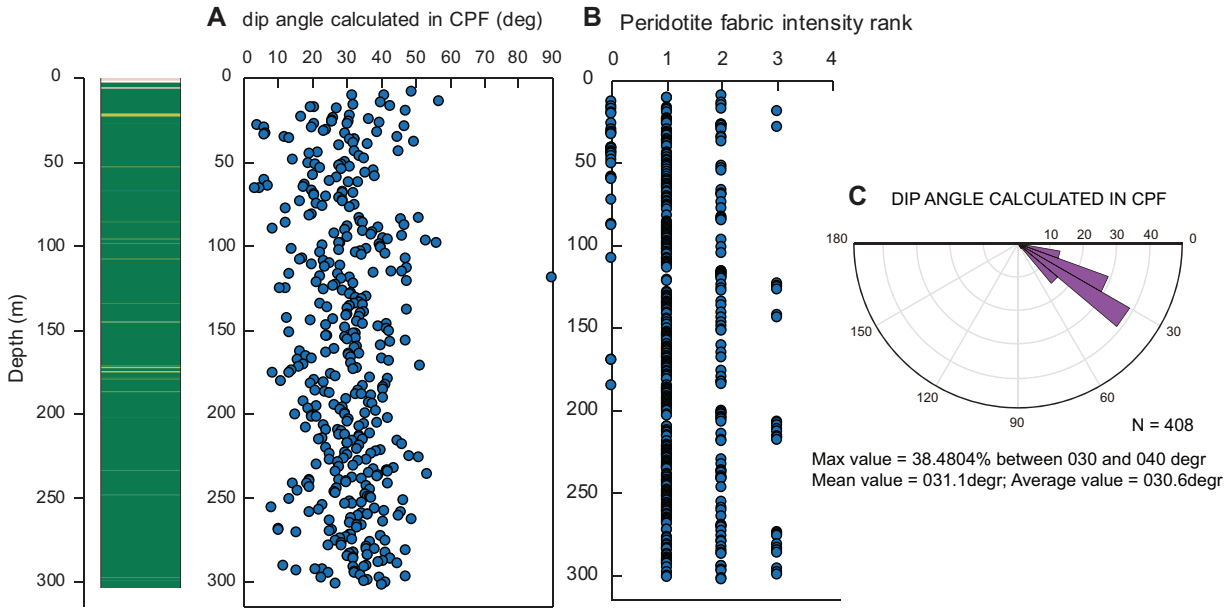

Figure F35. Different types of peridotite fabric defined by geometry of pyroxene. **A.** Harzburgite shows porphyroclastic texture by slightly elongated pyroxene. **B.** Harzburgite shows protomylonitic texture by strongly elongated pyroxene. **C.** Slightly elongated pyroxenes are exhibited by brighter color. **D.** Strongly elongated pyroxenes (brighter color). **E.** Difference of textures between Sections 44Z-1 and 84Z-4. In Section 44Z-1, slightly elongated pyroxenes form porphyroclastic texture. In Section 84Z-4, strongly elongated pyroxenes form protomylonitic texture.

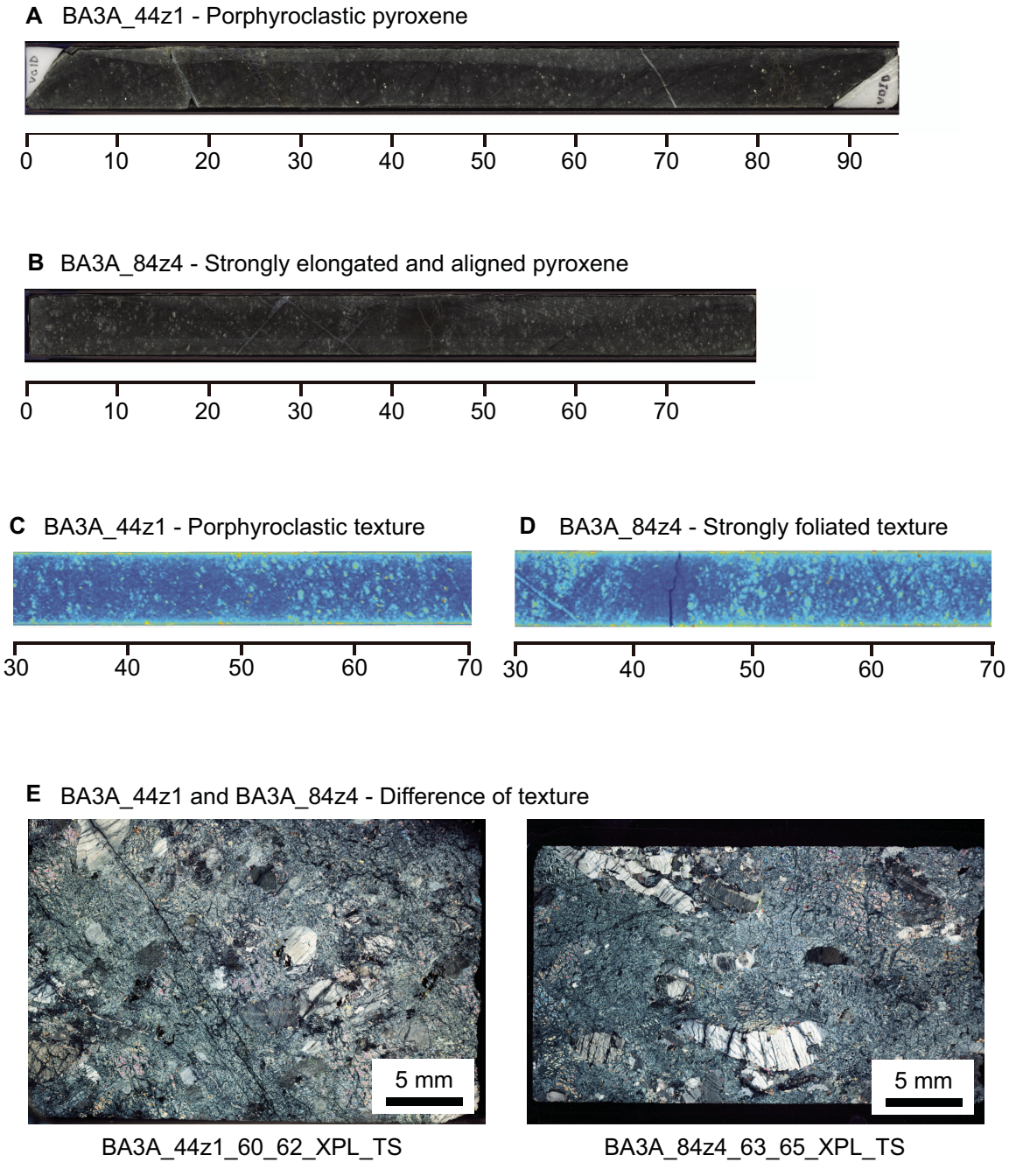

Figure F36. Examples of intrusive textures. **A.** Complete core scan showing one small dike with irregular contacts and one pyroxenite layer with gradational contacts. **B.** Crosscutting between two dikes. **C.** Sharp contact. **D.** Pyroxenite layers with gradational contacts. **E.** Dunite/harzburgite contact. **F.** Garnet-bearing gabbro dikelet. **G.** Clinopyroxenite dike with irregular contacts.

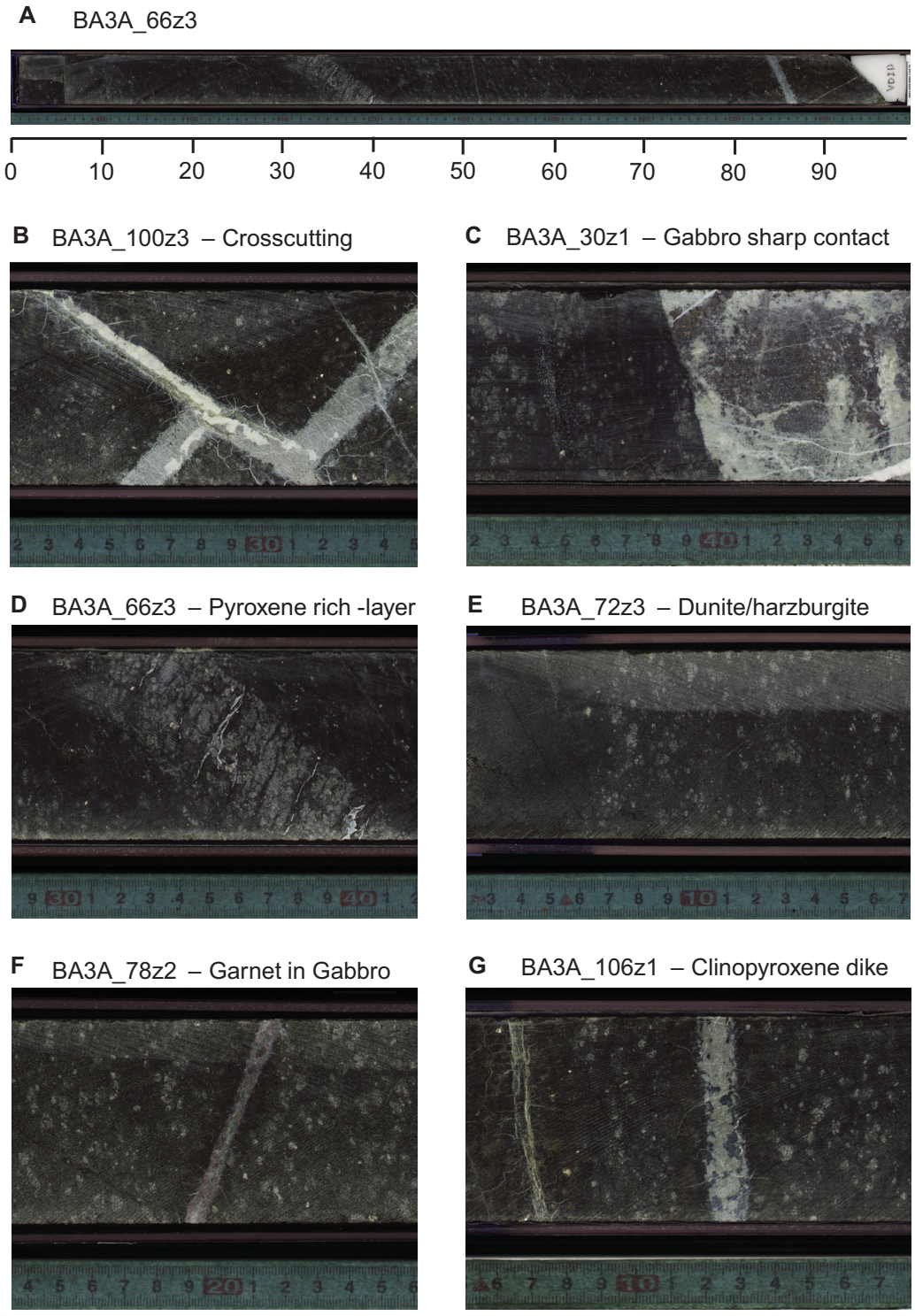

Figure F37. Locations and dip of magmatic contacts plotted with lithologic log of Hole BA3A. Comparative graphic with the apparent thickness vs. depth and rose diagram plots with statistics (using Stereonet 9.5, Cardozo and Allmendinger, 2013) of the dip angle for each type of contact. From left: compilation of all the data, contact dunite/harzburgite (yellow), clinopyroxenitic dike (green), pyroxene layers (light purple), and gabbroic dike (light blue).

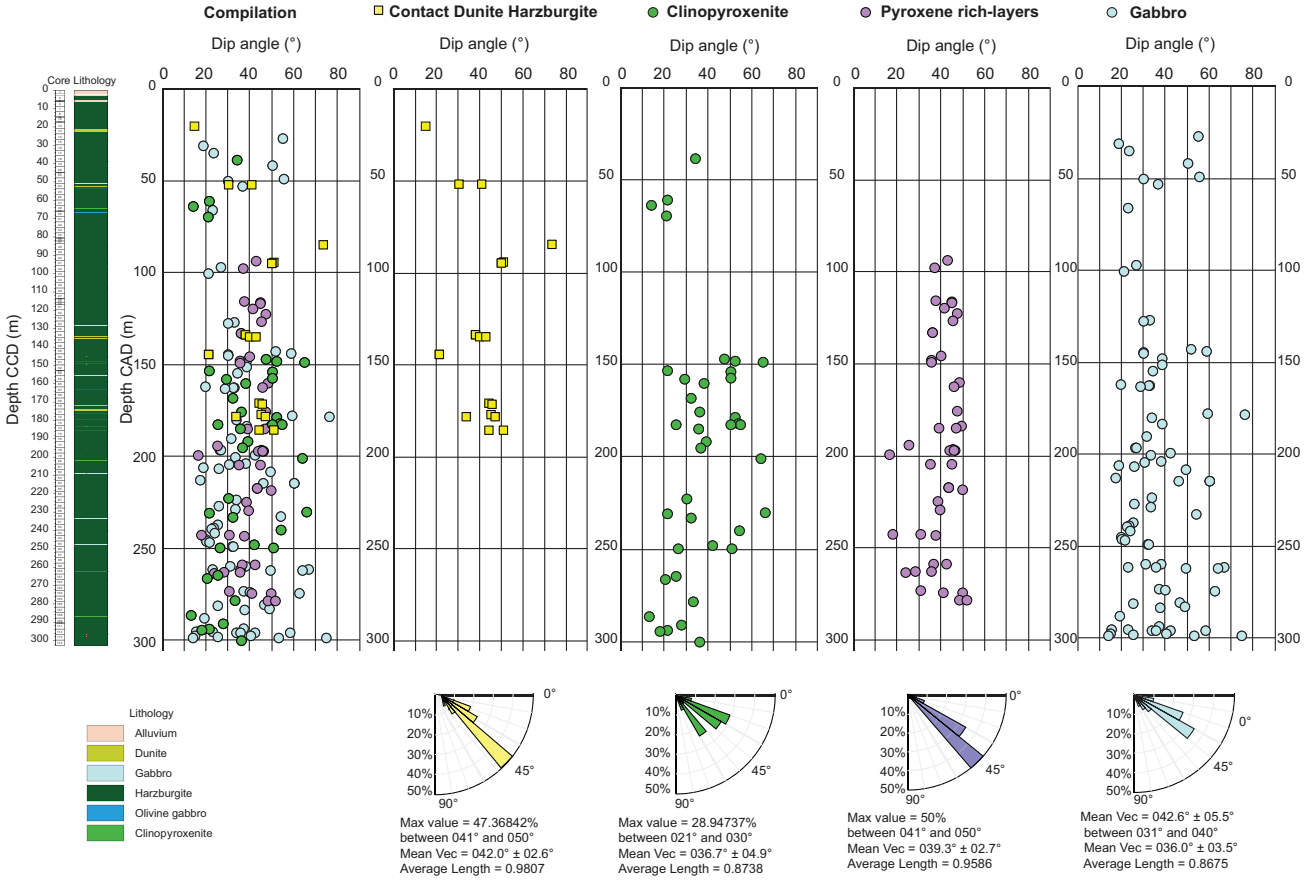

Figure F38. Locations and thicknesses of magmatic contacts plotted with lithologic log of Hole BA3A. Comparative graphic with the dip angle calculated vs. depth. From left: compilation of all the data, clinopyroxenitic dike (green), gabbroic dike (light blue), and pyroxene layers (light purple).

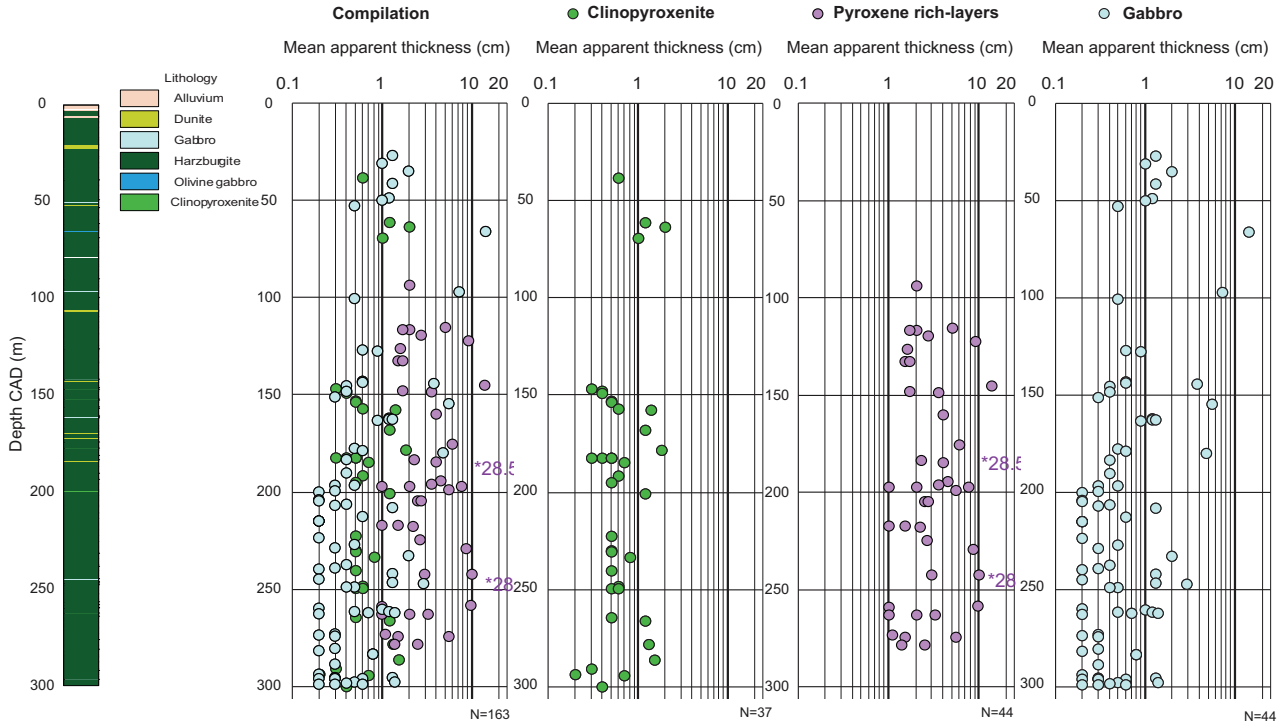

Figure F39. A. Locations and thicknesses of fault zones (red bars) and cataclastic zones (blue bars) plotted with lithologic log of Hole BA3A. **B.** Thicknesses of damage zones for each deformation feature logged vs. depth. Where a feature crossed a discontinuous boundary between two sections of core, the two sides had to be logged as individual features, as the relation between the two sections was not observed. **C.** Plot of deformation intensity rank ascribed to each feature. Intensity increases from 1 to 5; for full explanation of ranking procedure see **Structural geology** in the **Methods** chapter. **D.** Fracture and vein density rank with depth; for full explanation of ranking procedure see **Structural geology** in the **Methods** chapter.

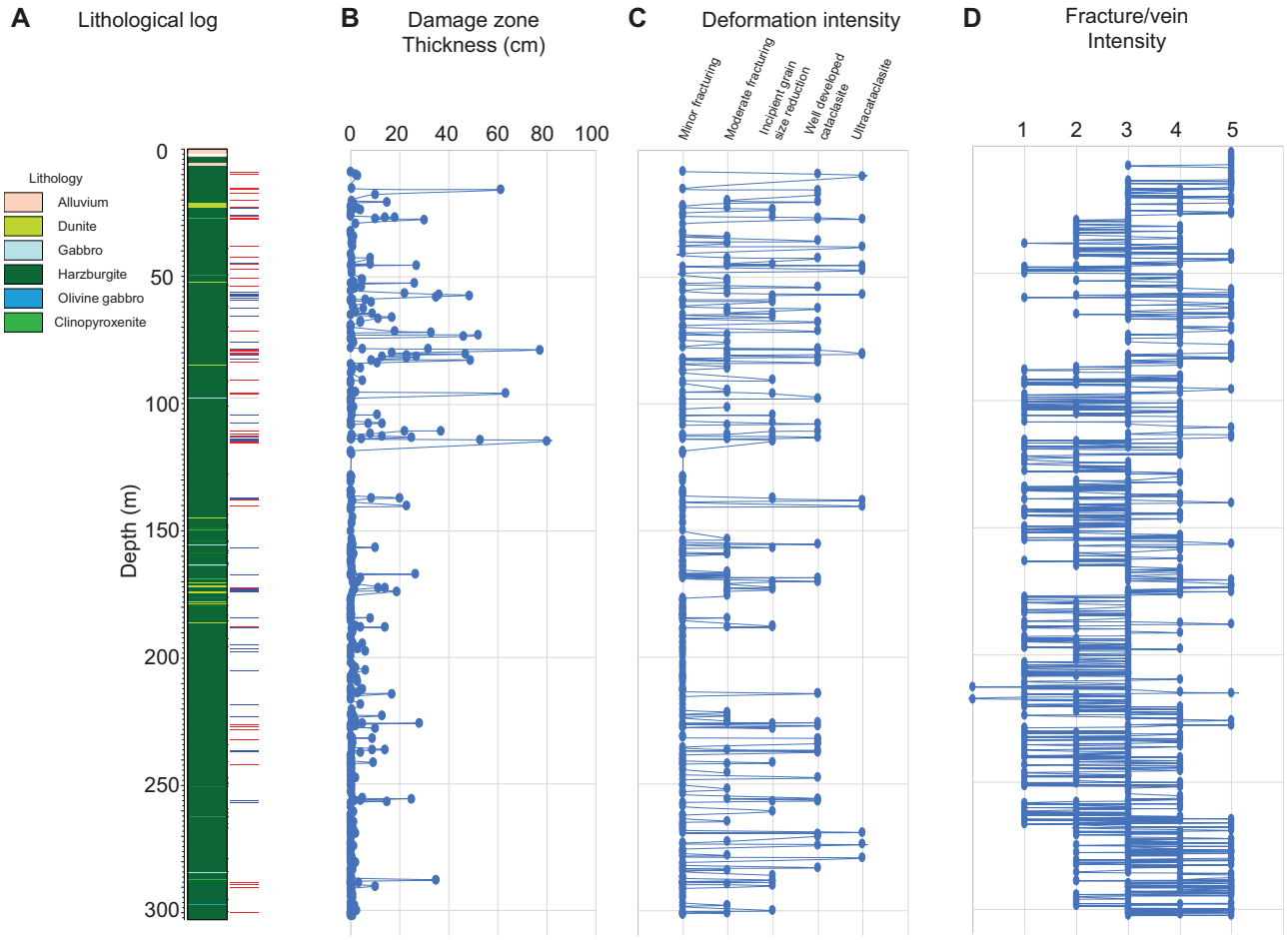

Figure F40. Plots of dip angle for each logged deformation feature in Hole BA3A. (**A**) All features, (**B**) joints, (**C**) cataclastic zones, (**D**) fault zones, (**E**) semibrittle or crystal-plastic shear zones, (**F**) shear veins. Features whose dip could not be accurately measured on the core are not included in this plot.

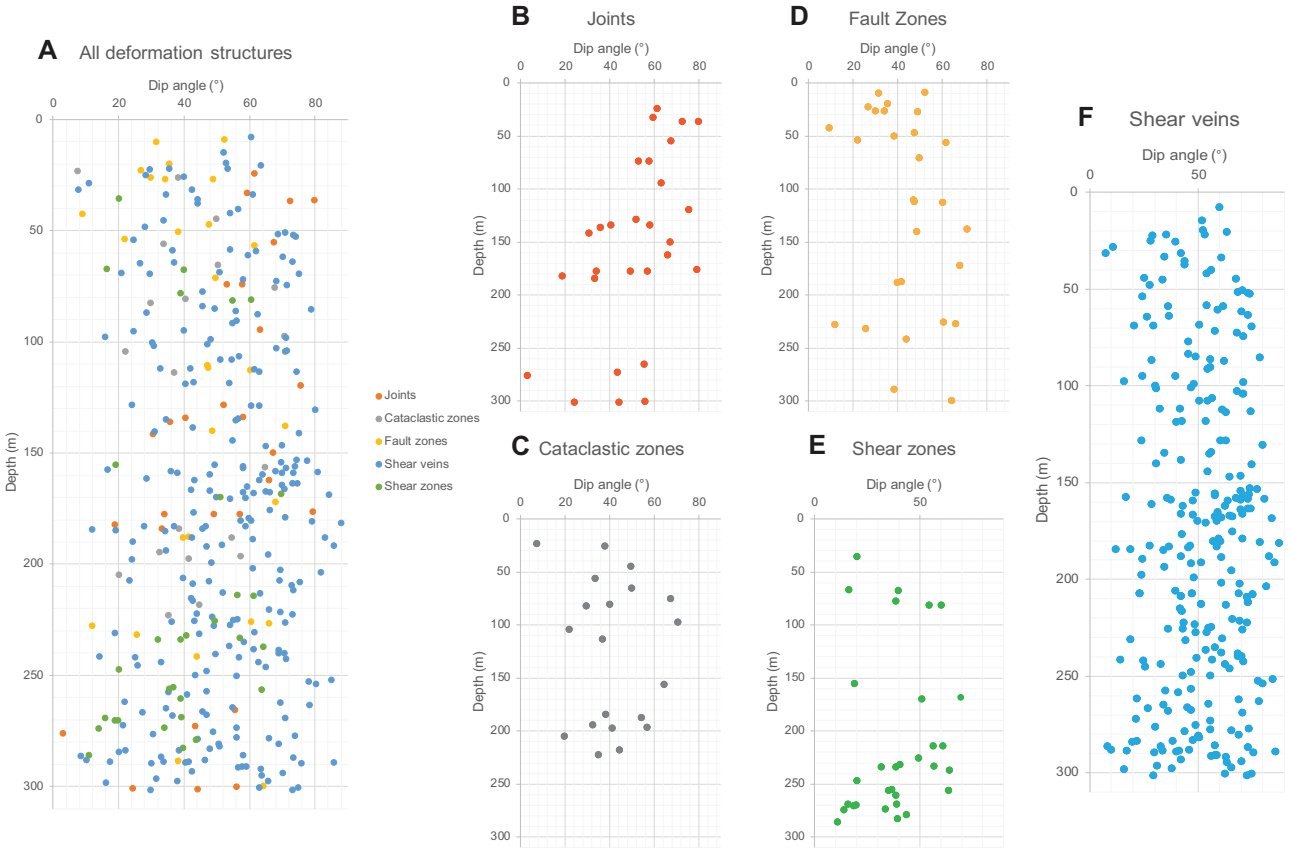

Figure F41. Rose diagrams of the dip angle of deformation structures in Hole BA3A sorted by type of feature. In general, sharper features such as shear veins and joints dip slightly more steeply than the wider deformation zones. Rose diagrams were calculated using stereonet 9.5 (Cardozo and Allmendinger, 2013) with a binning angle of 10°.

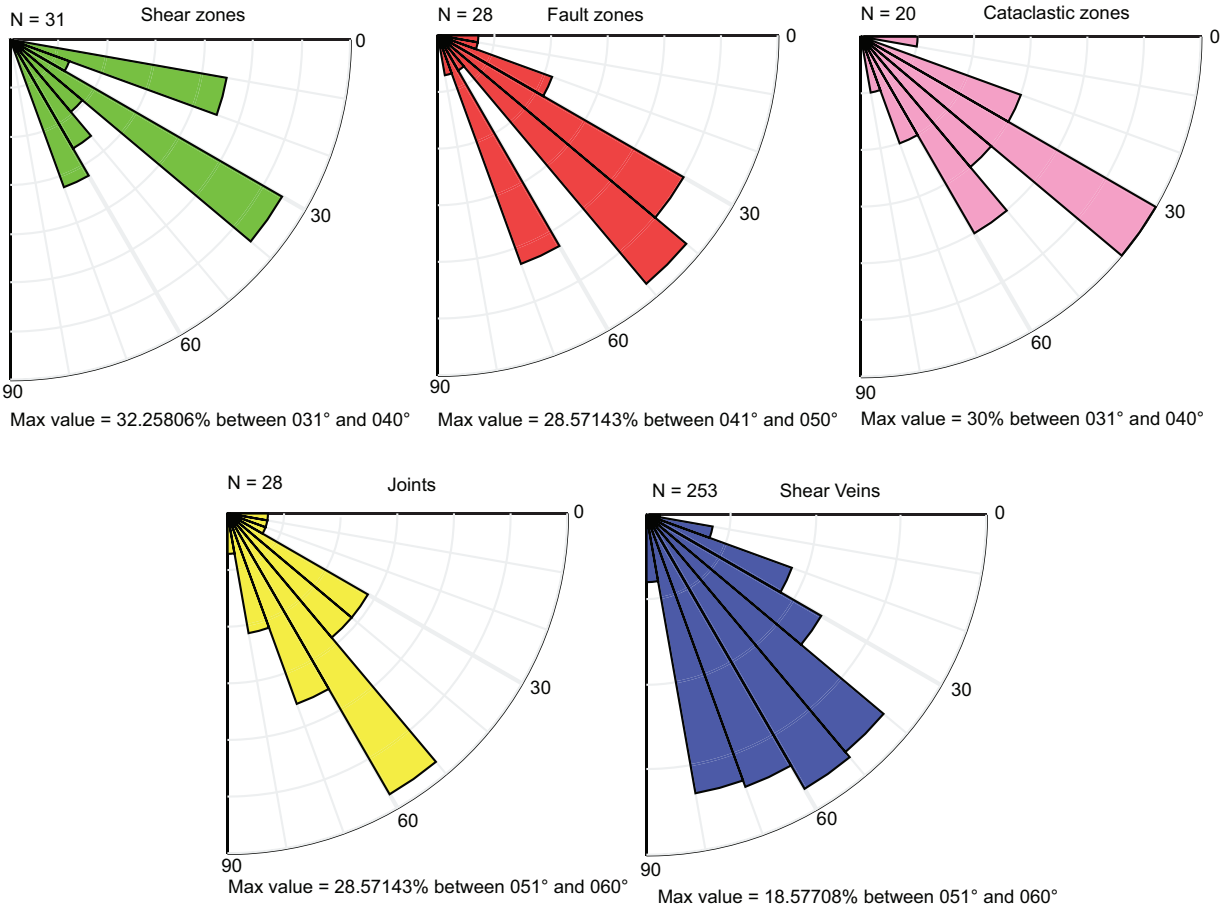

Figure F42. A. Lithologic log of Hole BA3A with locations and thicknesses of fault zones (red) and cataclastic zones (blue). Both fault zones and cataclastic zones are distributed throughout the hole but are somewhat more common and wider in the upper 120 m. **B.** Example of a fault zone from 26 m depth (14Z-4, 26–45 cm) that has an incohesive fractured core and a foliated, cohesive damage zone. **C.** Example of a fault zone from 140 m depth (58Z-4, 0–24.5 cm) that is composed almost entirely of incohesive fault gouge. The distinct coloration of this fault zone with respect to the wall rock may suggest localization of the fault within a heavily altered dike. **D.** Example of a cataclastic zone from 174 m depth (71Z-1, 15.5–34.5 cm). The cause of this zone of fracturing is unclear partly due to the out of situ nature of the material. It was logged as a cataclastic zone to highlight the distinction between this and a clear fault zone.

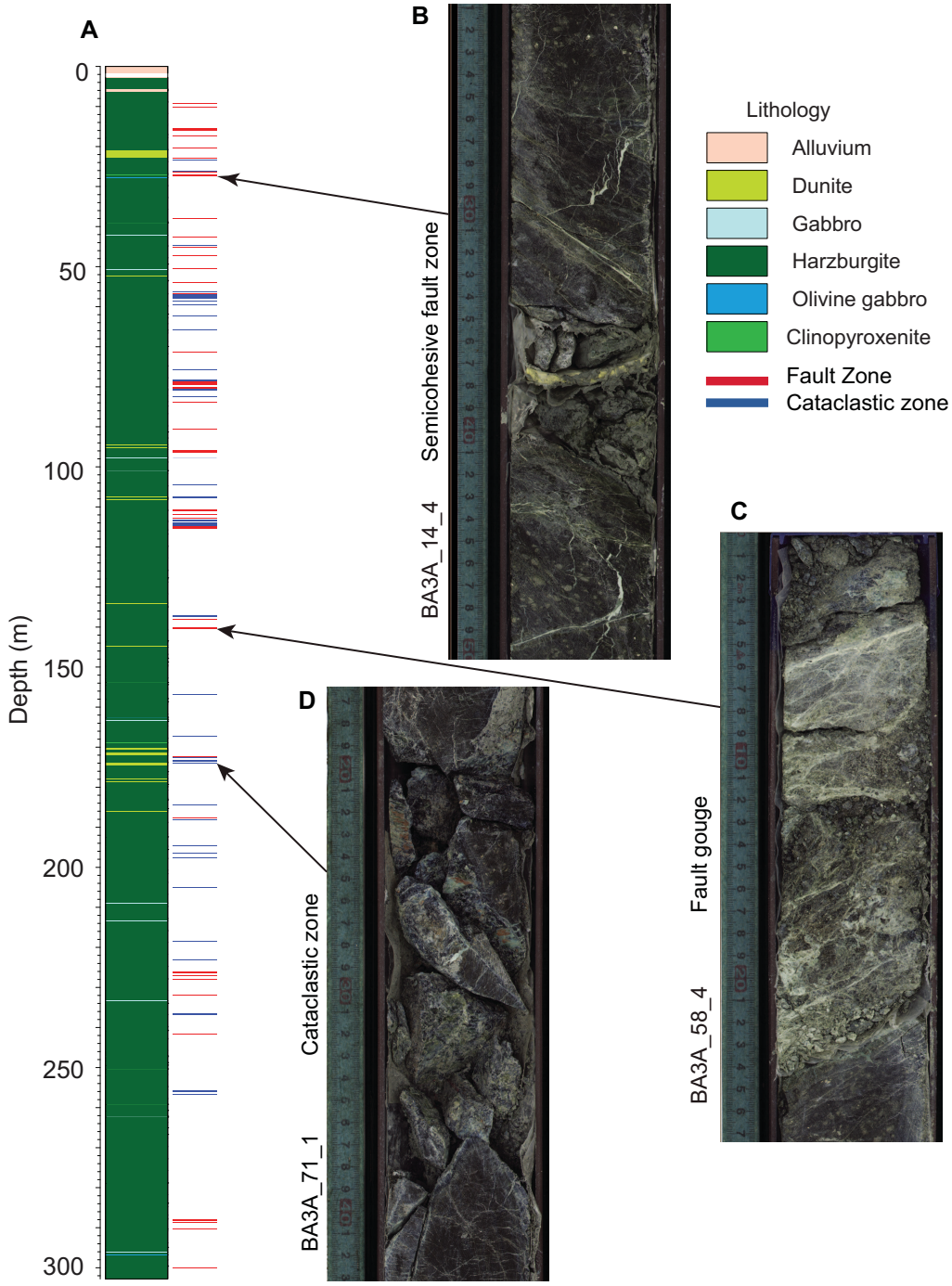

Figure F43. A. Fine, parallel, white incipient veinlets dispersed across a wide area. These are inferred to represent a somewhat homogeneous distribution of strain across the area concerned. **B.** Typical shear vein intersecting the core surface at a low angle and revealing mineral lineations on the slip surface. **C.** Wide shear zone with an aligned crystal-plastic fabric bounded along the lower surface by a shear vein or brittle slip surface. **D.** Narrow crystal-plastic shear zone.

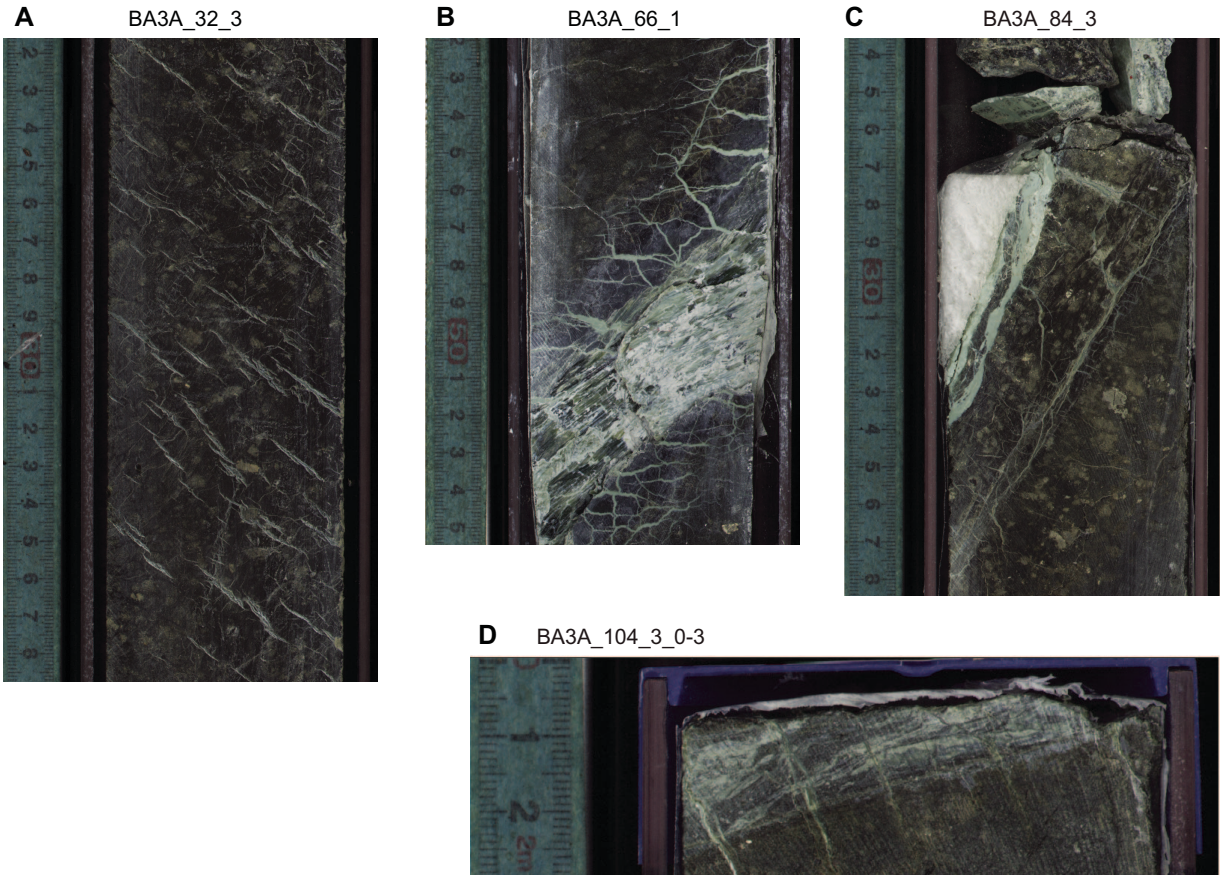

Figure F44. A. Plot of dip angles of features that display an offset, sorted into apparent normal or reverse shear sense based on that offset. Large offsets could not be captured within the core so this data set is biased toward features with smaller, observable displacement. The shear sense given is that which was apparent when viewing the feature on the cut surface of the core. Features with a reverse apparent shear sense (compressional) are more abundant in the lower part of the hole below ~175 m depth, whereas normal apparent offsets (extensional) are distributed more evenly throughout the core. **B.** Plot of lineation plunge showing that most high-angle (>40°) slip lineations occur at ~40–110 m and that below this depth the majority of lineations have a very shallow plunge usually indicative of strike-slip shear. There is a notable recurrence of higher angle plunges at the very bottom of the hole. **C.** Plunge angle vs. dip angle of the plane on which they were measured. Points along the diagonal line are dip-slip (plunge similar to dip), points along the y-axis are strike-slip (plunge << dip), and points in between are oblique-slip (plunge < dip). Points beyond the diagonal line are likely due to the wavy nature of some of the measured planes; however, these points can be assumed to relate to dip-slip features.

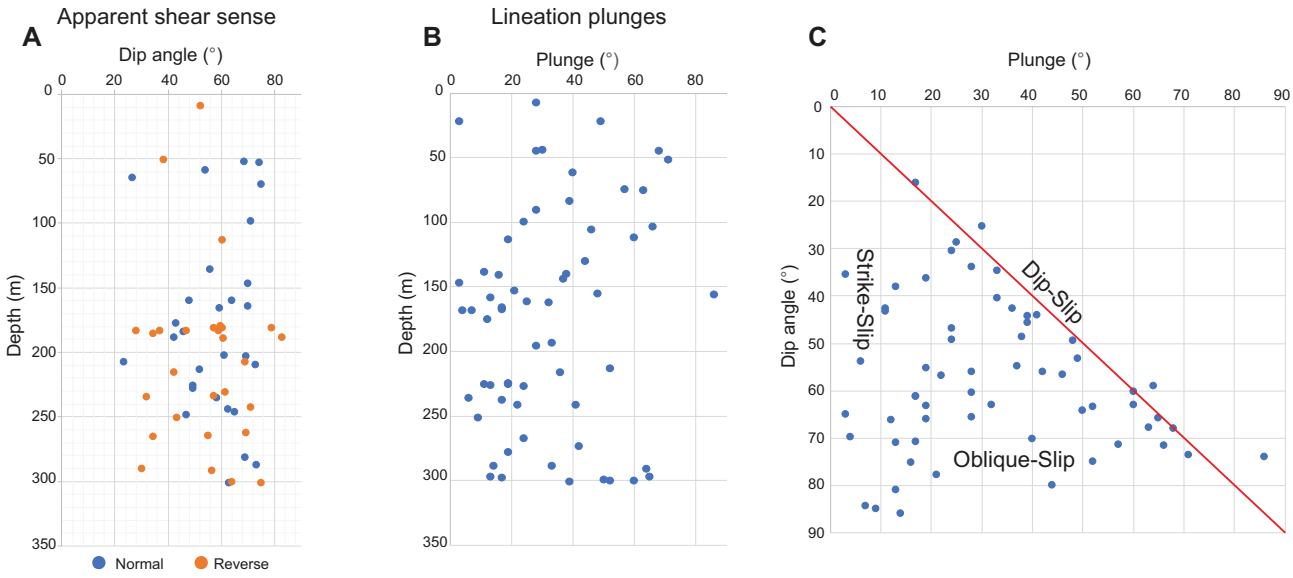

Figure F45. A. Narrow shear zone localized along the upper surface of a dike (34Z-5, 17–29 cm). **B.** Whole thin section scan with the edges of the main deformed zone highlighted in red (64Z-5, 22–26 cm; XPL). Much of this zone is composed of fine-grained fibrous serpentine. **C, D.** Photomicrographs of the region highlighted in the yellow box in (C) XPL and (D) with the lambda plate inserted reveal the presence of a strong preferred orientation within the fibrous serpentine.

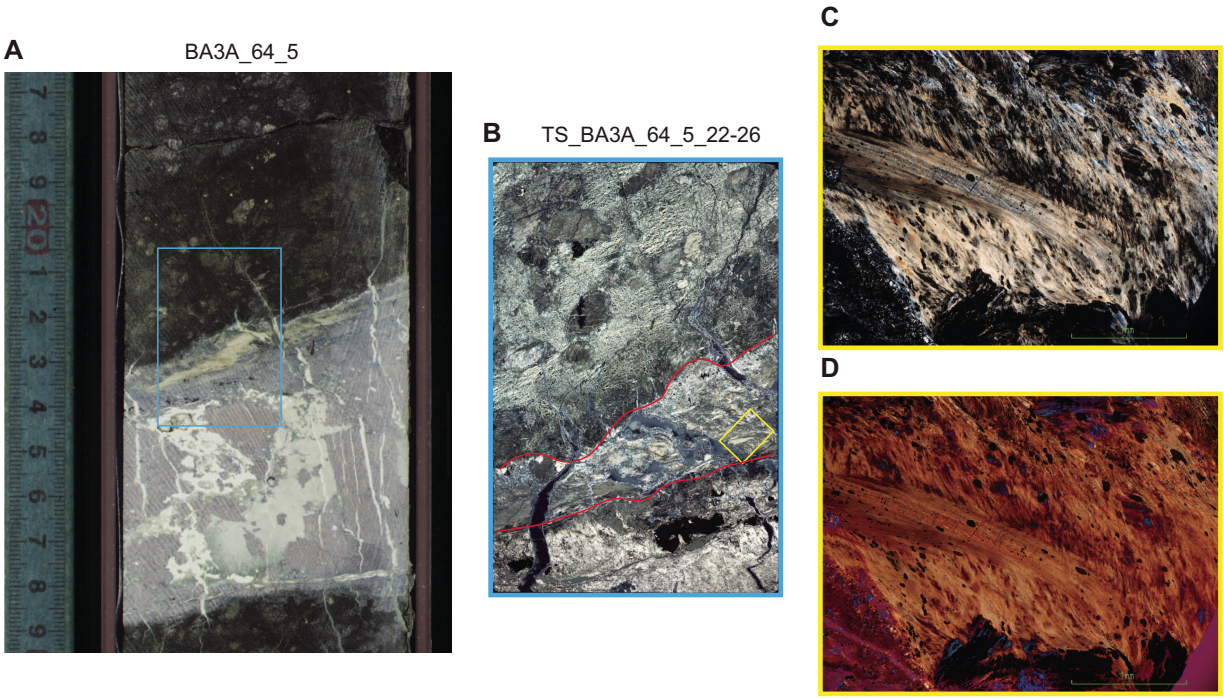

Figure F46. Variation of dip angles of different alteration vein types, compiling dips of all carbonate, carbonate-serpentine, serpentine, and occasional xonotlite veins in Hole BA3A. Lithologic column and occurrences of fault and cataclastic zones (red and blue lines next to the column) for comparison.

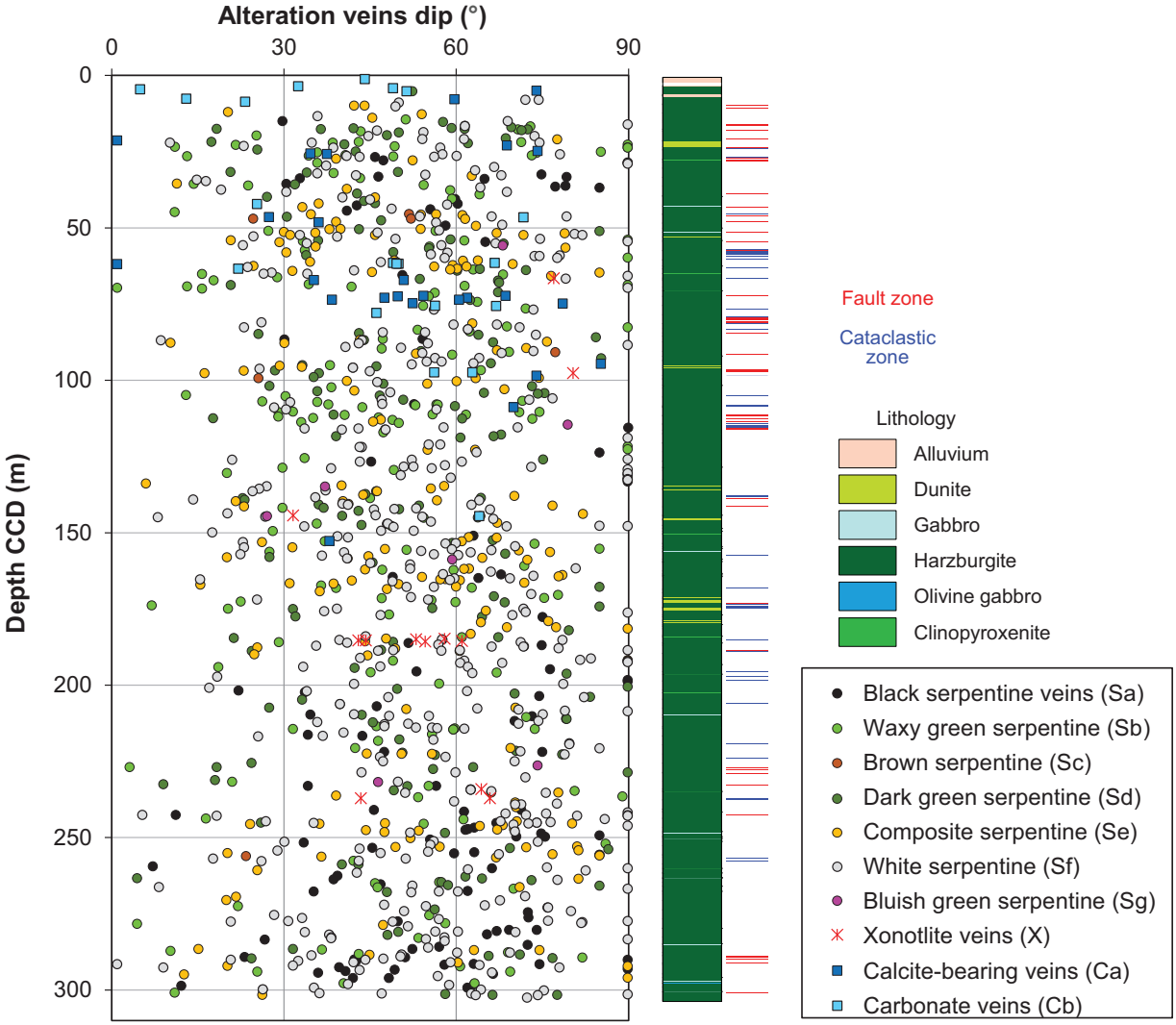

Figure F47. Variations of dip angles of the most abundant carbonate and serpentine vein types superposed on dip angles of all serpentine veins, and overall rose diagrams of their dips weighted by vein density (using as a preliminary weighting factor the vein density defined by values 1–5; see **Veins** in the **Methods** chapter). Note that black serpentine veins (Sa) were only measured where clear orientations emerged from the background mesh texture; therefore, their frequency with depth is not representative for their true abundance. Rose diagrams are calculated using stereonet 9.5 (Cardozo and Allmendinger, 2013) with a binning angle of 10°.

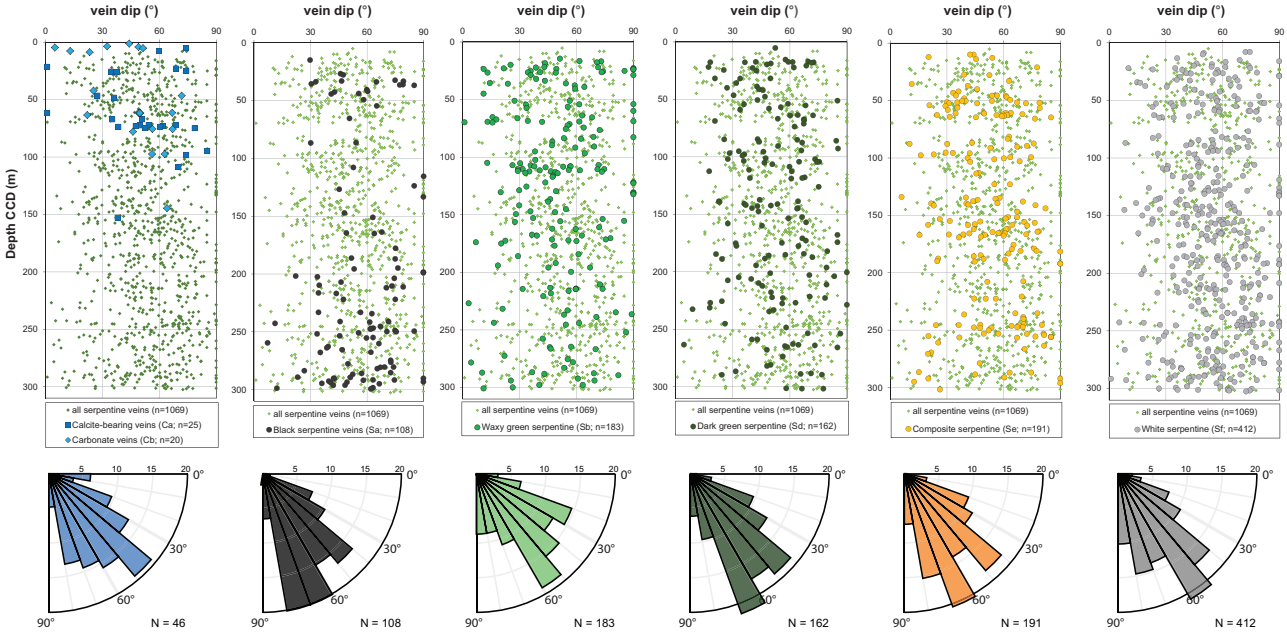

Carbonate veins (Ca, Cb)
Mean Vec = 049.7° ± 04.7°

Sa Serpentine veins
Mean Vec = 057.2° ± 02.7°

Sb Serpentine veins
Mean Vec = 047.8° ± 02.5°

Sd Serpentine veins
Mean Vec = 052.5° ± 02.5°

Se Serpentine veins
Mean Vec = 053.4° ± 02.3°

Sf Serpentine veins
Mean Vec = 054.4° ± 01.3°

Figure F48. A. Whole thin section scan showing a sheared serpentinite vein with clear orthogonal riedel type shears cutting across its width (101Z-2, 4–7 cm; XPL). The terminations of many of these fractures coincide with small veinlets perpendicular to the main vein that cut across what is either an altered halo or the remnant of an original pyroxenite dike inside which the vein has formed. **B.** Core scan of part of Section 101Z-2 showing the location of the thin section in A. Many of the orthogonal shear fractures are visible even at the mesoscale. **C.** Detail of area highlighted in A revealing the presence of many more microfaults and microfolds than those observable at a larger scale (XPL). These faults are clearly defined by the displacements of sequential layers of serpentine which would have initially formed parallel to the vein walls during the growth of a large composite vein prior to deformation. **D.** Detail of area highlighted in C showing how individual layers or sequences of layers can be traced across the microfault planes (XPL).

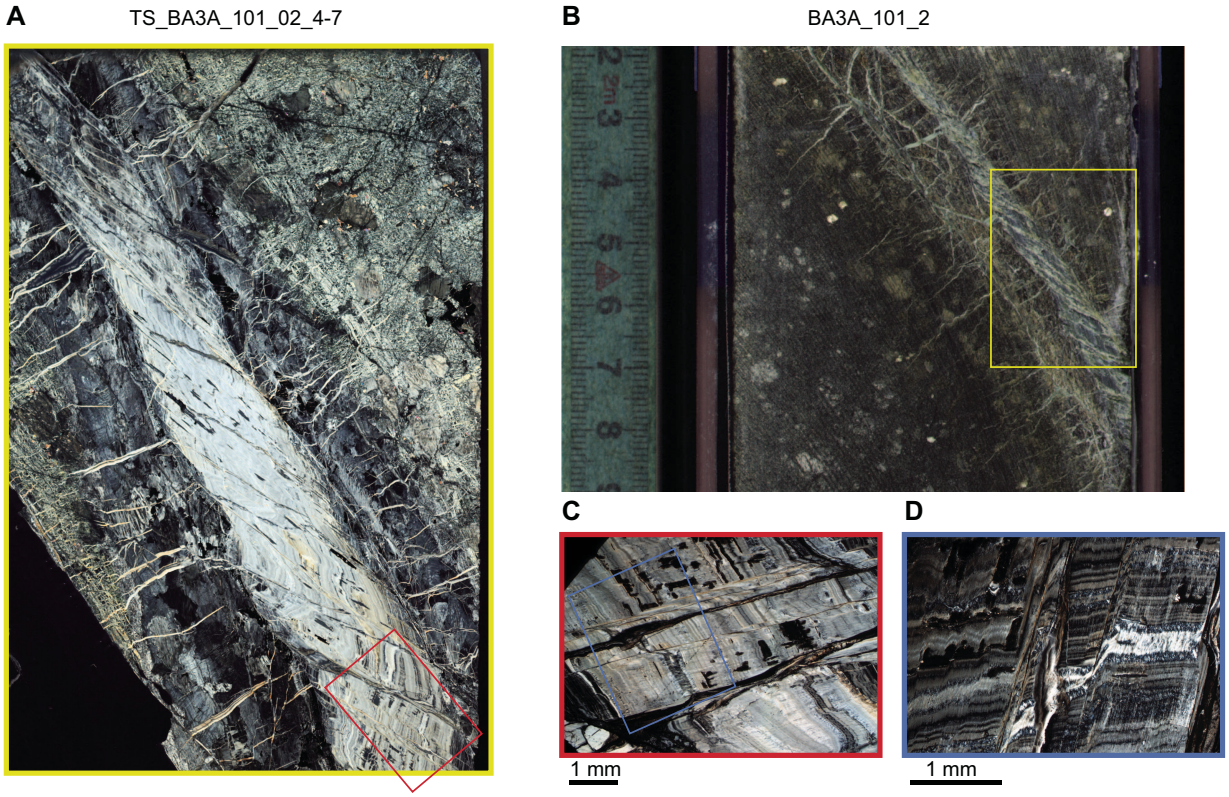

Figure F49. A. Whole thin section scan showing a very narrow slip surface offsetting a dike by 2 cm (101Z-2, 40–43 cm; XPL). **B.** Core scan photograph of part of Section 101Z-2 highlighting the location of the thin section in A. Small offsetting structures such as this are common in Hole BA3A. **C.** Detail of the area highlighted in A showing the narrow slip surface and a region of undeformed serpentine crystals which have grown syntaxially, possibly into a void along the slip plane (XPL). This horizon of euhedral serpentine is discontinuous along the length of the slip surface. **D.** Example of a feature that appears similar in the core at the macroscale, also offsetting a dike by 2 cm, but is actually formed of several anastomosing slip surfaces (Sample 111Z-2, 20.5–23.5 cm; XPL).

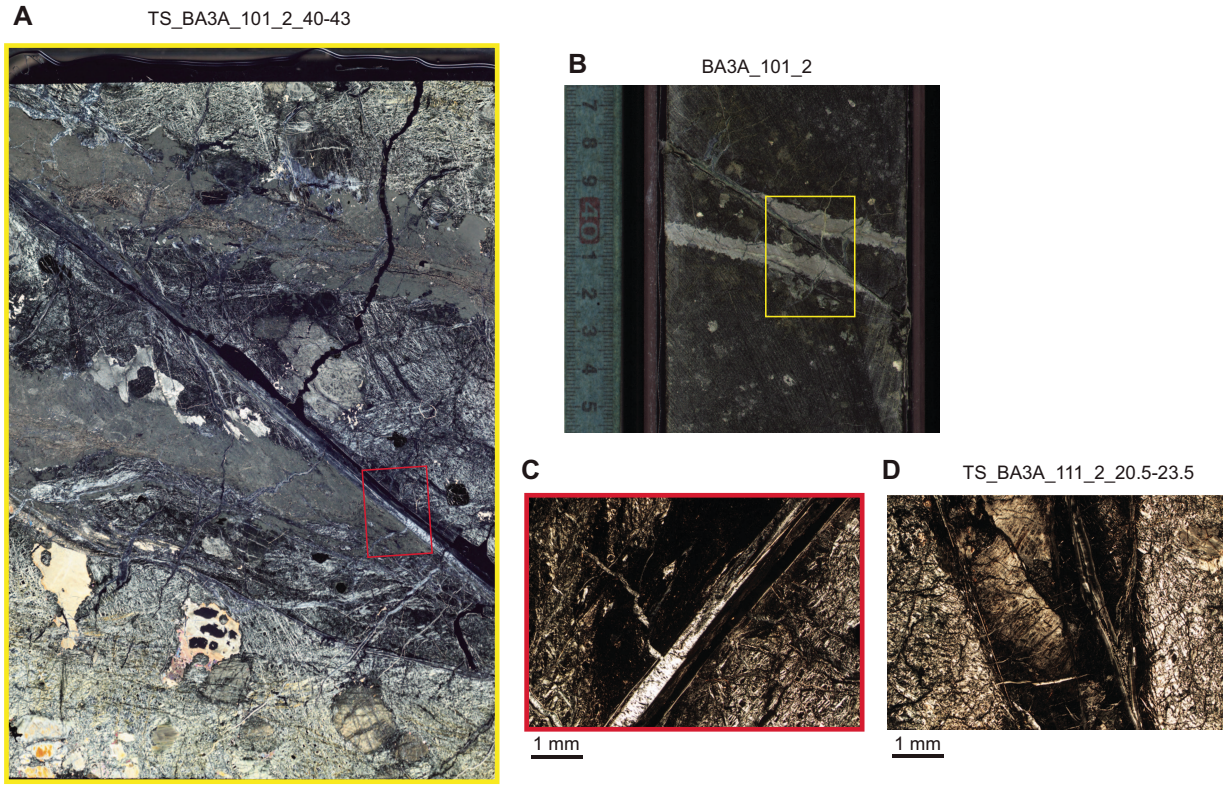

Figure F50. Fragmented serpentinite clasts in carbonate vein at 7.78 m depth (Section 3Z-3) suggesting local crystallization-driven brecciation.

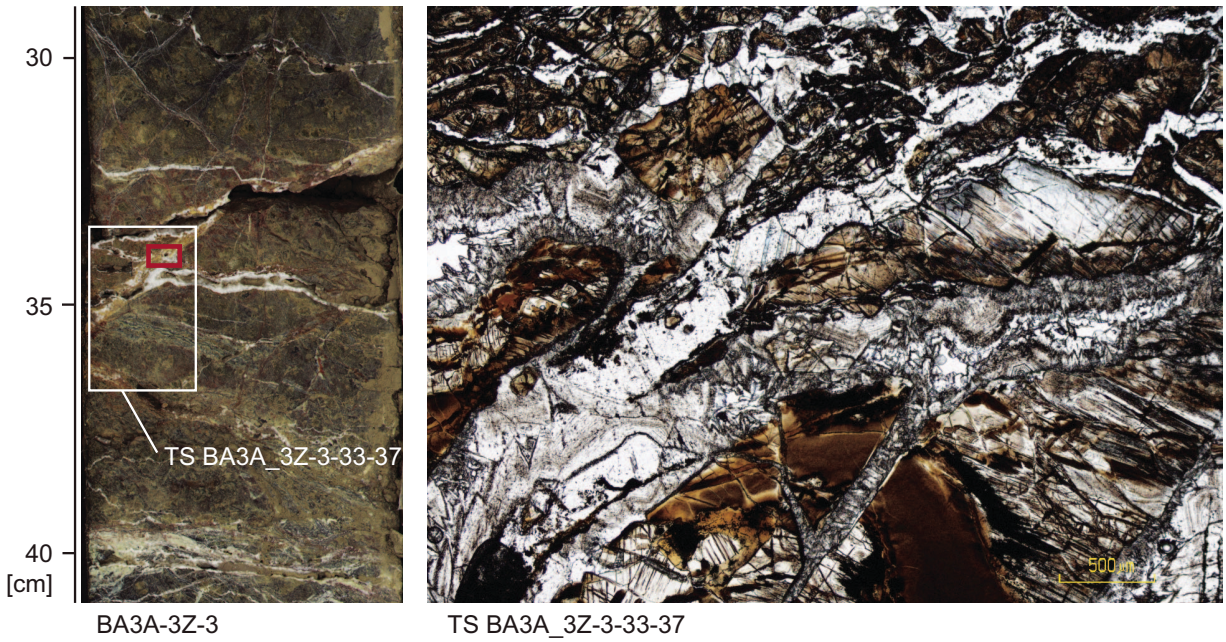

Figure F51. Plots: (**A**) LOI, (**B**) Mg#, (**C**) TiO_2, (**D**) Ni, (**E**) Cr, Hole BA3A. Semitransparent diamonds = Hole BA1B values. Green vertical bars = Oman ophiolite values from literature (i.e., Hanghoj et al. 2010; Godard et al., 2000; Rospabé et al., 2018; Takazawa et al., 2003; Khedr et al., 2014; Lippard et al., 1986; Monnier et al., 2006).

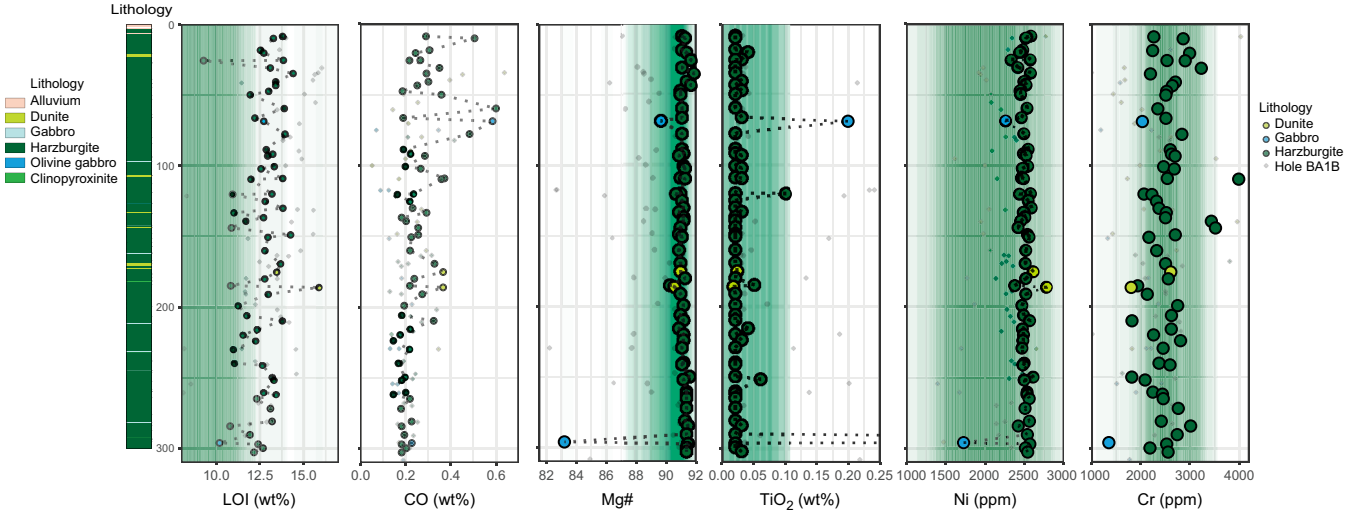

Figure F52. (**A**) CO_2 and (**B**) H_2O contents vs. LOI, Hole BA3A.

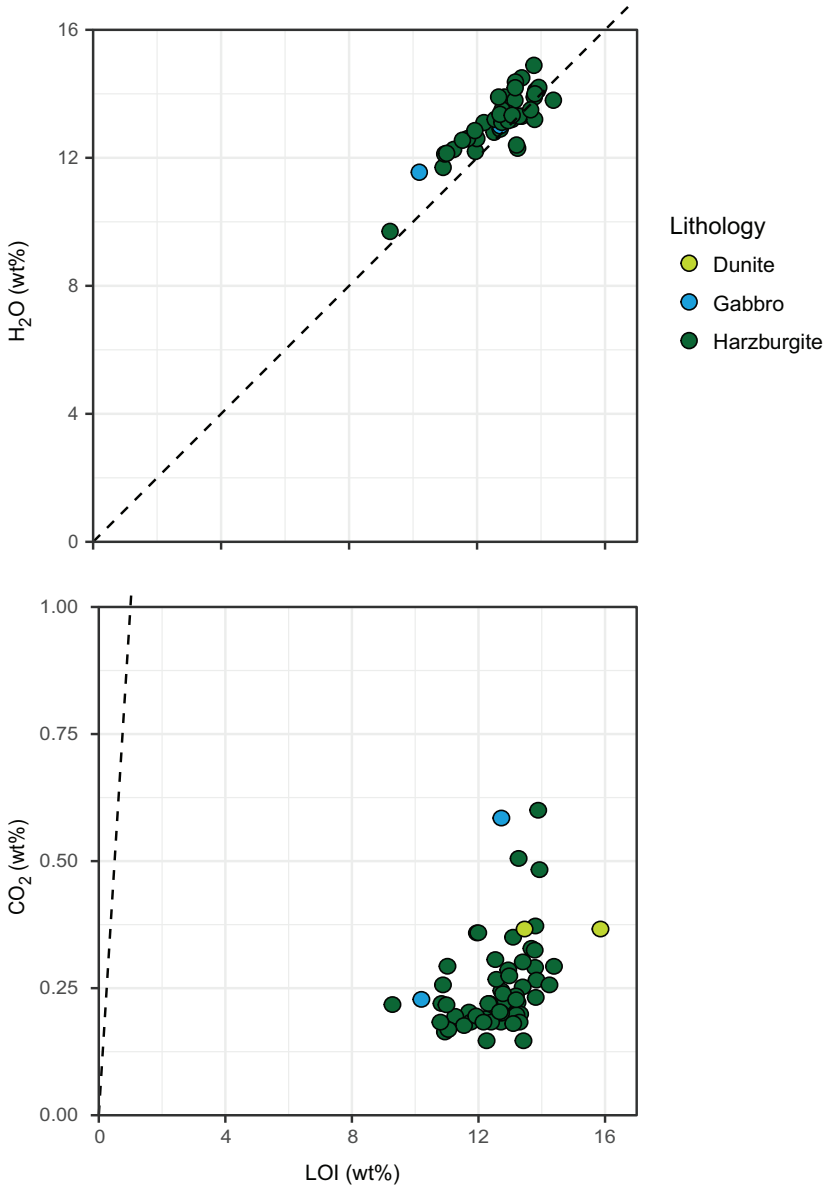

Figure F53. Al_2O_3 vs. (**A**) SiO_2, (**B**) Fe_2O_3, (**C**) CaO, and (**D**) MgO. Semitransparent circles represent Oman ophiolite values from literature data (i.e., Hanghoj et al. 2010; Godard et al., 2000; Rospabé et al., 2018; Takazawa et al., 2003; Khedr et al., 2014; Lippard et al., 1986; Monnier et al., 2006).

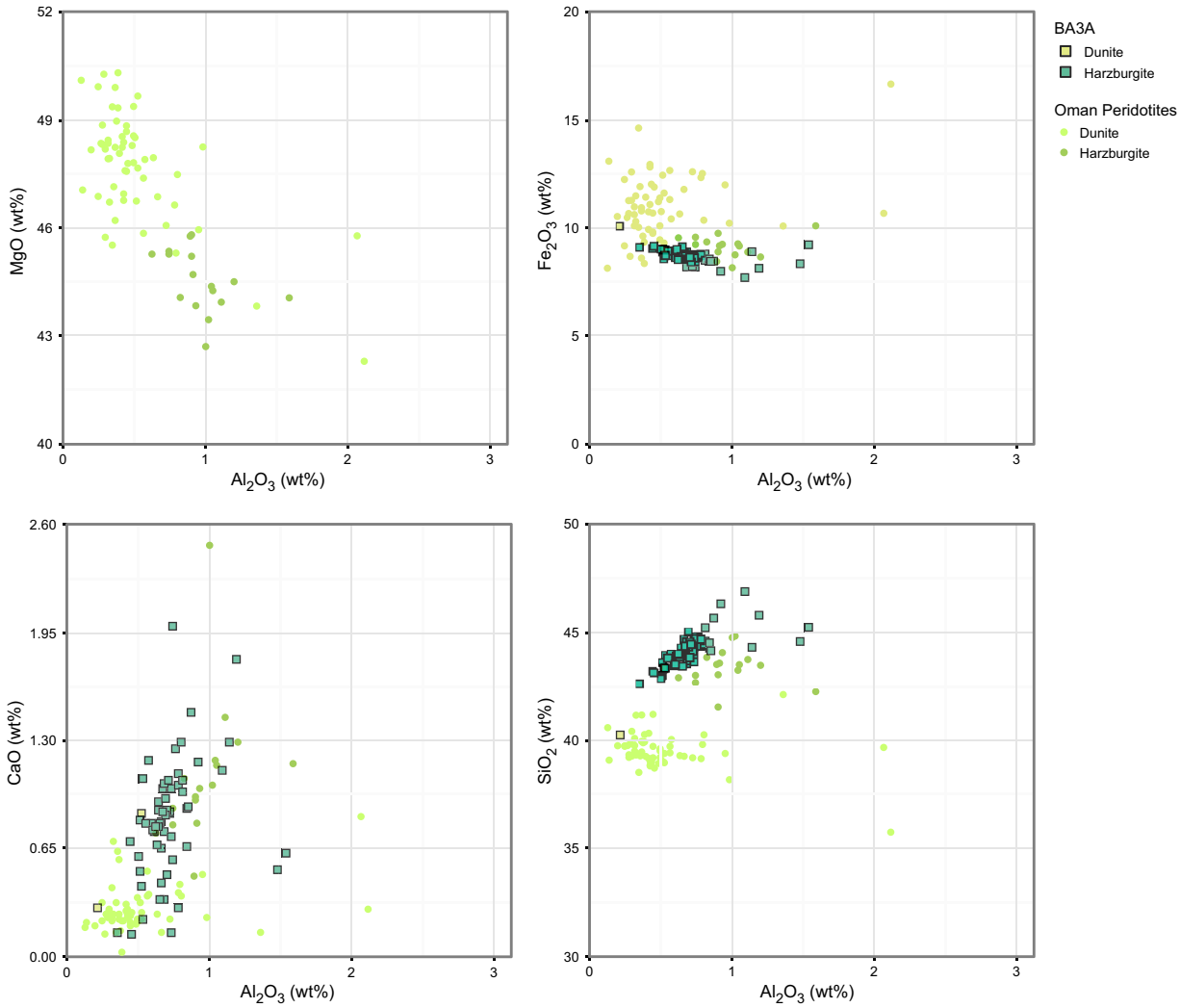

Figure F54. Plots of (**A**) TiO_2, (**B**) V, and (**C**) Cr vs. Al_2O_3. Semitransparent circles represent Oman ophiolite values from literature data (i.e., Hanghoj et al. 2010; Godard et al., 2000; Rospabé et al., 2018; Takazawa et al., 2003; Khedr et al., 2014; Lippard et al., 1986; Monnier et al., 2006).

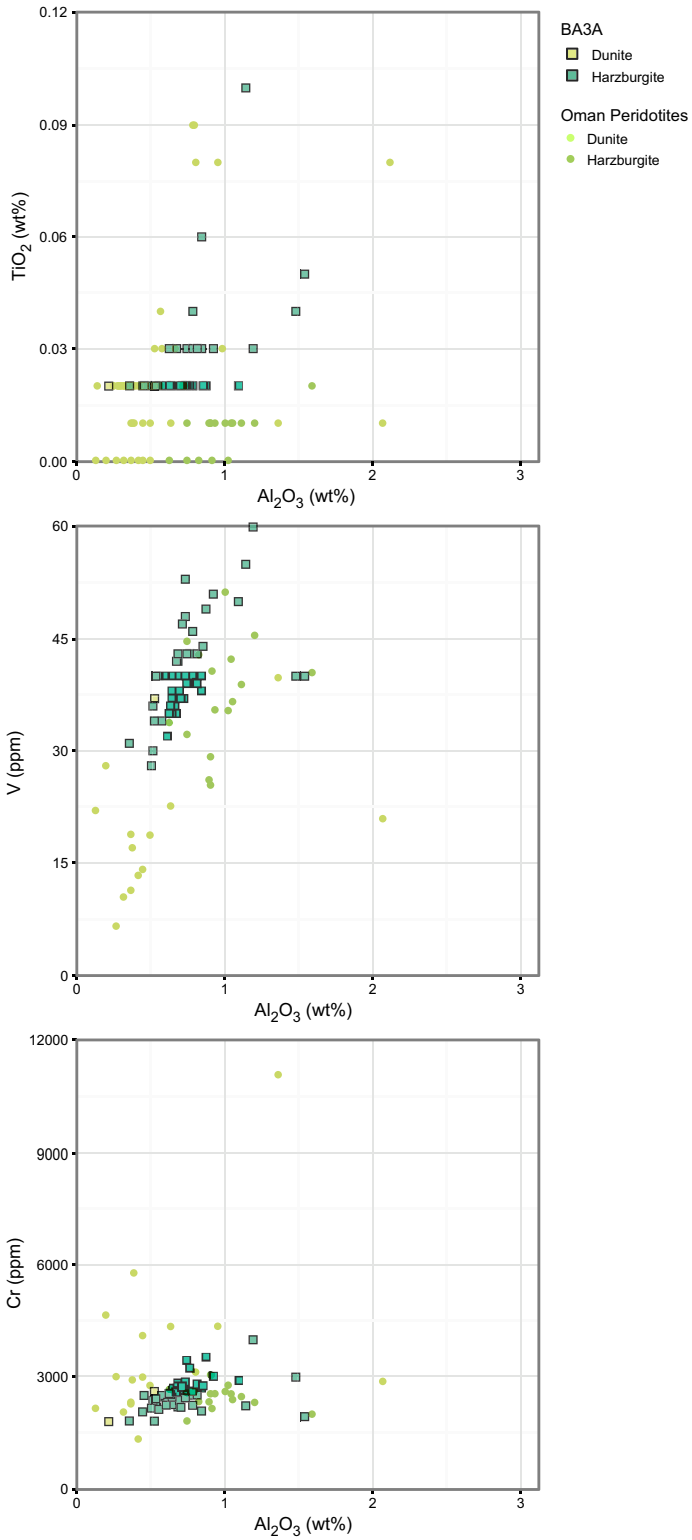

Figure F55. Plot of Ni vs. Mg# for Hole BA3A. Semitransparent circles represent Oman ophiolite values from literature data (i.e., Hanghoj et al. 2010; Godard et al., 2000; Rospabé et al., 2018; Takazawa et al., 2003; Khedr et al., 2014; Lippard et al., 1986; Monnier et al., 2006).

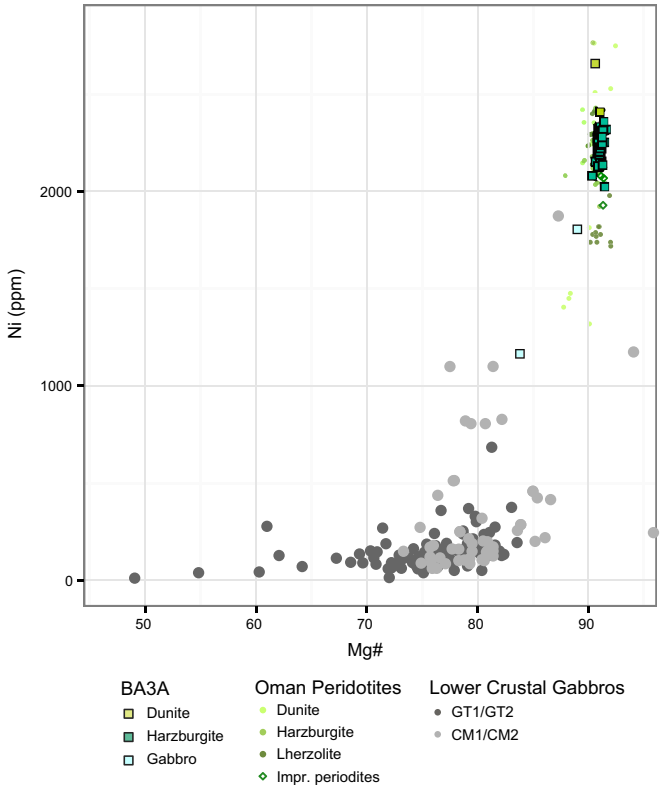

Figure F56. Plots of SiO_2 vs. (**A**) MgO, (**B**) Fe_2O_3, (**C**) TiO_2, (**D**) CaO, and (**E**) Al_2O_3. Grey semitransparent circles represent data from Holes GT1 and GT2 of the Oman Drilling Project. Green semitransparent circles represent data from Oman ophiolite literature (i.e., Hanghoj et al. 2010; Godard et al., 2000; Rospabé et al., 2018; Takazawa et al., 2003; Khedr et al., 2014; Lippard et al., 1986; Monnier et al., 2006).

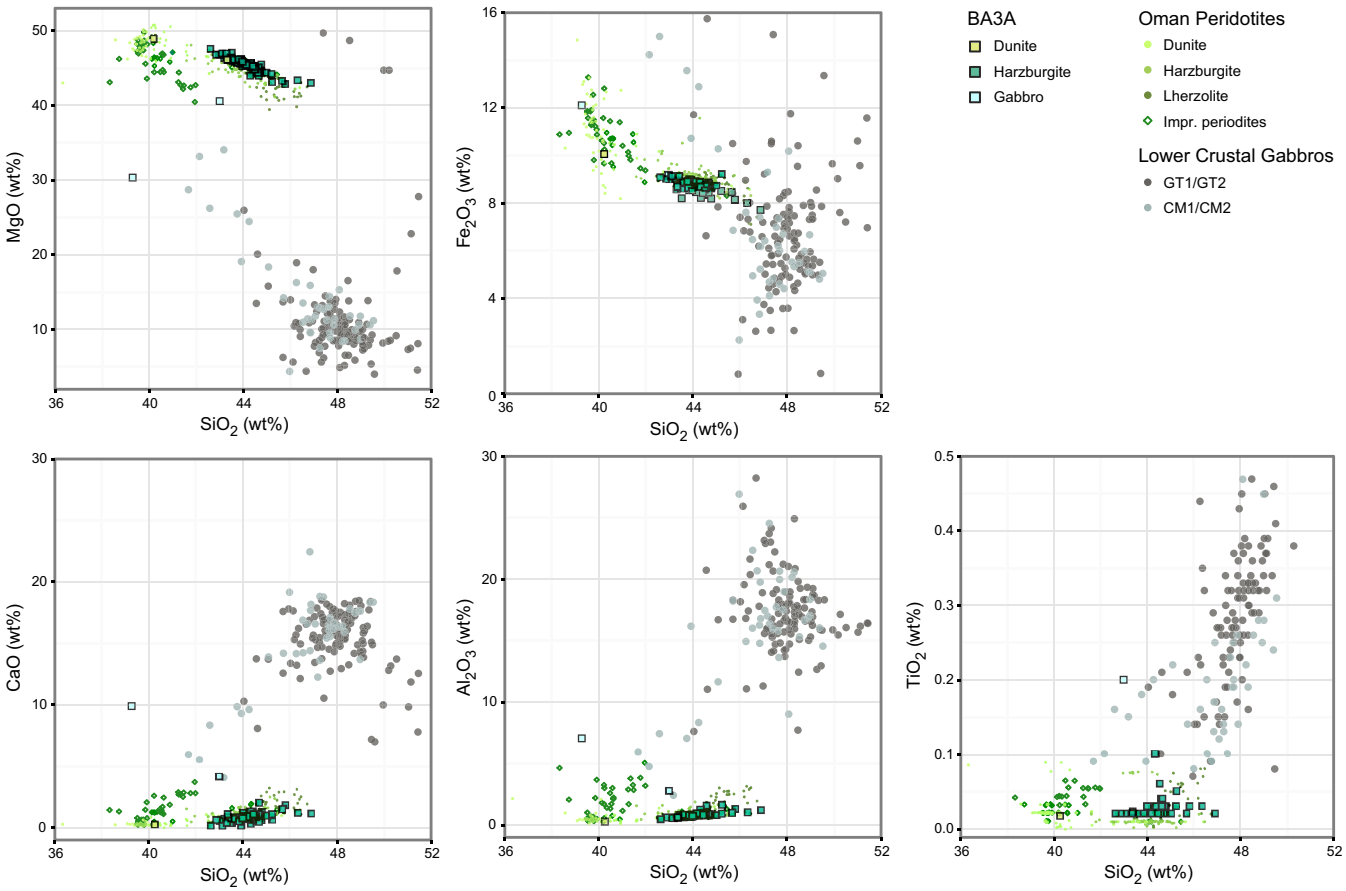

Figure F57. Downhole plots of NRM intensity, bulk (volume) magnetic susceptibility, and Koenigsberger ratios (*Q*), Hole BA3A.

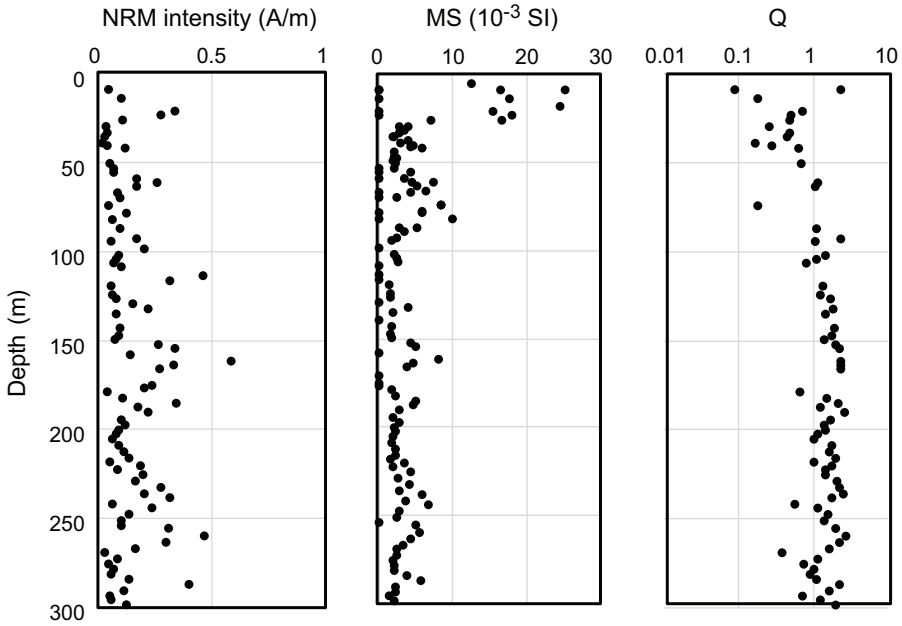

Figure F58. Downhole plots of NRM inclinations and ChRM inclinations isolated from principal component analysis, Hole BA3A.

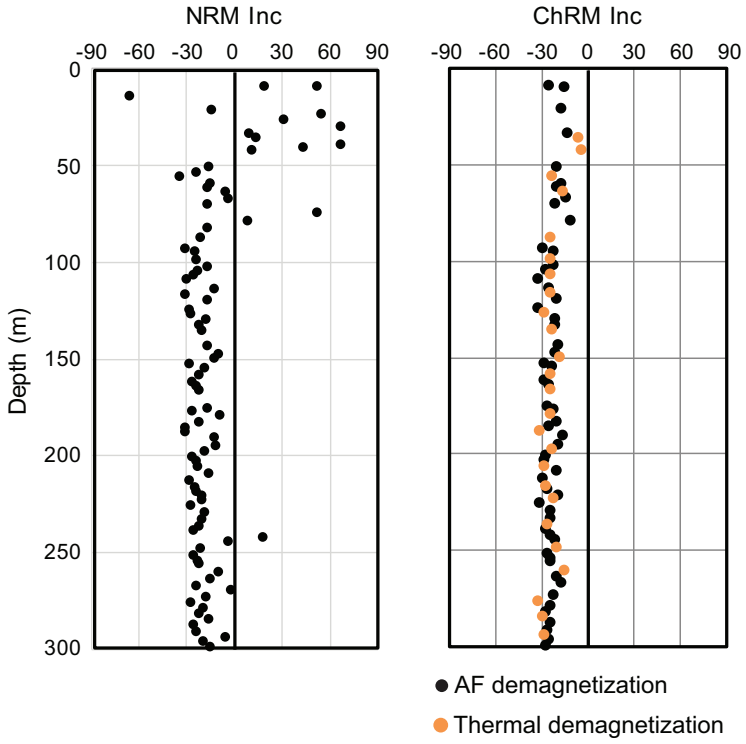

Figure F59. A. Representative orthogonal vector projections displaying behavior of magnetic remanence directions during progressive AF demagnetization of discrete samples. **B.** Changes in normalized remanence intensity as a function of field strength, Hole BA3A.

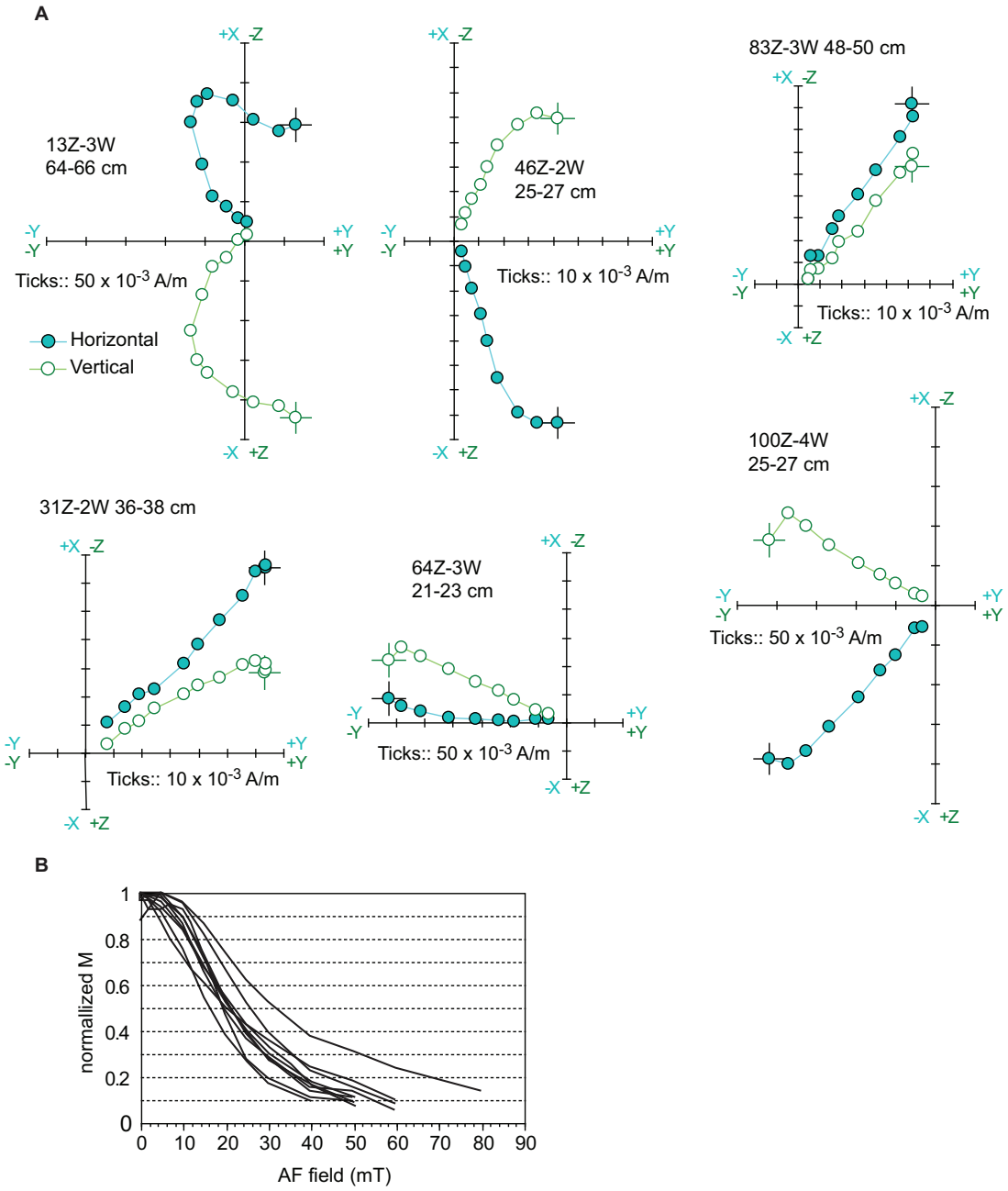

Figure F60. A. Representative orthogonal vector projections displaying behavior of magnetic remanence directions during progressive thermal demagnetization of discrete samples. **B.** Changes in normalized remanence intensity as a function of temperature, Hole BA3A.

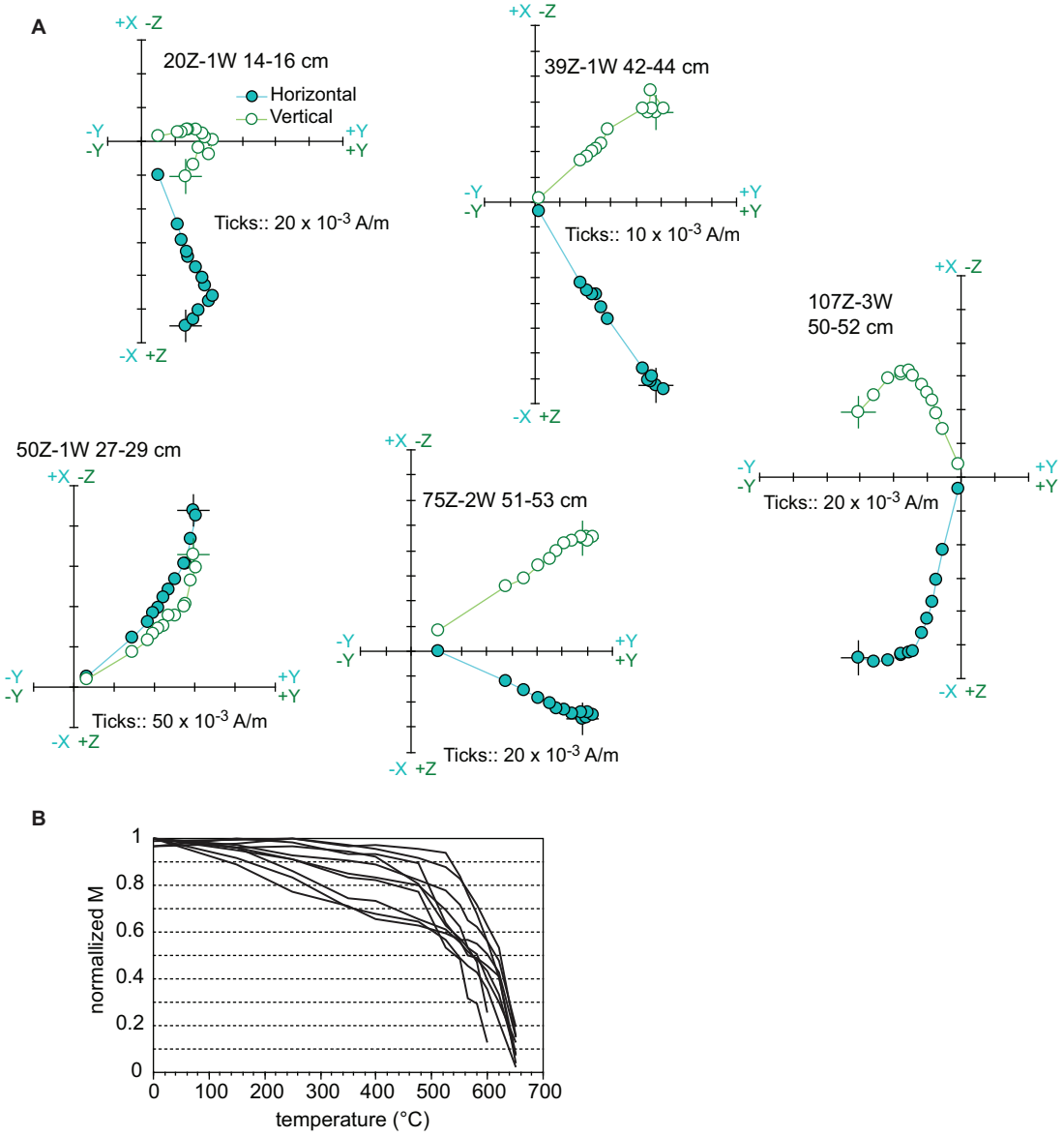

Figure F61. Downhole plots of median destructive field (MDF) and median destructive temperature (MDT) during demagnetization experiments, Hole BA3A.

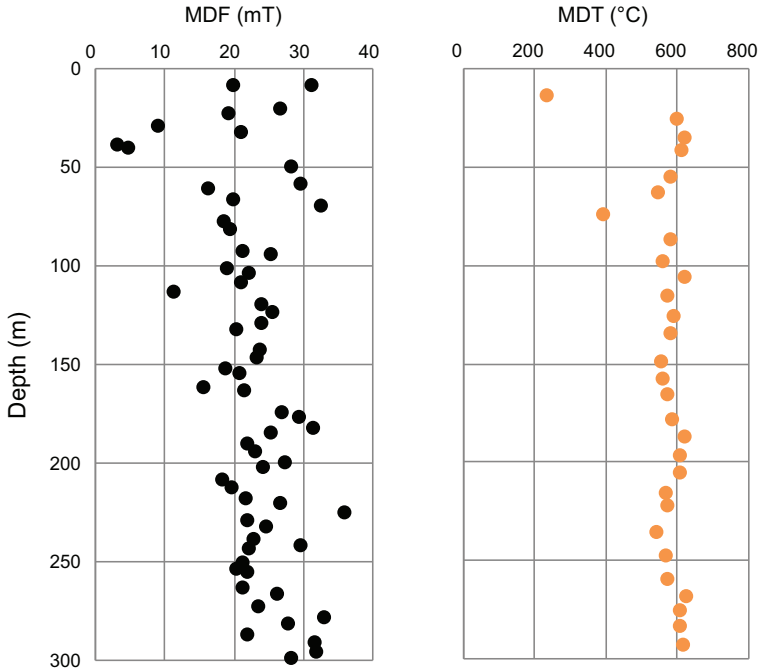

Figure F62. A. Downhole plots of magnetic anisotropy intensity (P'), shape parameter (T), and K_{max} and K_{min} inclinations. **B.** Degree of anisotropy as a function of bulk susceptibility. **C.** Shape parameter T vs. degree of anisotropy of magnetic susceptibility, Hole BA3A.

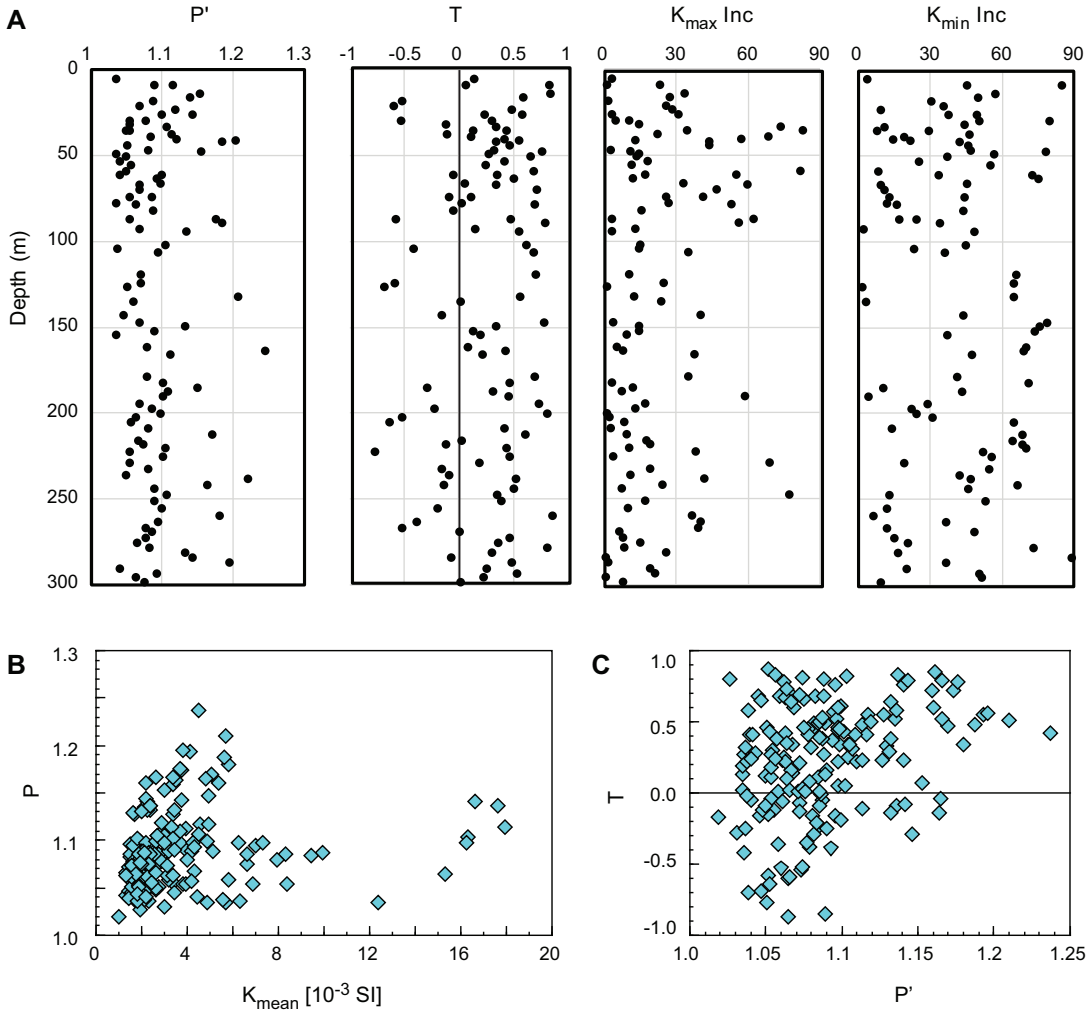

Figure F63. Contoured stereoplots of principal susceptibility axes from AMS analyses plotted on lower hemisphere equal-area projections in the core reference frame, Hole BA3A.

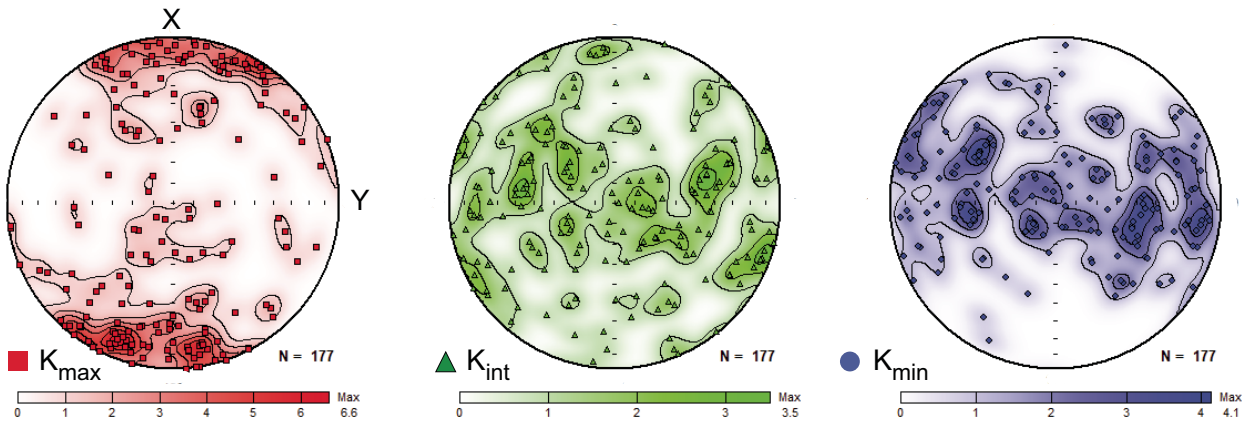

Figure F64. Plots of GRA density, NGR, MS, NCR, and average CT values with lithology, Hole BA3A.

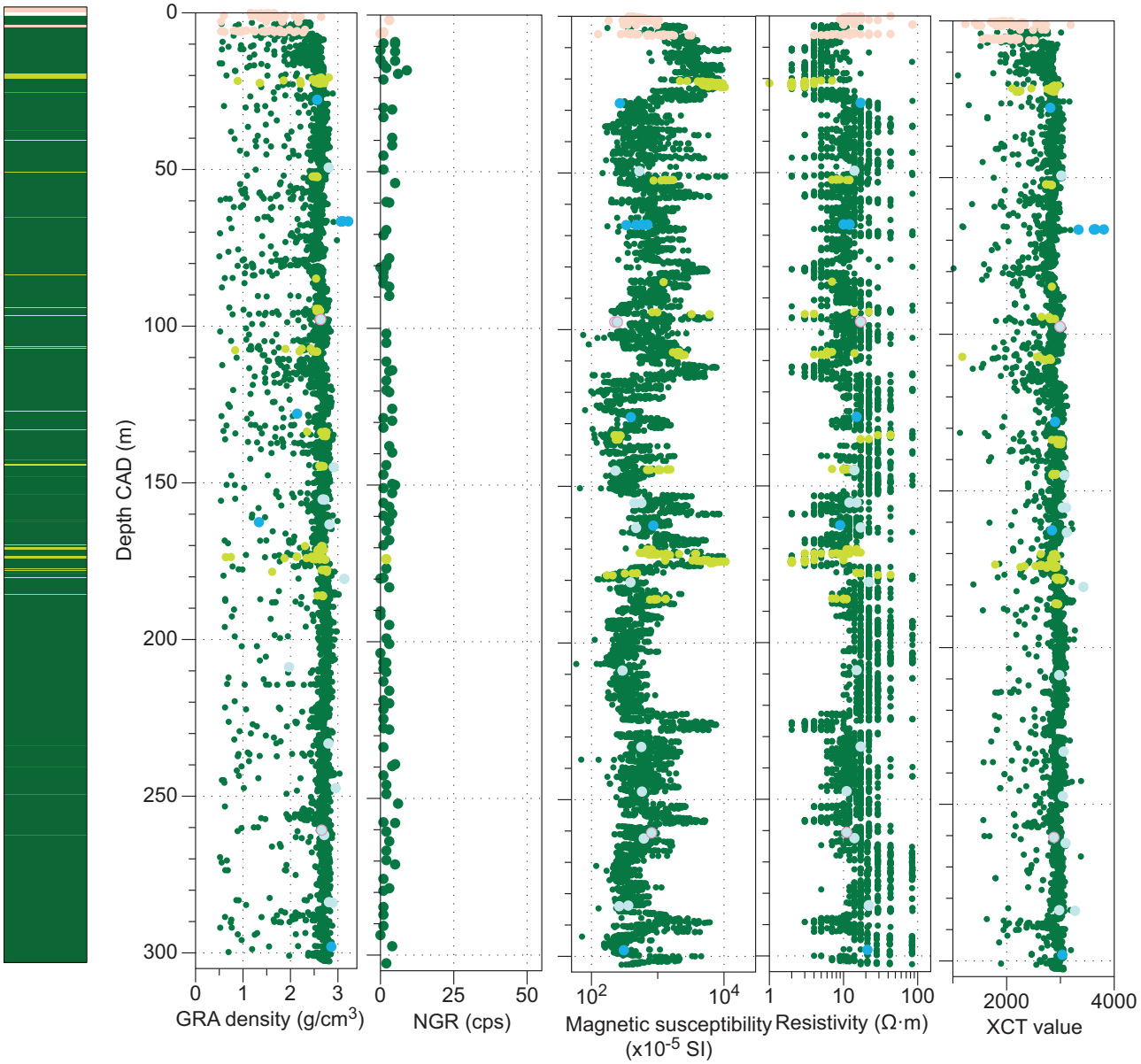

Figure F65. Examples of MSCL-I average and mode of CT values, and CT image, Hole BA3A. (**A**) Harzburgite with vein (Section 55Z-1) and (**B**) harzburgite with thin gabbroic dike (Section 107Z-1).

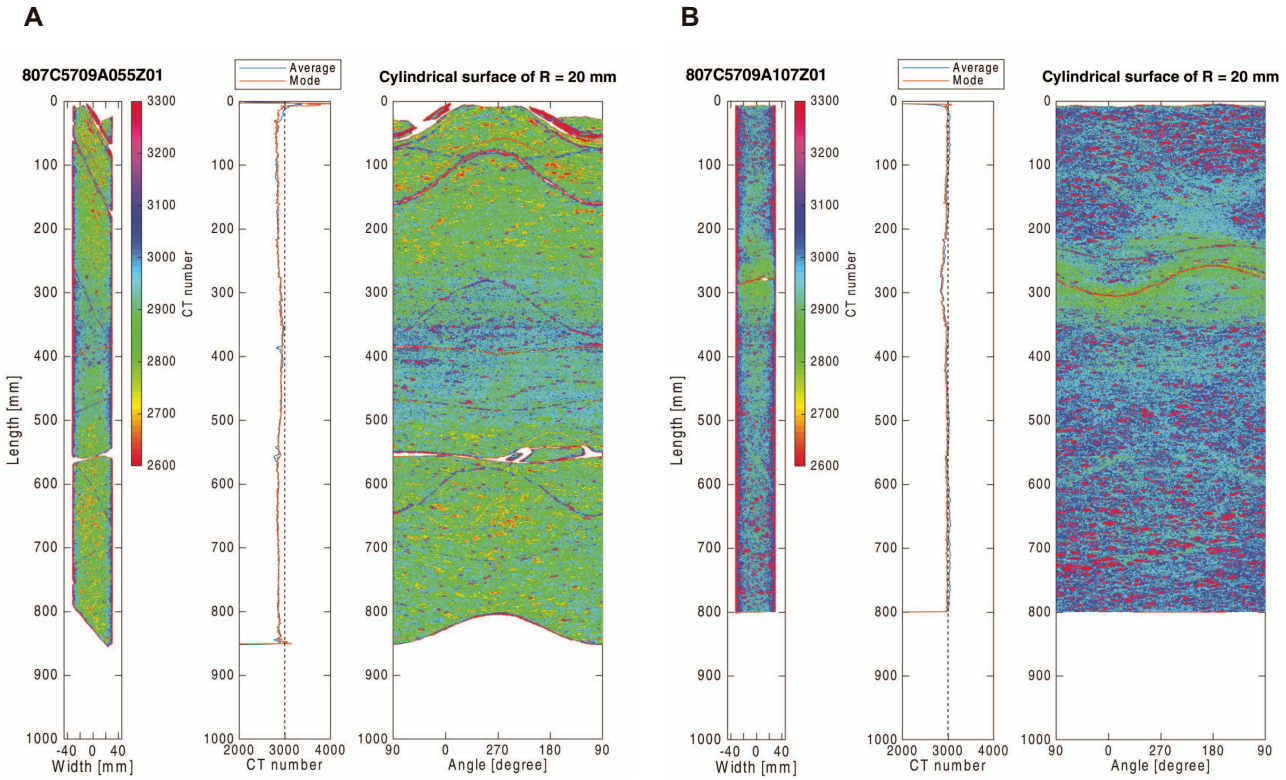

Figure F66. Correlation between (**A**) GRA density and XCT value and (**B**) whole-round resistivity (i.e., electrical conductivity) and magnetic susceptibility, Hole BA3A. Linear fitting lines are shown in each plot.

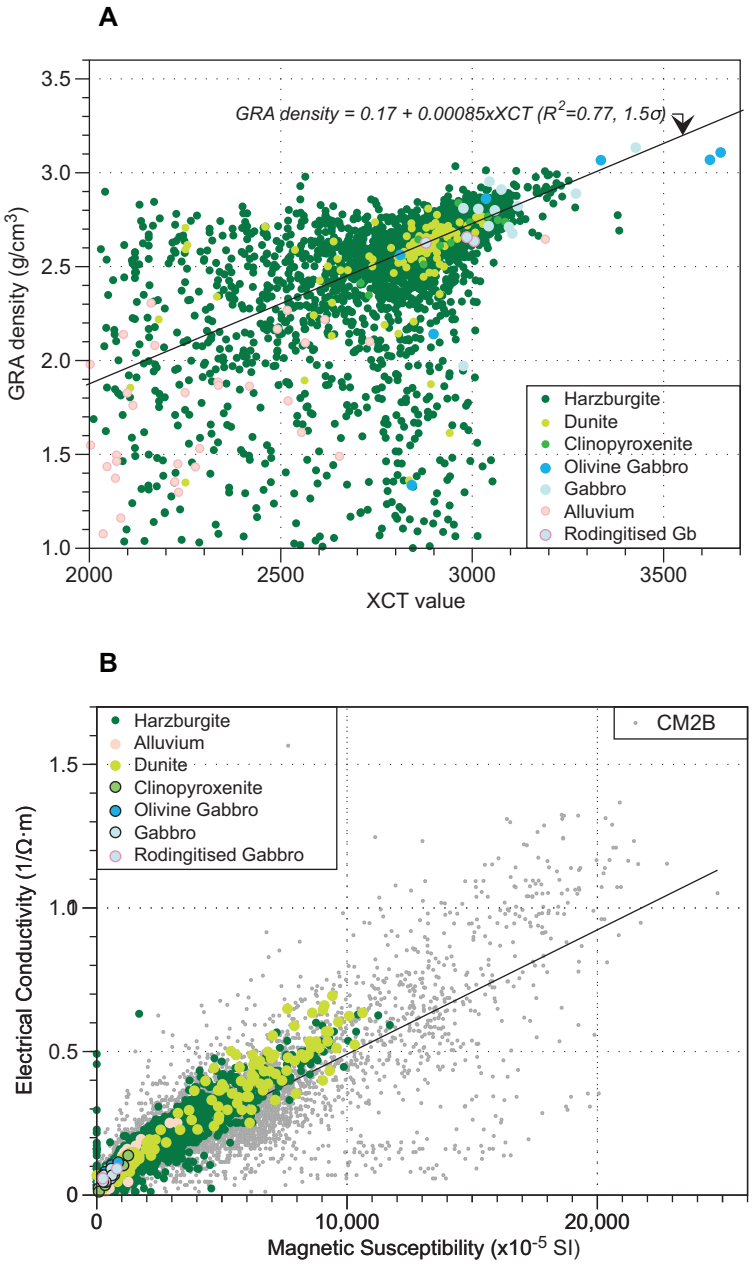

Figure F67. Plots of discrete sample measurements of physical properties, Hole BA3A. (**A**) *P*-wave velocity (V_P), (**B**) bulk density, (**C**) grain density, (**D**, **E**) porosity, (**F**) electrical resistivity under dry and wet conditions, (**G**) bulk magnetic susceptibility (AMS), and (**H**) thermal conductivity.

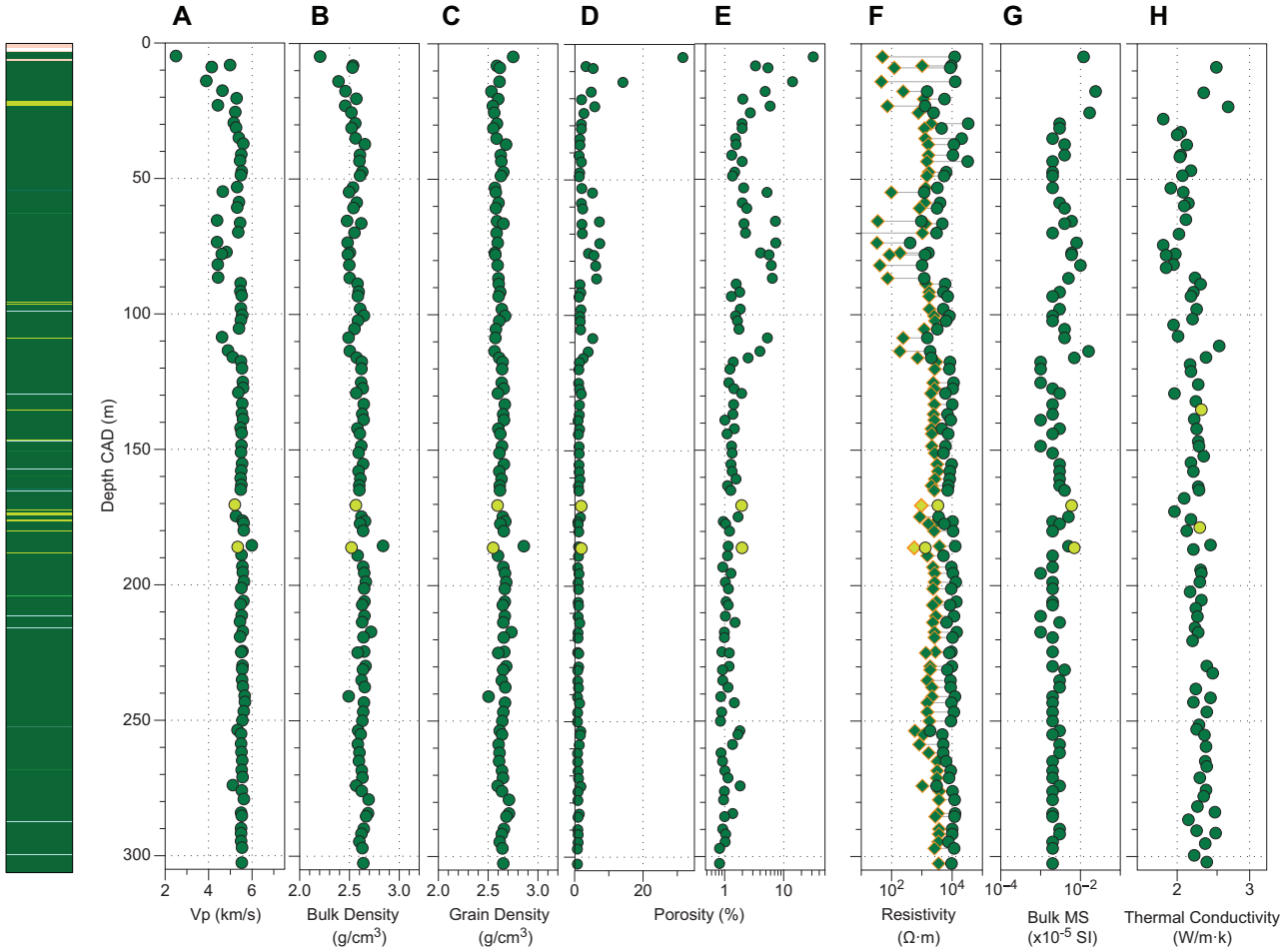

Figure F68. Plot of averaged *P*-wave velocity, azimuthal anisotropy, and perturbation of velocity in each orientation from the average, Hole BA3A.

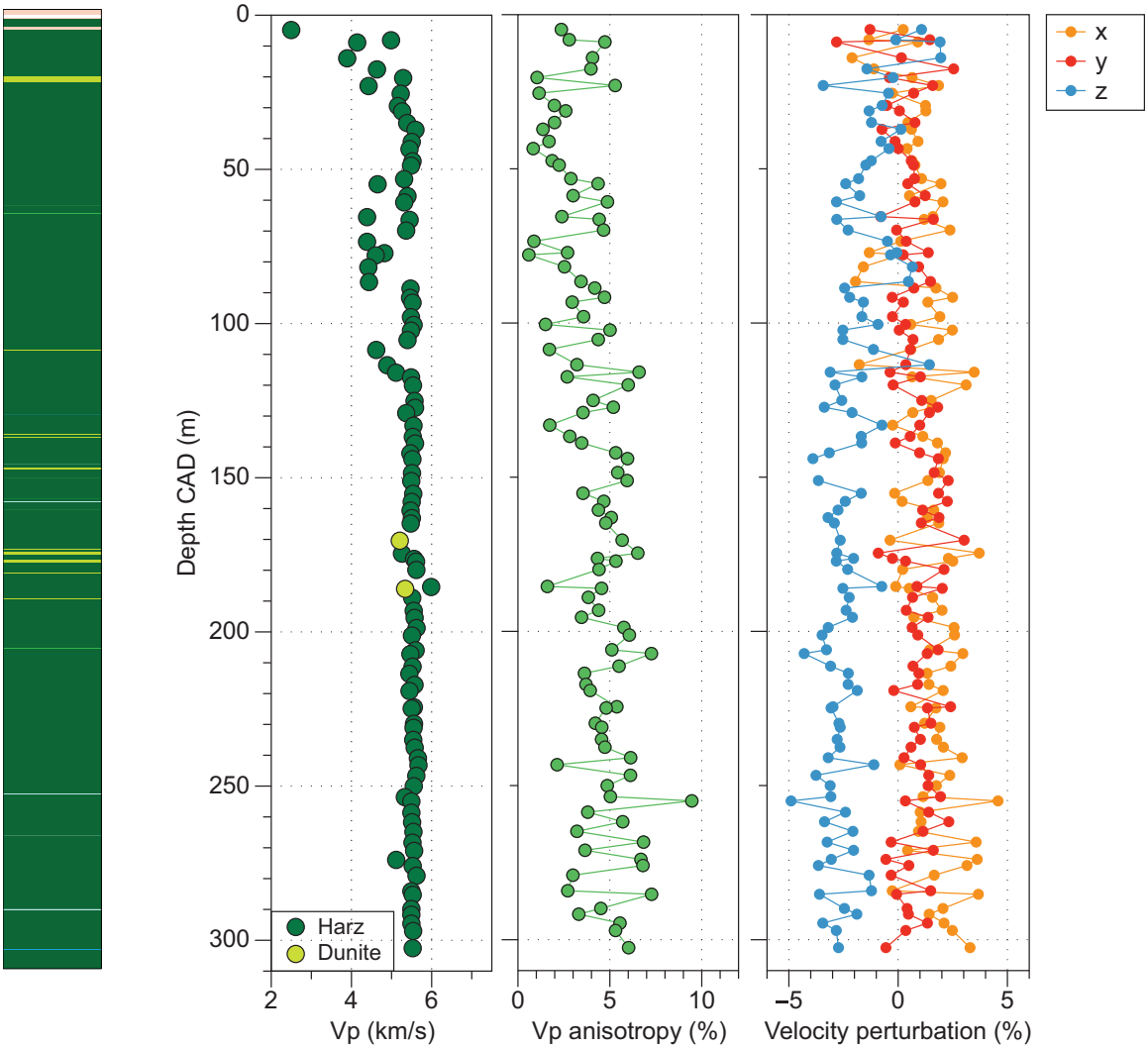

Figure F69. Relationships between *P*-wave velocity and (**A**) bulk density and (**B**) grain density of minicube samples, Hole BA3A. Hole BA1B data are plotted for comparison.

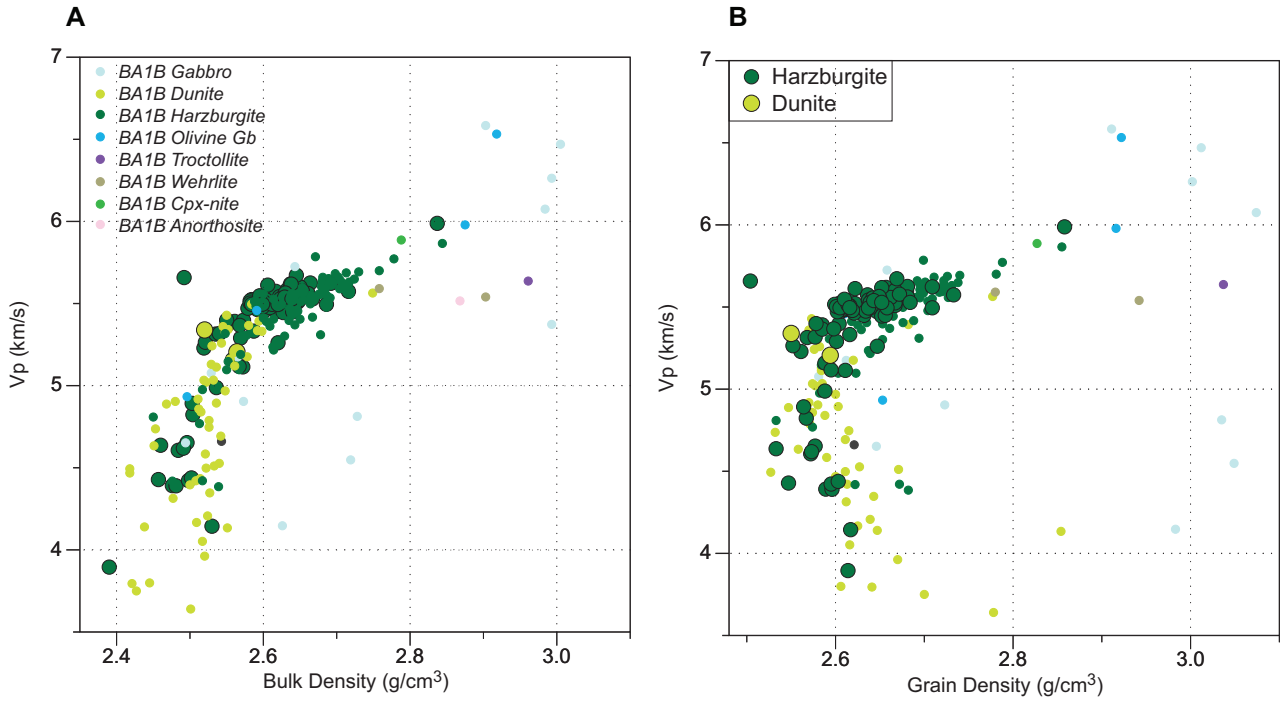

Figure F70. Relationships between *P*-wave velocity and porosity of minicube samples plotted with (**A**) linear scale and (**B**) logarithmic scale of the horizontal axis, Hole BA3A. Hole BA1B data are plotted for comparison.

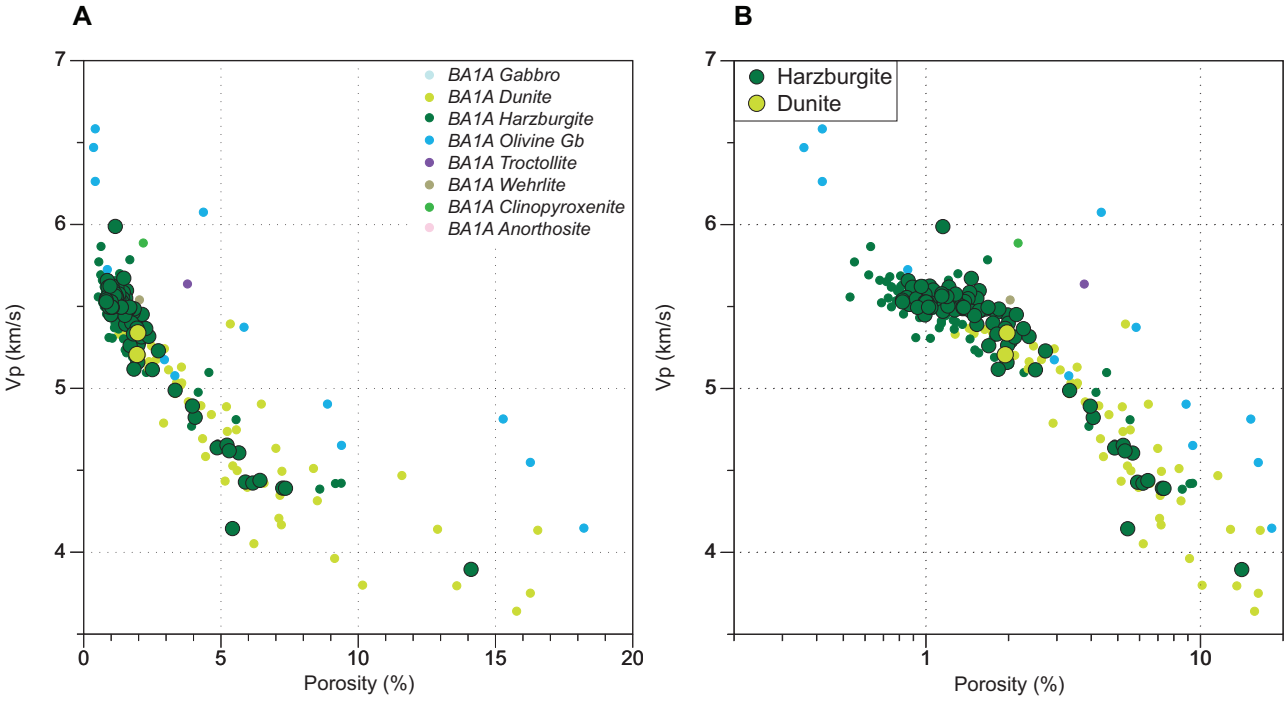

Figure F71. Relationships between porosity and average XCT value from Holes BA1B and BA3A. Gray line is a linear fitting line for samples with XCT < 2950.

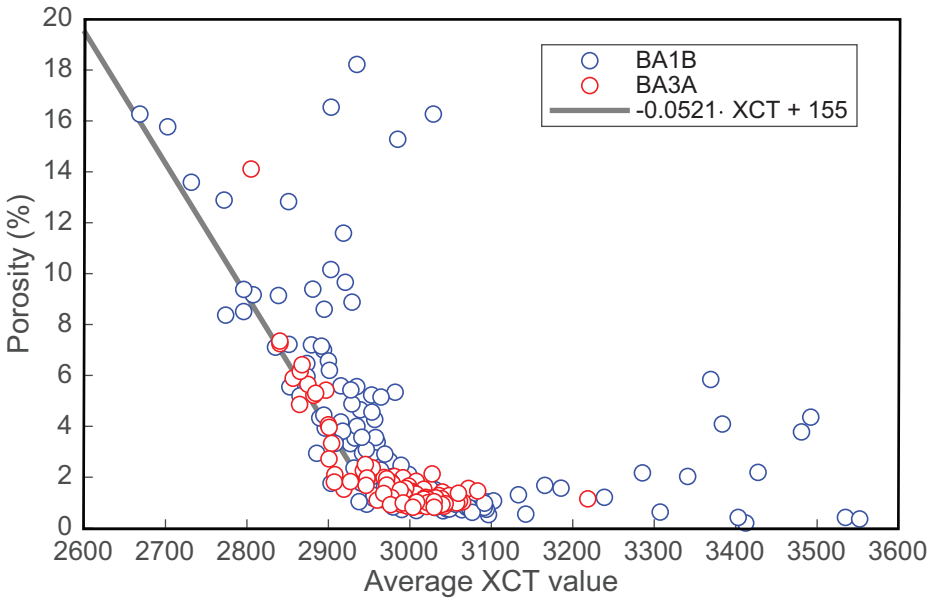

Figure F72. Plot of porosity inferred from XCT data using the linear correlation, Hole BA3A. Red and blue lines are moving averages of 6.1 and 122 cm, respectively.

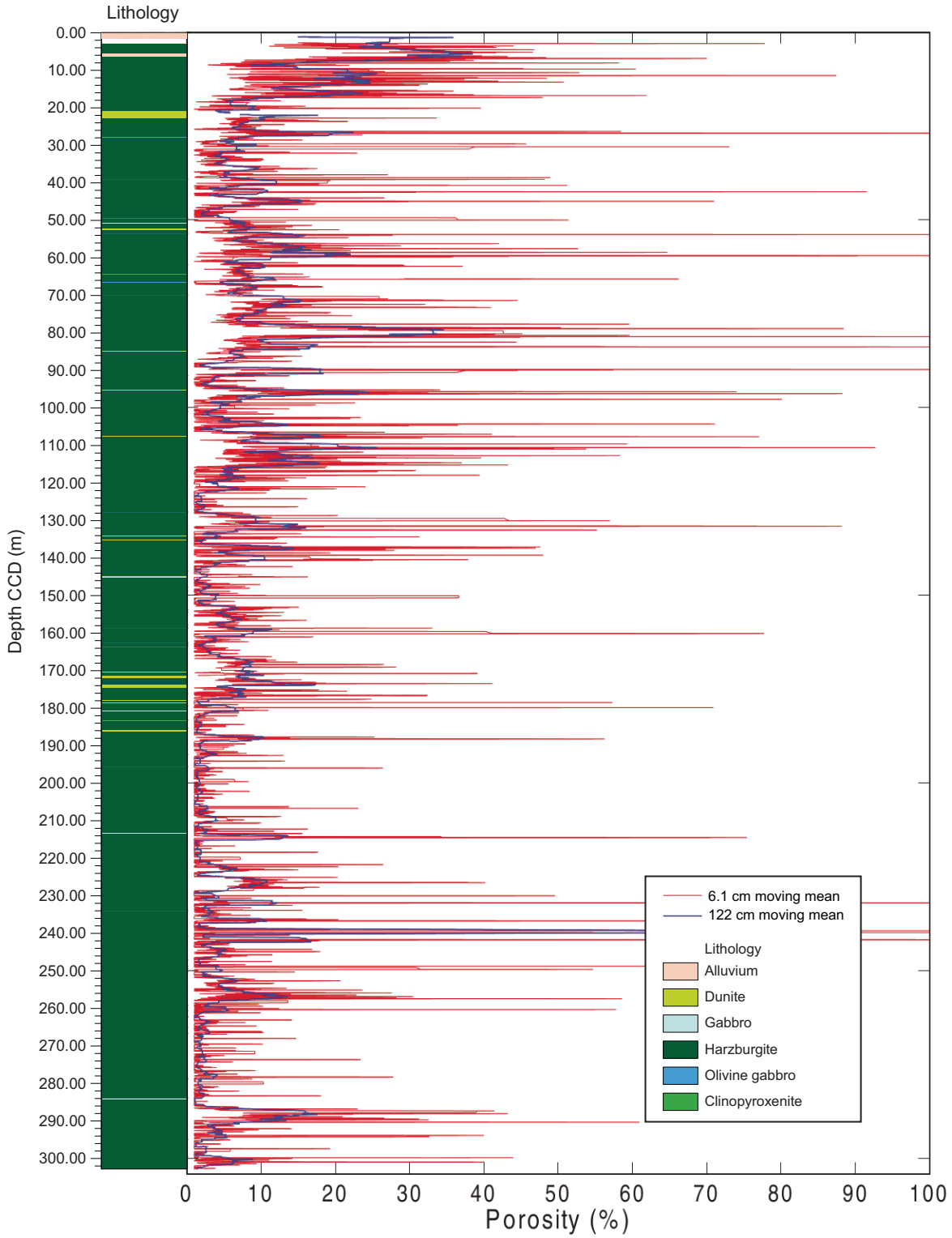

Figure F73. Correlation between bulk magnetic susceptibility and electrical resistivity of the minicube samples (dry and wet measurements), Hole BA3A. Hole BA1B data are plotted for comparison.

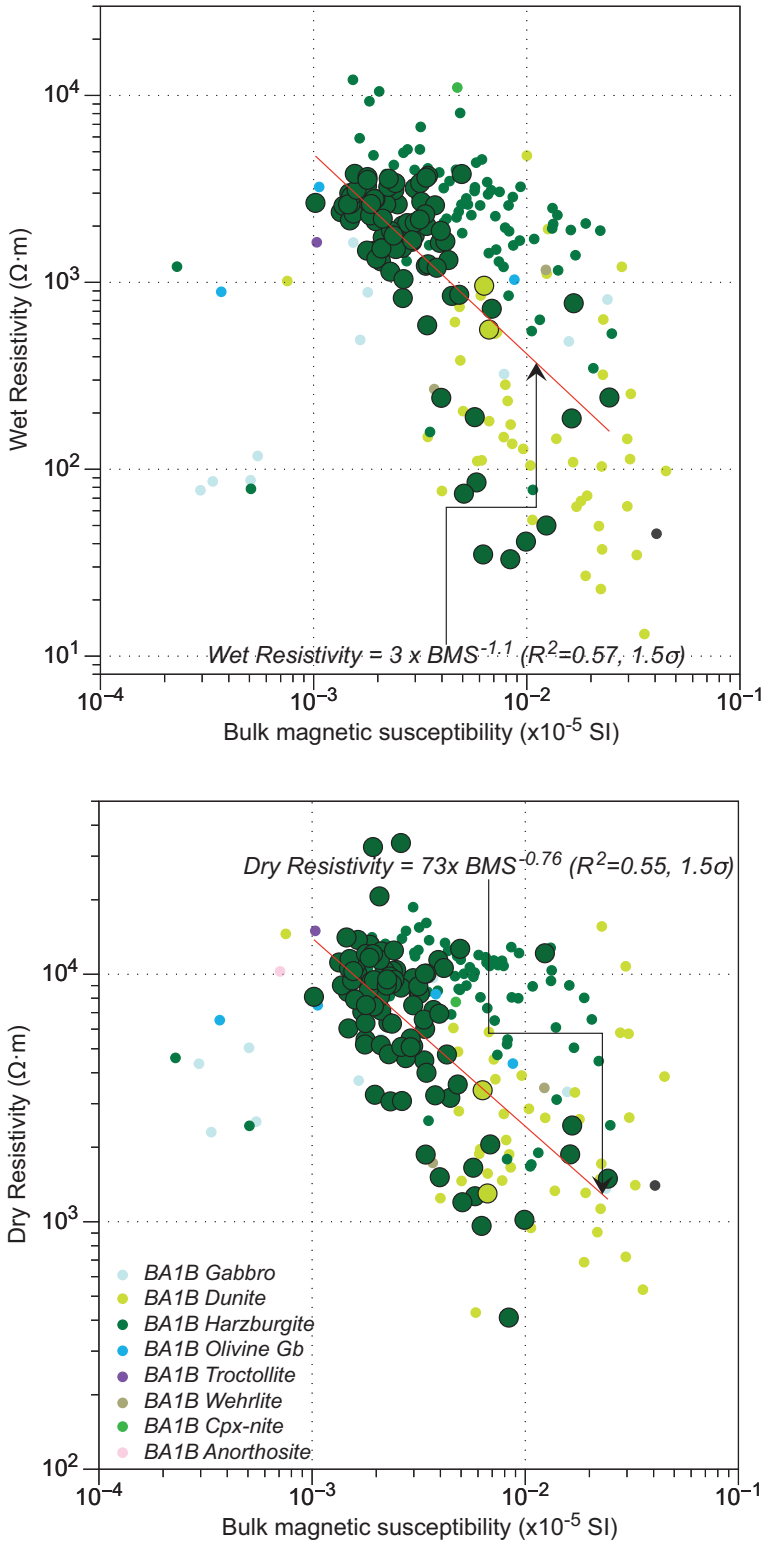

Figure F74. Thermal conductivity and *P*-wave velocity of the minicube samples plotted with XCT value, Hole BA3A. These physical properties are correlated to the XCT value, and fitting lines are shown in each figure. Hole BA1B data are plotted for comparison.

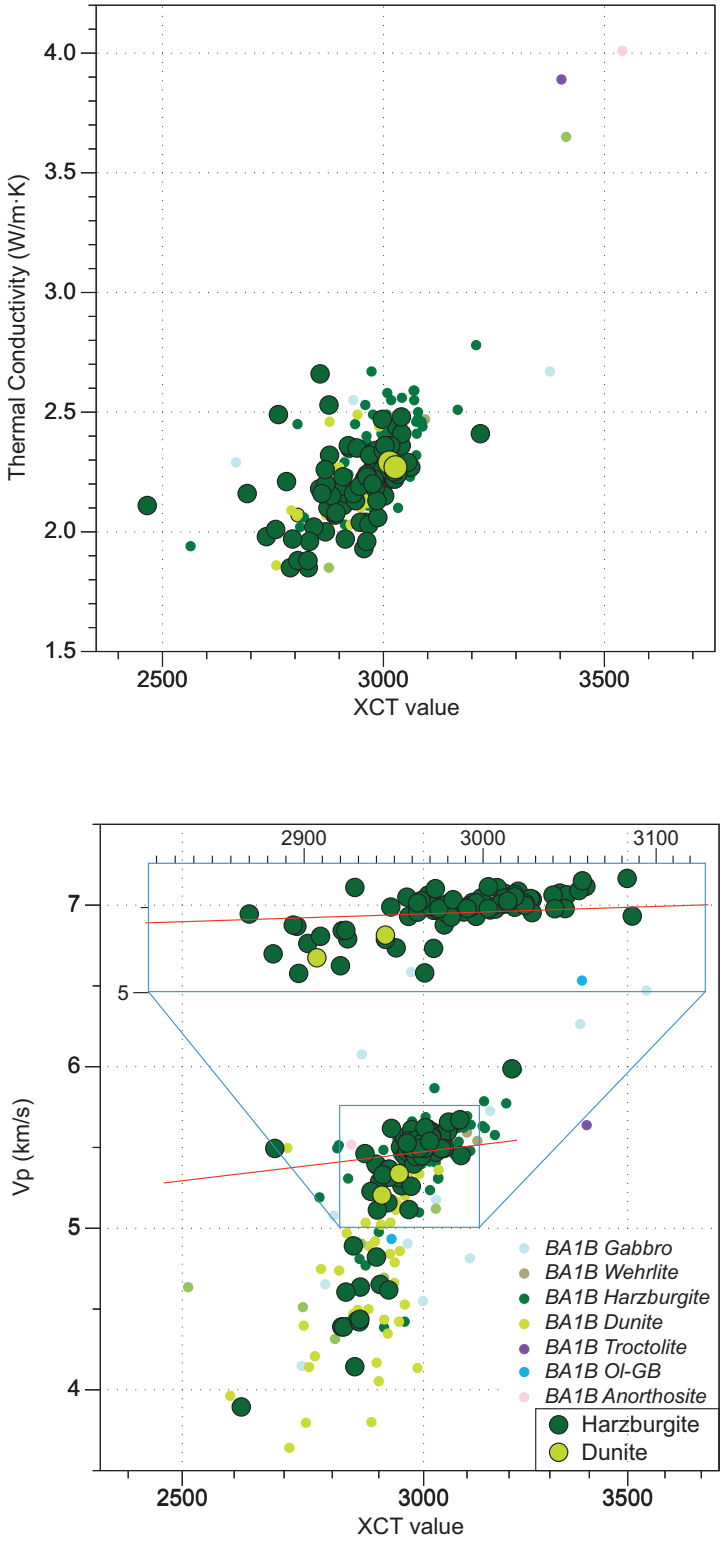

Figure F75. Example of processed imaging spectroscopy data, Hole BA3A. **A.** Lightened MSCL-I image. **B.** Depths of absorption features that are present in serpentine and carbonate spectra. Yellow to green colors = spectral characteristics of serpentine; green to blue colors = spectral characteristics of carbonate. For more discussion of these absorption features, see **Imaging spectroscopy**. Brighter colors indicate deeper absorption features, which often correlates with the abundance of the mineral but can also be influenced by texture and grain size. Other minerals and additional mixing are likely present but are not shown in this view for simplicity.

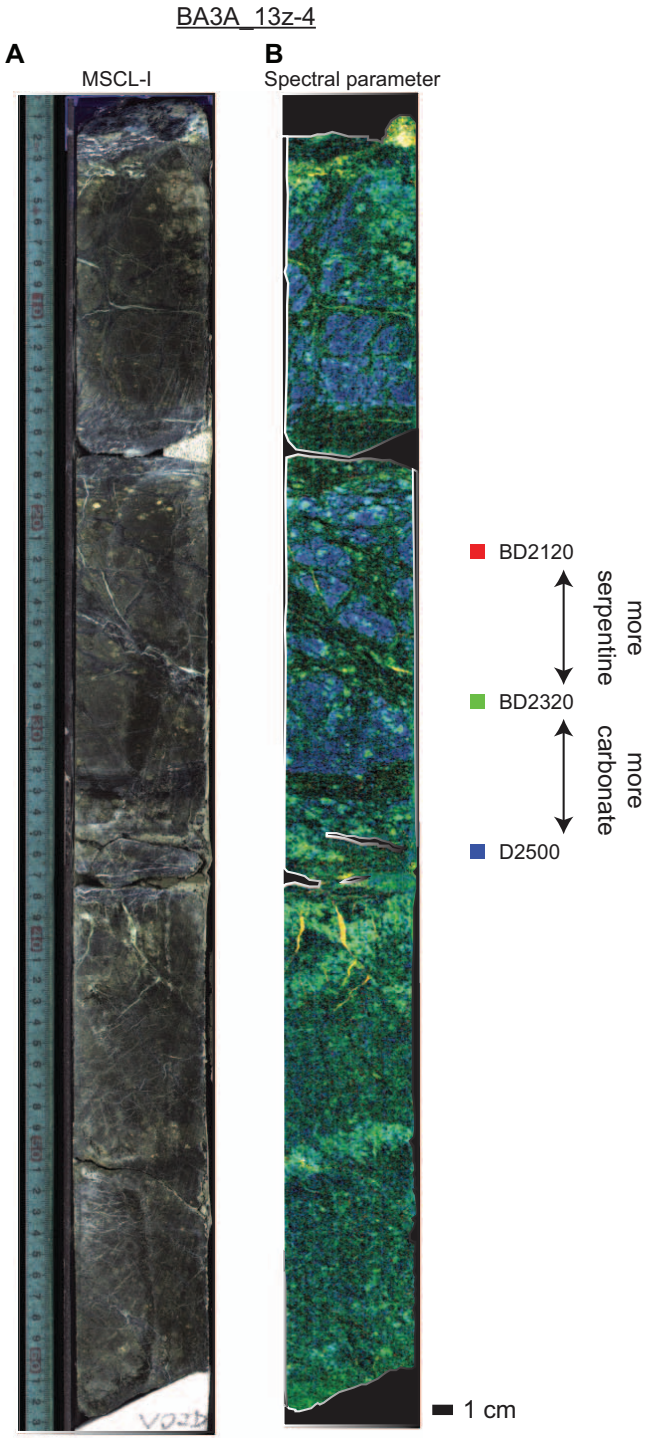

Tables

Table T1. Operations, Hole BA3A. **This table is available in Microsoft Excel format.**

Table T2. Number and thickness of the rock types occurring within the full core, Hole BA3A. **This table is available in Microsoft Excel format.**

Table T3. Details of the lithologic sequences in Hole BA3A. **This table is available in Microsoft Excel format.**

Table T4. Details and results of XRD analysis, Hole BA3A. **This table is available in Microsoft Excel format.**

Table T5. Secondary minerals in veins identified by XRD aboard *Chikyu*, Hole BA3A. **This table is available in Microsoft Excel format.**

Table T6. Whole-rock major element, trace element, and volatile compositions Hole BA3A, with mineralogy by XRD. **This table is available in Microsoft Excel format.**

Note: Total carbon, hydrogen and sulfur compositions were measured by CHNS and inorganic carbon by coulometry on-board DV *Chikyu*. Major element analyses made on-board DV *Chikyu* by XRF were measured on beads for all oxides except for K_2O, which was measured on pellets. Whole rock trace element analyses made on-board DV *Chikyu* were measured by XRF using pellets.

Table T7. LA-ICP-MS analyses, Hole BA3A. **This table is available in Microsoft Excel format.**

Table T8. Natural remanent magnetization and principal component analysis results, Hole BA3A. **This table is available in Microsoft Excel format.**

Table T9. Bulk magnetic susceptibility values and anisotropy of magnetic susceptibility parameters, Hole BA3A. **This table is available in Microsoft Excel format.**

Table T10. Discrete physical properties data, Hole BA3A. **This table is available in Microsoft Excel format.**

Table T11. Velocity, density, porosity, electrical resistivity, magnetic susceptibility, Hole BA3A. **This table is available in Microsoft Excel format.**

Table T12. Thermal conductivity data, Hole BA3A. **This table is available in Microsoft Excel format.**

Supplemental tables

Table ST1. Rock descriptions, Hole BA3A. **This table is available in Microsoft Excel format.**

Table ST2. VCD summaries, Hole BA3A. **This table is available in Microsoft Excel format.**

Table ST3. Vein log 1, Hole BA3A. **This table is available in Microsoft Excel format.**

Table ST4. Vein log 2, Hole BA3A. **This table is available in Microsoft Excel format.**

Table ST5. Vein crosscutting log, Hole BA3A. **This table is available in Microsoft Excel format.**

Table ST6. MSCL-W data, Hole BA3A. **This table is available in Microsoft Excel format.**

Table ST7. MSCL-C data, Hole BA3A. **This table is available in Microsoft Excel format.**